Proposal for the PAC 50: Timelike Compton Scattering Off a Transversely Polarized Proton

May 16, 2022

Abstract and Summary of our goals

The present proposal is an update of PR12-18-005 (2018, PAC46) and C12-18-005 (2020, PAC48) where we received a conditional approval (C2). The experiment will take place at JLab Hall C and will use a real photon beam, provided by the Compton Photon Source (CPS), and the Neutral Particle Spectrometer (NPS), in a dedicated configuration.

We want to measure the transversely polarized target spin asymmetries of Timelike Compton Scattering (TCS process) + Bethe-Heitler (BH process, interfering with TCS) in the photoproduction of an electron pair reaction, $\gamma P^{\perp} \rightarrow e^{+}e^{-}P$. In the TCS process, at the kinematics we are proposing, the incoming photon interacts with a quark of the (polarized) proton, and a high virtuality (greater than 2 GeV^2) photon is emitted. This photon provides us with the hard scale needed to be sensitive to the partonic structure of the proton. The TCS process can be seen as the timelike equivalent of the (spacelike) Deeply Virtual Compton Scattering (DVCS) process, where a virtual photon is scattered off a quark and a real photon is emitted. Implications will be discussed in our physics motivation.

The high virtuality photon emitted during the TCS process decays into an $e^{+}e^{-}$ pair, while in the case of the interfering BH process, the final lepton pairs comes from the splitting of the incoming photon in the target's electromagnetic field. The lepton's azimuthal distribution dependence of the target spin asymmetry comes from the interference between BH and TCS. Therefore, we can extract from our measurements several Compton Form Factors (CFFs) and ultimately the so-called Generalized Parton Distributions (GPDs). Indeed, the TCS amplitude depends on CFFs, which themselves depend on GPDs.

We demonstrated our sensitivity to the GPDs H, $\tilde{H}$ and in particular the still poorly constrained GPD E. The later is very important as it contains information about the angular momentum of the quarks and can also lead to interpretations such as how the spin distributes among the partonic constituents of the proton. Furthermore, we aim at complementing data sets from which GPDs can

be extracted. Currently, most of the observables are coming from DVCS measurements. Our experiment will bring 2 new independent observables (the "in-plane" and "perpendicular" transverse spin asymmetries), that have never been measured at JLab for the equivalent DVCS process, and are therefore independent functions to constrain the GPD models and fits in a a multi-observable multi-parameters approach of extracting CFFs and GPDs, as we are describing in this document.

Furthermore, it is essential to start building a data set of pure TCS measurements (excluding DVCS), to study GPD universality from their extraction solely out TCS observables in comparison to extractions solely out of DVCS observables, in order to confirm or infirm our assumption that leading twist and leading order GPDs are universal. Should we find differences between GPDs that are extracted out of DVCS or out of TCS, measurements such as ours will be essential for understanding the higher twist and higher order effects, which are different in the timelike TCS and the spacelike DVCS processes.

The experiment will take place at JLab Hall C and will use a real photon beam, electromagnetic calorimeters and a recoil proton detector. We will also use a solid NH_3 target where protons are transversely polarized. Our primary goal is to measure transversely polarized target spin asymmetries of TCS+BH over a range in photon's energy from 5.5 to 11 GeV and in proton's momentum transfer of up to -t=1 GeV^2.

Keywords *Generalized Parton Distributions, Compton Form Factors, Timelike Compton Scattering, Neutral Particle Spectrometer, Compact Photon Source, Hall C.*

Related experiments at Jefferson Laboratory *PR-12-18-005 and C12-18-005 (prior version of this proposal)*

Related experiments at Jefferson Laboratory for complementary measurements *Beam spin asymmetry of TCS+BH: E12-12-006A [1] unpolarized TCS with SoLID (approved), E12-12-001 [2] unpolarized TCS with CLAS12,*
Transverse target asymmetry for DVCS+BH: PR-12-12-010 (C1) [3] transversely polarized DVCS with CLAS12.

List of Authors

Debaditya Biswas, M. Boër[1], Brannon Semp, Erik Wrightson, Camille Zindy
Virginia Polytechnic Institute & State University, Blacksburg, Virginia 24061, USA

A. Asaturyan, A. Mkrtchyan, H. Mkrtchyan, V. Tadevosyan[2], H. Voskanyan, S. Zhamkochyan
A. I. Alikhanyan National Science Laboratory, 0036 Yerevan, Armenia

A. Camsonne[3], M. Carmignotto, R. Ent, C. Keith, C. Keppel, D. Mack, J. Maxwell, R. Paremuzyan, L. Pentchev, A. Somov, B. Wojtsekhowski, S.A. Wood, C. Zorn
Jefferson Laboratory, Newport News, Virginia 23606

Z. Akbar, S. Ali, D. Day, I. Fernando, J. Hoskins, D. Keller[4], B. Kriesten, S. Liuti, D. Perera, O. Rondon, J. Zhang
University of Virginia, Charlottesville, VA 22904

V. Berdnikov, J. Crafts, T. Horn, P. Stepanov, R. Trotta
The Catholic University of America, Washington, D.C. 20064

L. Kurbany, E. Long, M. McClellan, E. Mustafa, D. Ruth, S.N. Santiesteban, K. Slifer,
University of New Hampshire, Durham, NH-03824

R. Dupré, M. Guidal, H.S. Ko, D. Marchand, C. Munoz Camacho, S. Niccolai, E. Voutier
Laboratoire de Physique des 2 Infinis Irène Joliot-Curie, Université Paris-Saclay, CNRS/IN2P3, IJCLab (Orsay, France)

M. Amaryan, C. Hyde, M. Kerver, M.N.H. Rashad
Old Dominion University, Norfolk, Virginia 23529

P. King, J. Roche
Ohio University, Athens, OH 45701

J.R.M. Annand, D.J. Hamilton
University of Glasgow, Glasgow, Scotland, UK

G. Niculescu
James Madison University, Harrisonburg, Virginia 22807

J. Stevens
Physics Department, College of William and Mary, Williamsburg VA 23187

[1]Co-spokesperson and Contact person: mboer@jlab.org
[2]Co-spokesperson
[3]Co-spokesperson
[4]Co-spokesperson

K.-T. Brinkmann, S. Diehl, R. Novotny, H.-G. Zaunick
Universitaet Giessen, Giessen, Germany

I. Strakovsky, W.J. Briscoe,
George Washington U., Washington, DC 20052

D. Dutta
Mississippi State University, Starkville, MS 39762

E. Kinney
University of Colorado, Boulder, CO 80309

V. Bellini
University of Catania, Catania, Italy

I. Albayrak
Hampton University, Hampton, Virginia 23669

S. Sirca
University of Ljubljana, Ljubljana, Slovenia

And the NPS Collaboration.

Contents

1 Foreword: summary of PAC48 concerns and our responses

For convenience, we reproduce the main questions from PAC48 (PAC and TAC reports) and our responses in this frontpage. Detailed work to address these questions is available in the main document.

1.1 Motivations

PAC48 report: *Some of the goals of the experiment (e.g., testing universality of GPDs) are overstated as they require many complementary experiments involving DVCS and TCS over a wide range of kinematics. To better understand the impact and complementarity of TCS measurements with respect to DVCS measurements, one should extract the CFFs from DVCS and TCS pseudo-data corresponding to the precision of the planned experiments. The presented impact study is very difficult to interpret, as the uncertainties do not represent the existing and planned data.*

Our response We agree with this statement and rewrote our physics case in order to better emphasize the importance of our experiment in accessing GPD E from TCS+BH data, and solely complement other DVCS and TCS experiments for the purpose of studying GPD's universality. We made clear what are the limitation of our experiment, and studied different scenarios in terms of kinematics, uncertainties, where it would be made more difficult to access the GPDs out of TCS than DVCS. Part of our projections were made at the precision of planned experiment. We still conclude that our physics goals are achievable. We weren't able to include world data for TCS+BH, since none exist at this time, and we decided to not include DVCS+BH for consistency in the error analysis, and also because precision mesurements at our kinematics for that reaction are forthcoming. We clarified our conclusions in the physics case and in the conclusion of the proposal.

A cross check has been recently provided by a student for the interpretation of the extracted CFFs, running an independent analysis, but using the same model and fitting code. There is no existing study that can directly be compared to our fitting method, therefore we decided to simply stay consistent for what we are doing for DVCS+BH and TCS+BH. We presented this work several times in conferences but haven't published it yet (besides PHD and public notes), but will provide more details to the committee members if requested. A publication is to expect for later this year, but unlikely by the time of the PAC presentations.

PAC48 report: *. . . if differences between the GPDs from DVCS and TCS are observed, should these be interpreted as violations of universality, or presence of higher twists, or effects beyond the leading order in the strong coupling?*

Our response This is an excellent question, as it is actually one of the goal of our experiment, of course in complement with other experiments for TCS+BH and DVCS+BH and enhanced pre-

cision measurements. Recent JLab publications on DVCS+BH emphasized the possibility of non-negligible and visible higher twist effects in their measurements. However, we are not sure, nor is any of our collaborator, of such interpretation since no measurement exist for the moment in the timelike equivalent channel, which is TCS+BH. Besides our past phenomenology work, with a partial implementation of twist 3 and 4 corrections in TCS+BH amplitudes (target mass and gauge invariance add-hoc corrections), we are not aware of any other published work on higher twist in TCS. Several groups worked on NLO corrections and found potential non-negligible contribution, though more important at slightly lower ξ than our experiment. It is very difficult to make the distinction between what is a potential higher twist effect, NLO contribution, potential universality violation, etc, in particular since nobody has yet calculated TCS+BH at full twist 4.

To bring a partial answer to this question, we performed fits of CFFs out of DVCS+BH and out of TCS+BH with our partial higher twist contributions, from a leading twist model, from a higher twist model, and with partial corrections only. We found interesting results showing that effects are more important in the real part of the amplitude, and are more correlated to the value of ξ than t. This is one of our motivation in our choice of binning in ξ (and thus forces us to integrate over Q'^2 and not include evolution effects), as we woudln't be able to observe any higher twist effect with a wider binning. We therefore decided to increase the numbers of bins in ξ to as much as we could, at the cost of a lower statistics in each bin, for this sensitivity to higher twist effects. Interestingly, the effects we implemented will drive CFFs extracted out of TCS and out of DVCS in different direction, at a different level for various kinematics. In a more realistic uncertainty scenario, we found that the study of the "shapes" of the extracted CFFs (if we are doing systematic extractions with various input parameters and conditions), will already bring a partial answer to whether higher twist effects are important in DVCS and in TCS. We haven't published these studies yet, but can provide figures if requested by the committee.

Regarding demonstrating the universality of the GPDs, our measurement will contribute by bringing 2 independent observables in data sets (which have zero for now for TCS+BH, and are quite limited for DVCS+BH). A lot more TCS+BH measurements will be necessary, as well as a lot more of theoretical work, in order to provide a clear distinction to what is higher twist, NLO, universality violiation... However, our measurement will be a first and non-negligible contribution to this question.

PAC48 report:*Is the attainable physics sensitive to the 11 GeV beam energy (e.g. if it is slightly less does this change anything)*

Our response If the energy is slightly lower, it doesn't change anything. Recent GlueX measurements are showing that we can go as low as ~ 8.5 GeV in beam energy and still be able to measure TCS. Since our asymmetry is purely related to the target spin, and not to the photon

beam, the different beam dilution factor is not affecting us (double spin asymmetries will be measured, but we are not emphasizing them in this proposal). The acceptance will still be correct. We however expect to run our experiment at no less than 9 GeV in terms of beam energy, to maximize our acceptance and phase space in the kinematic range of interest, i.e. high Q'^2.

1.2 Analysis

PAC48 report: *The proposal does not give enough details about what the signal to background ratio is, and which cuts are most effective to suppress it. A detailed discussion about the magnitude of the background would also be very helpful to understand the performance of the experiment, most importantly how the Monte Carlo simulation has been validated, so as to be sure that the absolute background level is reasonable.*

Our response We updated our analysis method and our background rates as well as our projections in the present document. We decided to use a standard analysis method as we did in our 2018 (PAC 46) version of these studies rather than the most recently submitted (2020, PAC 48) studies involving machine learning and models fitted out of data from other experiments.

In the presented studies (see "Projections" section), we estimate our physics background rate to mostly be coming from pion pair production continuum, exclusive events only, and be of the order of 20%. This estimation is based on fits of published GlueX data, and extrapolations to our kinematics. This source of background is the most difficult to cut from the analysis and is barely affected by our exclusivity cuts. It is however drastically suppressed (10^{-4}) thanks to our calorimeter resolution, and the different signal left by lepton and hadrons in the calorimeter.

We found all other sources of physics background, such as semi-inclusive events, associated production, proton resonances, etc, to be drastically suppressed by the fact of requesting the measurement of the proton track ("acceptance"), and the exclusivity cuts.

Overall, we rely on the results published by the GlueX collaboration in similar studies at similar Q'^2 values, despite a different acceptance and slightly different kinematics, to demonstrate that the level of background in our experiment is low enough to extract the physics signal. Our resolution and statistics is higher than what achieved in GlueX, also comparing their level to our projected background represent a "worse case scenario" for our experiment, and is still sustainable.

PAC48 report: *In order to achieve optimal rejection, separate particle momentum determination as well as cluster pattern recognition will be use. Advances in artificial neural networks have made significant progress with signal classification in this regard [72]." This is the plan to attain optimal rejection, but is it required? Will it be prepared at some level before the experiment and fine-tuned with data?*

Our response It is not required an therefore, we decided to not include them in the present proposal, and go back with a more standard analysis method as in our first submission in 2018. For consistency, we left the machine learning studies that were presented in 2020 in our Appendix. These studies may be finalized and improved once we have data, but until then, we decided to keep working with standard methods that demonstrated their ability to extract experimental results in multiple experiments.

PAC48 report: *Figure 25, page 38: How can the blue line for ρ^0 be above the black (total) line at the right?*

Our response It is part of the simulations that were done by a different collaborator and are not part of the present proposal. These results were published by another collaboration and believed to come from interference, and possibly from model bias in analysis. The final results of background studies and systematics were however consistent between the 2 collaborators who developed independently and with drastically different methods the analysis presented in 2020.

The present proposal uses the same method and similar studies, with improvement, for the background, as we presented in 2018. This is what we refer as "standard analysis method". Our background projections are based on and consistent with Hall D published results. These background studies and analysis have been done by the same person as in 2018, using different versions (rewritten several times) for the analysis code and the event generator, which always provided consistent results. They have also been cross-checked by several students in 2021, who used the same generator, but their own analysis codes.

1.3 Setup

PAC48 report: *The radiation load of the calorimeter is quoted to be 100 krad, which is 33 times the radiation hardness of the crystals: it needs to be shown how the radiation damage between recovery periods influences the energy calibration stability for the signal.*

Our response Predicted from our simulations per month accumulated doses in the $PbWO_4$ crystals are shown in Fig.1. The maximum dose rate of $\sim$200 krad/month is expected in crystals close to the beam pipe. This can be compared to a 432 krad dose accumulation in the crystals from radiation with electrons, at which reduction in longitudinal transparency of about 10 – 20% was observed ([83], fig.20).
Therefore, we do not expect significant deterioration of performance of the calorimeters due to radiation damage, and we do not plan to cure crystals in the course of data taking. We will follow changes in the gains of modules due to radiation by means of gain monitoring system.

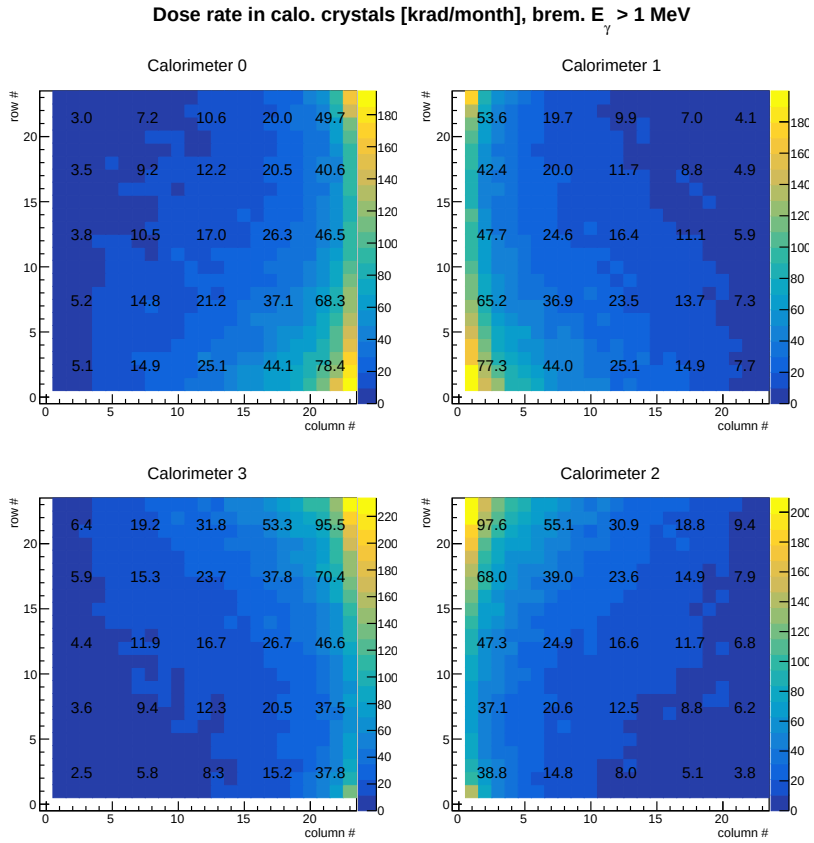

Figure 1: Radiation dose rates in the calorimeters' PWO crystals as predicted by Geant4 simulation. CPS photon beam from 2.7 μA e^- beam impinging on a 10% radiator is modeled. The bremsstrahlung spectrum is integrated from 1 MeV to 11 GeV end point. The simulation includes JLab-UVA target and the TCS detector setups. The numbers are average doses over 5×5 crystal matrix.

PAC48 report: *Good proton identification through the dE/dx measurement can only be achieved up to a momentum of 0.5 GeV: it should be shown how this impacts the measurement.*

Our response From simulations, kinetic energy of recoil protons within range from 90 MeV to 450 MeV can be reconstructed from deposited in the hodoscopes and calorimeters energies. The protons can be identified by means of signal amplitudes from hodoscopes and calorimeters, and times of flights (TOF) relative to the detected e^+ and e^-.

The energy deposition of recoil proton in the hodoscopes is driven by stopping power dE/dx, which at low energies falls as $1/\beta^\alpha$, with $\alpha \sim 1.5 - 1.7$ [99]. A convenient quantity to use for selection is product $E_{HODO} \times (E_{HODO} + E_{CALO})$, where E_{HODO} and E_{CALO} are deposited in the hodoscope and calorimeter energies. For a hodoscope of 5 cm thick plastic scintillator before the calorimeter, protons with the product within range from 2800 MeV^2 to 4200 MeV^2 can be reconstructed to acceptable accuracy.

The TOF will be used to reject background pions. The highly relativistic e^+ and e^- of interest have at least 2.5 GeV energy, and will arrive at the calorimeters in 5.3 ns. The timing resolution in the calorimeters would be 225 ns or better [101]. The protons will arrive at the hodoscopes within range from 6.8 ns (450 MeV) to 12.2 ns (90 MeV). With timing resolution in plastic scintillators $\sim$100 ns [99], the relative TOF can be measured to acceptable accuracy.
For the pions arriving within the same time window, with velocities β within range from 0.410 to 0.737, the kinetic energy will be within 70 - 80 MeV range, which is below the required minimum energy of 90 MeV. They can be rejected by cutting on the sum of deposited energies in the hodoscope and calorimeter.

PAC48 report: *A full GEANT simulation of the electromagnetic calorimeter response for e/π simulation should be provided.*

The Geant4 code, with full simulation of the calorimeter has been developed and used for development of the proposal. It includes CPS bremsstrahlung beam, target assembly, and the detector package. The response of calorimeter includes optical photon generation, tracking and PMT response in number of photoelectrons.

PAC48 report: *. . . Does this mean that the GEMs will be integrated with the trigger? The overall trigger design is not clearly described.*

Our response The trigger will be based on coincident high amplitude signals from e^+ and e^- in the calorimeters. A pair of clusters of energy depositions greater than 2.5 GeV in opposite quarters of calorimeters is requested. In addition, sum of the energies is requested to be greater than 6 GeV. Clusters with seeds within high background rate region close to the beam pipe (within 8° polar angle) are excluded. Based on simulations, the efficiency of such a trigger would be $\sim$72%, and accidental coincidence rate for a 50 ns time window $\sim$60 kHz.
Inclusion of GEM-s will allow for a cleaner trigger. We are considering this option for the future, but as exploratory, and haven't based our present projection on this possibility.

PAC48 report: *A more detailed description of the following critical experimental details is missing: the timing resolutions of all components, the timing requirement to suppress background, and how the GEMs are used in the trigger.*

Our response The timing characteristics of the detectors are important for DAQ electronics and trigger logic. The timing resolution of GEM based trackers depends on the used gas mixture and drift field and is on the order of several ns typically [86]. The timing resolution in plastic scintillators (to be used in the hodoscopes) can reach $\sim$100 ps [99].
The pulse shapes from the PWO calorimeters depend on the used photon detector and DAQ elec-

tronics. The timing resolution of EM showers is energy dependent. It was measured 330 ps and 140 ps at 1 GeV and 9 GeV respectively for the PMT and electronics configuration similar to the NPS [100].
Beam background conditions pose limits on the time window for trigger formation. For trigger logic based on calorimeter signals from e+ and e- alone, with high limits on e+ and e- signals of 2.5 GeV, and 6 GeV on the sum signal, a 50 ns time widow ensures 60 kHz accidental trigger signal rate, which is acceptable for running DAQ electronics.

PAC48 report: *"It should be noted that resolution of electromagnetic calorimeters critically depends on the calibration procedure. With this respect, we count on taking separate calibration runs with tagged photon beam in HallD. Alternatively, we can calibrate with electrons in elastic kinematics, by detecting recoil protons in a magnetic spectrometer. It can be done readily with HMS/SHMS spectrometers in Hall C."*
1. Does this imply that the calorimeters will be placed in Hall D temporarily and then moved into Hall C? A calibration transferred between halls is probably only good to a few percent. 2. What temperatures will the crystals be run at? 3. Will there be any initial plans using cosmics, etc? 4. If we are going to calibrate the calorimeters with the spectrometers, is this separate from the beam time request? 5. The inclusion of an LED gain monitoring system could also be of help for this detector.

Our response

1. Calibration with Hall D tagged photons may be a good 1-st approximation. Precision may be achieved by other means after installation in Hall C.

2. At 18 °C, as NPS.

3. Similar to NPS, the calorimeters will be equipped with top and bottom scintillator paddles for triggering from cosmic rays. Thus initial gain matching of the calorimeter channels may be done by cosmic rays. The absolute calibration we intend to do by detecting scattered electrons from hydrogen target in elastic kinematics. HMS or SHMS spectrometers in Hall C can be used for detecting recoil proton in coincidence. Per channel gain variations will be tracked by Gain Monitoring System. As scintillation yield in PWO crystals is temperature dependent, with rate of 2%/°C, the calorimeter will be stabilized at 18°C as in the NPS.

4. We are not considering to make an independent beam request for calibration.

5. We are considering this option and intend to use it, as other NPS experiments.

PAC48 report: *1. How will the gains be monitored for the PbWO4 crystals throughout running? There are known radiation effects that are observed in PbWO4. 2. Is there a plan to monitor and restore the crystals during the run period?*

Our response

1. We intend to use Gain Monitoring System, as NPS.

2. We found that the crystals will not need to be restored during the run period, as the inte-

grated radiation dose stay low enough over our running period, even for the more exposed blocks and the performance is not affected.

2 Introduction

This proposal aims at measuring Timelike Compton Scattering (TCS) off a transversely polarized target in the exclusive $\gamma P \to e^+e^-P'$ reaction, where TCS is interfering with a Bethe-Heitler like process (BH). TCS corresponds to the scattering of a real photon off a quark of a nucleon, followed by the emission of a high virtuality photon (with virtuality Q'^2=+$q'^2 \gg 1$ GeV^2). The virtual photon decays into a lepton pair (Fig. 2, left panel). BH corresponds to the splitting of a real photon into a lepton pair in the nucleon electromagnetic field, with a high virtuality photon being exchanged (Fig. 2, right panel). TCS is sensitive to Generalized Parton Distributions (GPDs) [4, 5], containing information on the longitudinal momentum fraction x carried by the quark in the nucleon versus its transverse spatial distribution. At leading order and leading twist, for quarks, there are two non-spin flip chiral-even GPDs (H, E) and two spin-flip chiral-even GPDs ($\tilde{H}$, $\tilde{E}$), with GPDs E and $\tilde{E}$ sensitive to the nucleon polarization. We neglect the contribution from gluon GPDs at our kinematics. Fig. 2, we indicate the kinematic variables that GPDs depend on, besides the photon's virtuality: x, ξ (skewness variable) is proportional to the longitudinal momentum transfer to the quark, and t is the squared 4-momentum transfer to the nucleon, i.e. $t = (p - p')^2$, where p and p' are the 4-momenta of the incoming and outgoing nucleon, respectively. We refer to the reviews [6, 7, 8, 9, 10] for details about GPD formalism and phenomenology.

As discussed in [11, 12, 13], for TCS+BH, we can measure several spin dependent observables (from polarized beam and/or target) that are more or less sensitive specific GPDs. In particular, transverse target spin asymmetries enhance the sensitivity to GPD E, which is poorly constrain in current GPD models. It is particularly important for the understanding of the nucleon spin content, and it is sensitive to the angular orbital momentum. The interpretation of the GPD E is that it describes the quark motion in a transversely polarized proton. Its measurement is a key for testing the nucleon momentum sum rule (Ji sum rule [4, 14]):

$$J^q(t=0) = \frac{1}{2}\int dx\, x\, [H^q(x,\xi,t=0) + E^q(x,\xi,t=0)] = \frac{1}{2}\Delta\Sigma + L_q \quad (\forall\xi), \tag{1}$$

where L_q is the quark angular momentum and $\Delta\Sigma$ is the fraction of the nucleon spin carried by the quarks ($\Delta\Sigma \simeq 0.3$).

Our main goal is to measure transverse target spin asymmetries of TCS+BH and extract GPD E from fits of our experimental results and simultaneous fits of our data and data from other TCS experiments (unpolarized cross section and/or beam spin asymmetries). We will also opportunistically measure unpolarized and beam polarized cross sections (circularly polarized photon) off the ammonia target, but these observables will be affected by the target dilution factor compared to measurements that can be done on a LH2 target and are only opportunistic complementary measurements for our goals.

A secondary goal of our experiment is to complement studies on GPD's universality by providing 2 independent constraints (2 orthogonal target spin asymmetries) in TCS+BH fits of data sets containing several spin-dependent observables. Indeed, one of the best way to determine if GPD are universal is to compare GPD results from extraction out of TCS and its spacelike equivalent reaction, Deeply Virtual Compton Scattering (DVCS, $eP \rightarrow e'P'\gamma$). GPDs enter in DVCS and TCS amplitudes through complex functions called Compton Form Factors (CFFs) (in the following we note $\Im H$, $\Re H$ the CFFs depending on GPD H, with equivalent notations for other CFFs and GPDs). DVCS and TCS CFFs are complex conjugate at leading order, leading twist [8]. It provides us a unique opportunity to compare GPDs extracted at the same kinematic points from two of the cleanest processes (the only soft part is the one parametrized by the GPDs). The leading GPD H is the one to be compared in these studies, and it is possible to only perform such comparison out of fits of unpolarized cross sections of DVCS+BH and TCS+BH. However, given that all GPDs are correlated, the interpretation of potential deviations as well as the reduction of correlation systematic uncertainties on GPDs will greatly benefit from measurements such as our. Indeed, the more independent observables we have in the data set used for the fits, the better we can constrain GPD H and reduce its uncertainty. Since our experiment covers a phase space accessible from other DVCS measurement at JLab, our data will be used as complement in such studies. Demonstrating the assumed universality of GPDs would be a milestone, however, observing deviations to their values could lead to even more information in term of the understanding of higher twist and higher order effects, which are neglected in this approach [15].

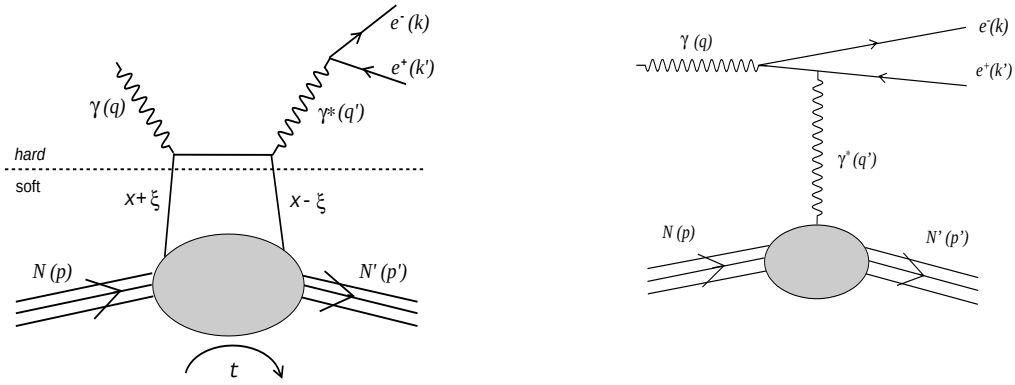

Figure 2: Left: TCS leading order and leading twist handbag diagram. The dashed line indicates the factorization between the hard QED calculable part, and the soft part, which is parametrized by GPDs. Right: Bethe-Heitler process interfering with TCS, leading order and leading twist diagram. Cross diagrams are not represented.

There is no other experiment accessing TCS+BH transverse target spin asymmetries. The first TCS experiment at JLab [2], using the Hall B CLAS12 spectrometer has recently published their results [16], demonstrating evidence of a non-negligible Compton signal at JLab kinematics in the

measurement of TCS+BH beam spin asymmetries. The significantly lower luminosity of CLAS12 compared to our experiment and the fact that most of their statistics is in a lower photon virtuality region that we exclude from our analysis, makes these results unusable in our global fit analysis and for our purpose to constrain the GPD E. However, it motivates further studies of TCS+BH at JLab, both for a precision measurements of the beam spin asymmetry, but also for the unpolarized and polarized cross sections, and for other asymmetries such as target spin asymmetries. The JLab Hall A SoLID TCS experiment [1] (E12-12-006A) which will run in parallel to the J/Ψ experiment, also from an electron beam, will provide beam spin asymmetries and a potential measurement of the absolute unpolarized cross section in a kinematic range comparable with our data, and at a luminosity providing enough statistics to be used in our global fit approach. Compared to the CLAS12 experiment, it will benefit from a higher beam intensity, compensating for a narrower acceptance, allowing for accessing higher virtuality region and bining Q'^2, with an estimated higher statistics by a factor $\sim$10. It will be possible to use the results from the SoLID experiment to complement our data set for CFF fits and for extracting the GPD E, as shown in this document.

DVCS has been studied over many years at Jefferson Laboratory and results from experiments have constraint GPD models in the high x region. Numerous experiments at JLab at 12 GeV aiming at measuring DVCS+BH observables have started taking data or have been approved to run in near the future. They will access GPDs in the same kinematic region as our TCS experiment and allow us for the universality studies as proposed above. The experiment E12-13-010 [18] will be conducted in Hall C, using the NPS calorimeter as for our proposed experiment. It aims at measuring DVCS+BH unpolarized and beam polarized cross sections. Experiments using the Hall B CLAS12 spectrometer include measurements of unpolarized and beam polarized DVCS+BH cross sections off unpolarized proton (E12-06-119, E12-16-010B) [19] and unpolarized neutron (E12-11-003, E12-06-113A) [20]. In addition, the CLAS12 experiment E12-06-109A [21] is measuring DVCS off a longitudinally polarized neutron, and will bring contraints on $\Im E$ of the neutron. A conditionally approved experiment (E-12-12-010) [3] with CLAS12 proposes to measure DVCS off a transversely polarized target (HDice), with goals similar to our TCS experiment. Compared to this DVCS experiment, we are proposing an alternative reaction for accessing GPD E with increased statistical significance. Results from all these experiments allow for extracting GPDs, with particular sensitivities to some of them, depending on the beam and target polarizations (beyond the leading GPD H). In particular, the CFFs $\Im H$, $\Re H$ and $\Im \tilde{H}$ will be extracted. Worldwide, DVCS experiments conducted at CERN and at HERA probed GPDs in a lower ξ region compared to the kinematics accessible at JLab-12 GeV experiments, while pre-upgrade experiments at JLab accessed GPDs in a higher ξ region. We refer to article from the different experimental collaborations: ZEUS [22, 23], H1 [24, 25, 26], HERMES [27, 28, 29, 30, 31, 32, 33, 34, 35], COMPASS [36], JLab Hall A [37, 38, 39, 40], JLab Hall B [41, 42, 43, 44].

Overall, the experiment we are proposing is unique (TCS off a transversely polarized proton)

and will provide for the first time an access to the GPD E of the proton in the JLab kinematic region through the extraction of the Compton Form Factor $\Im E$. At some kinematics, we will also be able to extract the CFF $\Im\tilde{H}$ and bring constraints to the GPD $\tilde{H}$, in addition to a significant improvement in the uncertainties on the GPD H extracted solely out of TCS beam spin asymmetry measurements. Indeed, the two independent target spin asymmetries we aim at measuring, added to GPDs data set will drastically reduce the uncertainty on the leading GPD, H (10 times better), in comparison to what we could obtain from only using the unpolarized and beam polarized cross sections. The major impact of the measurements, in order of importance will be:

1. Extraction of the CFF $\Im E$ and parametrization of GPD E. This result will allow for understanding the partition of the nucleon angular momentum among the quarks.

2. Contribution with 2 independent variable to a new (not existing yet) standalone database of TCS+BH measurement in order to fit CFFs from this reaction independently.

3. Simultaneous fits of CFFs with DVCS and TCS to constrain all CFFs (twist 2) at the same time thanks to new independent observables from TCS, provided the GPD universality is established.

4. Thanks to its contribution to a TCS+BH database for CFFs fits (item 2), reduction of systematic uncertainties and understanding of the correlation errors on GPD extraction, in order to achieve the required precision for a possible demonstration or proof of violation of GPDs universality by comparative measurement of CFFs extracted from TCS (timelike) and DVCS (spacelike).

The proposed experimental setup consists of a high intensity photon source, a transversely polarized proton target, GEM and NPS detectors and scintillators to measure the decay lepton pair and the recoil proton from the BH+TCS reaction in coincidence, and provide constraints on the trigger. Some of the group members of the proposal are deeply involved in the design and construction of the components of the setup which are already under development. Other members are ready to take responsibility for development of new components. The Compact Photon Source [45, 46] is being developed by joint efforts of the CPS collaboration and JLab. The NPS collaboration will take responsibility for the development and the construction of the electromagnetic calorimeters for the lepton detection [47]. The UVa and JLab polarized target groups [48, 49] will provide the transversely polarized ammonia NH_3 target [50, 51, 52], also in collaboration with the UNH group. The Virginia Tech group will be responsible to develop and build the proton detector part of the setup, in collaboration with the UVA, JLab, ODU and ASNL groups, together with the NPS collaboration.

3 Physics case

3.1 Observables

We refer to [11] and Appendix A for more details about the formalism and notations used in this proposal. Fig. 3 is displaying the particles involved in the reaction and the notations for their 4-vectors. TCS+BH unpolarized and beam polarized cross sections depend on 5 variables, which we choose to be the momentum transfer squared t ($t = (p - p')^2$), the outgoing photon virtuality Q'^2 ($Q'^2 = +q'^2$), the photon beam energy E_γ, or alternatively the skewness variable ξ ($\xi = \frac{Q'^2}{2s - Q'^2}$, with $s = (p + q)^2$) and the polar and azimuthal angles (θ, ϕ) as represented Fig. 3. If the target is transversely polarized and the beam is along the z-axis, there is an additional dependence in ϕ_S, illustrated by red arrows on Fig. 3 around the proton vector, and corresponding to the angle between the reaction plane and the target spin. The GPDs depend on x, ξ and t, and the CFFs only on ξ and t (we are neglecting Q'^2 evolution). All our projections are using GPD parametrization from VGG model [53, 54, 7, 55] for the 4 chiral-even quark GPDs H, E, $\tilde{H}$, $\tilde{E}$.

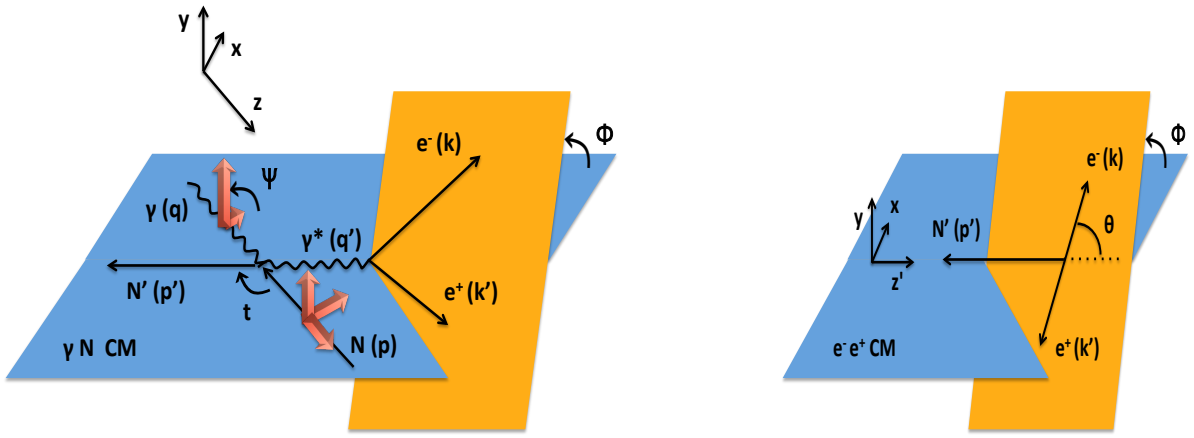

Figure 3: Scheme of the TCS reaction in the nucleon-photon center of mass frame (left panel) and in the virtual photon rest frame (right panel). The momentum of incoming and outgoing nucleon, real and virtual photon, electron and positron are indicated by letters p, p', q, q', k and k', respectively. Left panel: we indicated the angle ϕ_{CM} between the lepton decay plane and the reaction plane. We also indicated by red arrows the possible orientations of the incoming photon spin (Ψ) and the target spin (ϕ_S, θ_S). Right panel: ϕ_{CM} angle is conserved in the boost from γN to γ^* C.M. frames. θ_{CM} is the angle between the lepton direction and the boost axis, defined by the γ^* direction in the γN C.M. frame.

To refer to spin asymmetries, we use the notation $A_{PP'}$, with the first index referring to the polarization type of the beam (U for an unpolarized beam, $P = \odot$ and for a circularly polarized beam) and the second one to the target (U (unpolarized), x ($\phi_S = 0°$), y ($\phi_S = 90°$), or T for any generic value of ϕ_S). Similarly, we use the notation $\sigma_{PP'}$ for polarized cross sections and $\Delta\sigma_{PP'}$

for polarized cross section differences. We define transverse spin asymmetries as

$$A_{Ui} = \frac{\sigma^+ - \sigma^-}{\sigma^+ + \sigma^-}, \tag{2}$$

where $\sigma^{\pm}$ stands for the 4-fold differential cross sections $\frac{d\sigma}{dQ'^2\, dt\, d\phi\, d(cos\theta)}$ for the two target spin orientations $+$ and $-$ along the axis $i = x, y$ or any other ϕ_S direction with $\theta_S = 90°$.

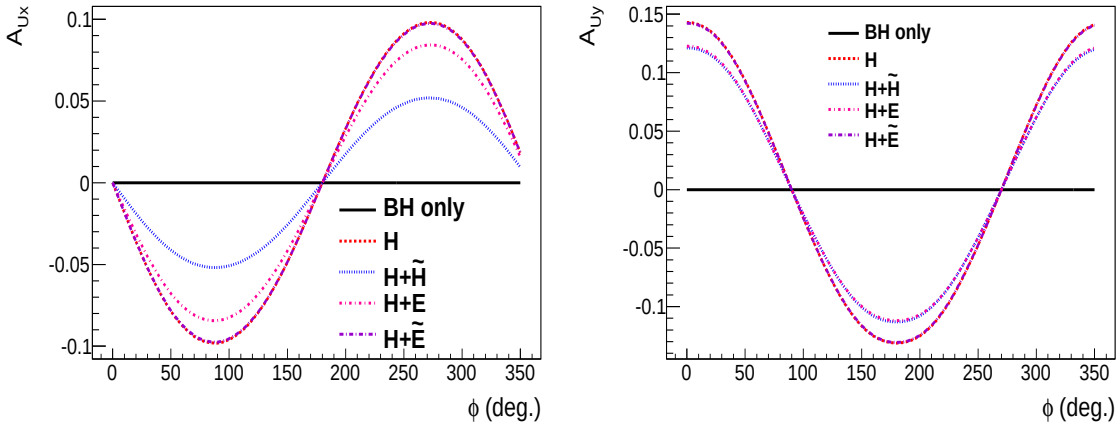

Figure 4: The A_{Ux} (left panel) and A_{Uy} (right panel) asymmetries as a function of ϕ for $\xi = 0.2$, $Q'^2 = 7$ GeV^2, $-t = 0.4$ GeV^2 and for θ integrated over $[\frac{\pi}{4}, \frac{3\pi}{4}]$. TCS is calculated with different GPD parametrizations. From [11].

We show Fig. 4 the ϕ dependence of transverse target spin asymmetries with the target spin parallel (A_{Ux}, left) and perpendicular (A_{Uy}, right) to the reaction plane. These asymmetries are calculated at $Q'^2 = 7$ GeV^2, $\xi = 0.2$, $-t = 0.4$ GeV^2 and for θ integrated over $[45°, 135°]$. This observable is sensitive to the imaginary part of the TCS+BH amplitude, and therefore BH doesn't produce any asymmetry (its amplitude is purely real). The observed asymmetry therefore reflects a contribution from TCS and is sensitive to the GPDs. The different colored curves are from calculation with one GPD (H) or more (H+E, H+$\tilde{H}$, H+$\tilde{E}$). At first order, the asymmetry behaves as a $sin(\phi - \phi_S)$ function. In order to emphasize the sensitivity to the quark angular momenta J_u and J_d through the parametrization of GPD E, we extracted the maximum value of the asymmetry A_{Ux} calculated from different values of J_u and J_d. The result is displayed Fig. 5 and demonstrate that transverse target spin asymmetries are very sensitive to the quark angular momenta.

Analytic calculations of TCS+BH cross sections in [8, 12, 13, 56] demonstrate that the leading order and leading twist TCS and DVCS amplitudes are complex conjugate. However, due to some of the kinematic factors, the ratio of amplitudes TCS/(TCS+BH) is small compared to the ratio DVCS/(DVCS+BH) for the kinematics we are working at. It is also discussed that the unpolarized

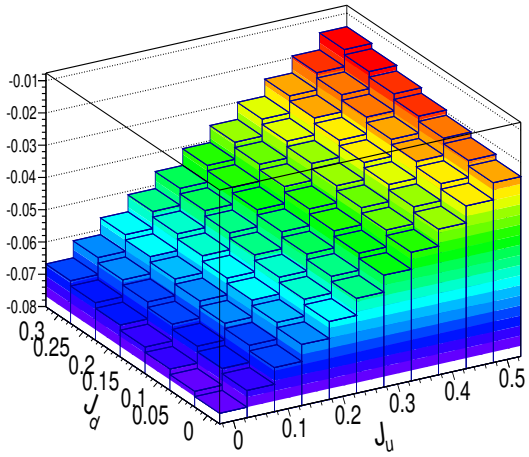

Figure 5: Vertical axis: Maximum of the A_{Ux} (at 90°) for values of J_u and J_d varying from 0 to 0.5 in the GPD E parametrization. Calculations have been done at $\xi = 0.2$, $Q'^2 = 7$ GeV^2, $-t = 0.4$ GeV^2 and using 4 quark GPDs.

cross sections of the two reactions are sensitive to different physics information. However, most of the equivalent beam and target spin asymmetries of TCS and DVCS are strongly correlated. For example, DVCS and TCS transverse target spin asymmetries will similarly enhance $\Im E$

Higher twist effect may impact the possibility to access the same CFFs with DVCS and TCS. Experimental measurements of DVCS [39] suggest that they may not be negligible. Ongoing studies with quantitative predictions for the full next to leading twist in TCS+BH will be soon available [57]. A study including some higher twist terms suggest that their impact on the size of spin asymmetries can be neglected [11] (however not all terms were calculated). If the higher twist effects are small, TCS versus DVCS measurements will allow us to demonstrate (or infirm) the universality of twist-2 GPDs. If large effects appear, measuring TCS will be a unique opportunity to observe the universality violation for GPDs and their important twist 3 structure [58, 59, 60, 61, 62, 63] in a timelike (TCS) versus a spacelike (DVCS) reaction. Similar studies with TMDs (Transverse Momentum Distributions) are done, in particular by comparing semi-inclusive measurements (spacelike photon) and Drell-Yan (timelike photon) [64]. The so-called Sivers effect (twist 3 TMD "$f_{1T}^{\perp}$" [65]), in which measurements using a transversely polarized nucleon are sensitive to, has an opposite effect in timelike and spacelike reactions. It can also be related to the GPD E (its projection in impact parameter space), as shown in [66], which will be accessed in our experiment.

Next to leading order calculations of DVCS+BH and TCS+BH [67, 13] emphasize different NLO structures for the two reactions, and that small but non negligible effects are expected on the observables. These effects are not included in our projections.

3.2 Extraction of Compton Form Factors

Brief description of the method and our parameters (details in Appendix B) To demonstrate the sensitivity of our experiment to the CFFs and the GPDs, and to provide a comparison with what can be extracted out of solely DVCS+BH, as well as the complementarity of DVCS and TCS in a multi-observable, multi-parameters approach, we generated several sets of observables at the same kinematics, for various scenarios of uncertainties, for the two reactions. The cross sections are calculated from [53, 54, 55, 7, 11] (GPDs from VGG model). We used the same GPDs for the two reactions, and CFFs are complex conjugates, as they are calculated at the same t and ξ, at asymptotic limit, and neglecting evolution effects. We used a slightly higher value for the hard scale in our TCS calculations to reflect the fact that our mean Q'^2 value is close to 5 GeV^2, while the mean value for current JLab DVCS measurements is around 2 to 2.5 GeV^2. Our fitting method is based on [68], with an interpretation of the uncertainties based on [69]. Further work has not yet been published (it will soon be in press and has been presented at several conferences). More details about this approach can be found in the public note [70], as well as in the version of this proposal submitted to PAC48.

For clarity, and because it doesn't impact our conclusion, in this document, we are only displaying results for the two following kinematics, corresponding to the typical kinematics for our proposed experiment and typical kinematics for the Hall C DVCS experiment expected to run later this year with the NPS calorimeter. More details and full sets of observable with multiple uncertainty scenario are to be found in the Appendix B. Selected kinematics:

(1) DVCS+BH distributions generated at t=-.2 GeV^2, $\xi = .15$, Q^2 = 2.5 GeV^2, E(beam) = 11 GeV, TCS+BH distributions generated at t=-.2 GeV^2, $\xi = .15$, Q'^2 = 4.5 GeV^2, θ_{CM} = 90°.

(2) DVCS+BH distributions generated at t=-.4 GeV^2, $\xi = .2$, Q^2 = 2 GeV^2, E(beam) = 11 GeV, TCS+BH distributions generated at t=-.4 GeV^2, $\xi = .2$, Q'^2 = 5 GeV^2, θ_{CM} = 90°.

Cross sections from transversely polarized target are calculated at $\phi_S = 0°$ (proton spin along the x-axis) and at $\phi_S = 90°$ (proton spin along the y-axis). In the experiment, we will be able to fit 2 by 2 the orthogonal bins in ϕ_S (8 independent bins as proposed). Both methods are equivalent and we propagated the uncertainties accordingly for their interpretation in this section. Note that the value of Q^2 (or Q'^2) has an impact on the interpretation, with generally CFFs being easier to extract at lower values with this fitting method. As explained above, this choice is motivated by the fact that JLab experiments will not access the same range in TCS and DVCS. If we happen to measure TCS at lower values of Q'^2 in the future (not proposed here), we may come with more optimistic predictions for the fits of CFFs out of TCS+BH than presented here. However, since we are not currently proposing to measure these lower values and no interpretable complementary experiment has been proposed yet with these lower values, we are showing here the more pessimistic scenario, in order to be realistic with the limits (and the advantages) of our experiment.

Results and interpretation Details and results are to be found in Appendix B. We extracted the CFFs from DVCS+BH only, TCS+BH only, and combining the data sets. We found that measuring only the unpolarized cross sections and beam polarized cross sections will allow us $\Im\mathcal{H}$, $\Im\tilde{\mathcal{H}}$, and $\Re\mathcal{H}$. If in addition to these 2 independent observable, we measure longitudinally polarized target spin asymmetries, we will enhance the sensitivity to $\Im\tilde{\mathcal{H}}$ and improve the uncertainties on $\Re\tilde{\mathcal{H}}$ (mostly due to correlations and better constraining the system). If instead, we measure transverse target spin asymmetries , we will access to $\Im\mathcal{E}$. This is the case of our proposed experiment, for TCS+BH.

We are illustrating the above conclusions with our results Fig. 6. The first line corresponds to fitting solely TCS+BH observable, while the second line correspond to fitting solely DVCS+BH observable. The results are similar. It is demonstrating the feasibility of extracting CFFs out of TCS+BH with the same sensitivity if done in similar conditions to fitting DVCS+BH, and it demonstrates the feasibility and a method for GPD's universality studies we aim at doing with our experimental results, in complement to other unpolarized TCS+BH cross section measurements.

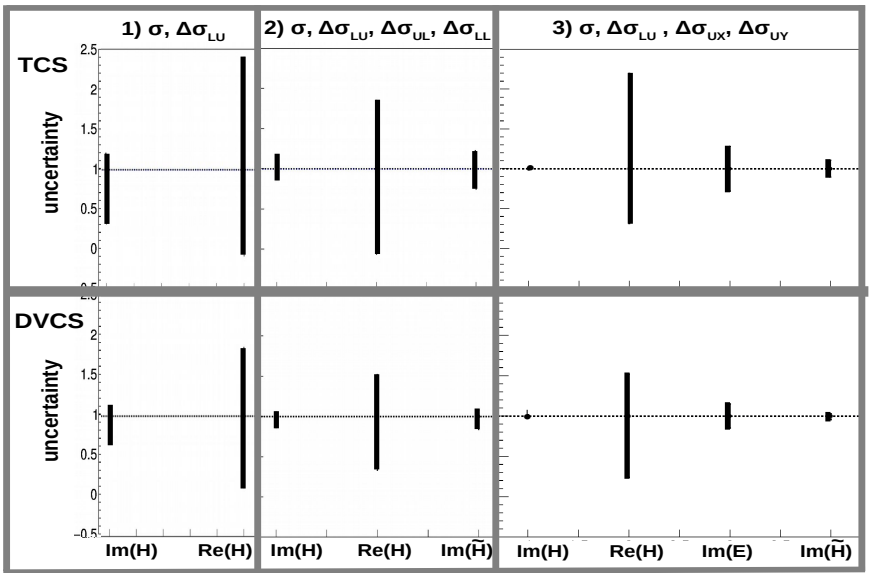

Figure 6: Uncertainties on CFFs extracted from TCS (top) and from DVCS (bottom). CFFs are extracted from σ and $\Delta\sigma_{LU}$ (left), σ, $\Delta\sigma_{LU}$, $\Delta\sigma_{UL}$, $\Delta\sigma_{LL}$ (center), σ, $\Delta\sigma_{LU}$, $\Delta\sigma_{UX}$, $\Delta\sigma_{UY}$ (right). (kinematic 1)

Double spin asymmetries If we had all the transverse and longitudinal target spin asymmetries together (single spin asymmetries only, not shown), we would constrain $\Im\mathcal{H}$, $\Im\tilde{\mathcal{H}}$, $\Im\mathcal{E}$, $\Re\mathcal{H}$, $\Re\tilde{\mathcal{H}}$ and $\Re\mathcal{E}$. Adding double beam+transverse target spin asymmetries (case 5) will strongly reduce the uncertainties on all CFFs, in particular on real parts, but also allow for the first time to access $\Re\mathcal{E}$. As

in this proposal we want to put emphasize on the importance of measuring solely the transverse target spin asymmetry of TCS+BH, we decided to not include the double beam and transversely polarized target spin asymmetries, which will be measured at the same time. However, we demonstrated a drastic improvement in CFFs extractions out of our projected experimental data if we are also including the double spin asymmetries (see [71, 72, 73]). We also demonstrated that this additional measurement will allow for the first time to bring constraints to the CFF $\Re\mathcal{E}$, the most poorly constrained in current GPD models. The measurement can be done in a parallel analysis of the data we will be taking.

Universality studies In this study, we found that, under some assumption, extracting CFFs from DVCS+BH and TCS+BH provide results at the same order of magnitude in accuracy for the CFFs. It is an important outcome, since it demonstrate that we will be able to compare CFFs from independent extraction out of DVCS and TCS to perform studies on the GPD universality, and thus despite the ratio of amplitudes TCS/(TCS+BH) which is much lower than the ratio DVCS/(DVCS+BH) at our kinematics.

Complementarity of DVCS and TCS Assuming that GPDs are universal, we also extracted CFFs out of combinations of observable from DVCS+BH and from TCS+BH. In agreement with the above paragraph, we found that, when we are using sets of non-independent observable with a similar uncertainty scenario, we reduce by a factor 2 the uncertainties on extracted CFFs compared to the case of only DVCS+BH. While it is statistically accurate, it is an unexpected and important result, since as mentioned above, the Compton process is more suppressed in the TCS+BH reaction than it is in the DVCS+BH reaction. Furthermore, observable are not fully correlated [12], therefore even if we are measuring the exact same dependent observable for DVCS+BH as we aim at measuring for TCS+BH, we would still bring independent information from TCS experiments. Our analysis is TCS+BH will both complement DVCS+BH data sets with dependable observables, with new information, plus in the case of our experiment, with 2 new independent observable. Fitting DVCS+BH and TCS+BH observable all together in our multi-observables multi-parameter approach is allowing to extract all the CFFs simultenaously, and bring unprecedented constraints to GPD models.

Note: results in this section use pseudo-data as there is no exploitable results for TCS+BH measurement at the time of writing this document, nor there is any precision measurement of DVCS+BH at JLab 12 GeV kinematic yet in our kinematic range. Any fitting with extrapolation out of JLab 6 GeV data, or fitting from the significantly lower luminosity and different kinematic range of CLAS12 experimental data, would be misleading our conclusions.

4 Experimental setup

4.1 The concept of setup

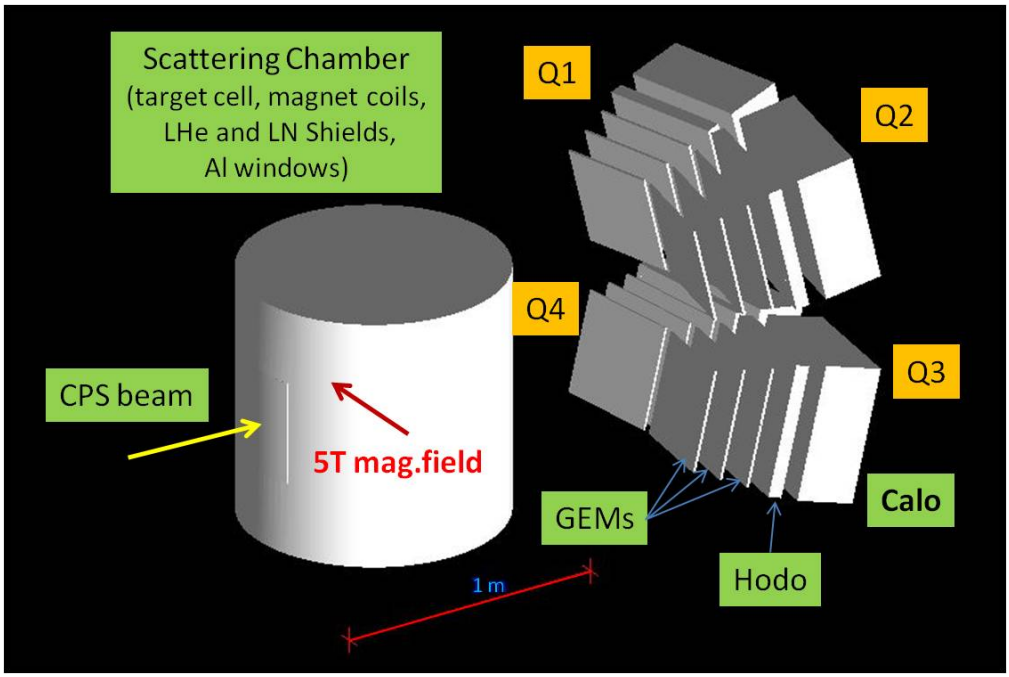

Figure 7: The proposed TCS experimental setup. Detectors are grouped in 4 sections Q1 – Q4 and are oriented toward target. Each stack comprises 3 layers of trackers (GEMs), a hodoscope (Hodo) for recoil proton detection, and a calorimeter (NPS) for lepton detection.

The setup is aimed at the detection of the lepton pair and recoil proton from BH/TCS events in triple coincidence, in forward kinematics. The key components of the setup are the high intensity photon source, a transversely polarized proton target, and a set of detectors for proton (GEMs combo) and lepton detection (NPS) needed for tracking and particle identification.

The experiment will utilize an untagged bremsstrahlung photon beam from the hermetically sealed Compact Photon Source (CPS) ([45, 46]) on the UVA/JLab polarized ammonia target ([51, 52]). The CPS is capable of delivering up to 1.5×10^{12} photons per second with primary CEBAF electron beam of 11 GeV energy and $2.5\ \mu A$ intensity, within the energy range from 5.5 to 11 GeV ([74]). The photon beam has a clear advantage over the traditional mix photon-electron beam when with a DNP polarized target system. This can be understood by target heat-load per photon intensity. Heat-load relates to the degree of secondaries and the rate of radiation damage to the target material as well as the heat-load on the target which must remain at ~1K to keep high polarization during the DNP process. The CPS and polarized target combination with the standard high cooling power evaporation fridge provide the highest figure of merit of this type worldwide. Assuming the aforementioned photon intensity, $1.5 \times 10^{23} cm^{-2}$ and a 3 cm long target

cell with a 0.6 packing fraction, and a $0.867 g/cm^3$ density of frozen NH_3, the luminosity can reach $2.2 \times 10^{35} cm^{-2} sec^{-1}$.

To provide transverse polarization, the JLab constructed rotating target assembly will be rotated by 90° around the vertical axis [75]. For this configuration the rendered angular acceptance is $\pm 17°$ horizontally, and $\pm 21.6°$ vertically. The exit beam pipe excludes from angular acceptance a conical region with opening angle of $6°$.

Our positioning of detectors optimizes coverage of the remaining angular acceptance in a simple way (Fig.7). The detectors are positioned above and below the exit pipe and span from $6°$ to $21.6°$ vertically, and $\pm 17°$ horizontally. Small adjustments in this coverage due to deflections of the particles in the target magnetic field and background distributions are described below, in Sections 4.6 and 4.7. Positioning at 150 cm from target ensures reasonable transverse sizes of detectors.

The proposed detector package intends to maximize acceptance while still providing the information need for particle ID and reconstruction. The physics goals require decent statistical precision which sets the precedent of our detector selection. We will use a combination of three layers of GEM (Gas Electron Multiplier) trackers and a hodoscopes for proton momentum reconstruction, and the set of NPS electromagnetic calorimeters for detection of the leptons as can be seen in Figure 7. The detectors are grouped in 4 sections Q1-Q4 and are oriented towards the target.

The NPS provides excellent information for the 4-vector reconstruction of the leptons with good positron and energy resolution. The cluster profiles also allow the deduction of the incoming angles. This detector also helps provide the PID needed for our leptons and provide the necessary pion suppression.

The recoil proton on the other hand is detected with the combination of this full detector stack which includes the GEM trackers, the hodoscopes and the NPS in that order. The GEM trackers provide excellent position resolution while the hodoscope complements our trigger and finally the NPS helps to confirm PID and proton energy.

The identification of protons relies on measuring energy loss ($dEdx$) in the hodoscopes and energy deposition in the calorimeters, and the timing information from both.

The final state of the two leptons provides a coincidence trigger. The exclusivity of the reaction is ensured by detecting all final-state particles, e^+e^-p. The secondary photon beam energy is inferred with the use of the reconstructed q-vector and the recoil proton 4-vector.

Parameters	Calorimeter	Hodoscope	Tracker
range in ϕ	$\pm 17^o$	$\pm 17^o$	$\pm 17^o$
range in θ	6^o - 21.6^o	6^o - 21.6^o	6^o - 21.6^o
	-6^o - -21.6^o	-6^o - -21.6^o	-6^o - -21.6^o
granularity $\delta\phi$	12.6 mr	13.3 mr	0.3 mr
granularity $\delta\theta$	12.6 mr	13.3 mr	0.3 mr
Energy resolution	$\sim 2\%/\sqrt{E}$	$\sim 25\% \sim dE/dX$	$\sim 60\% \sim$ dE/dX
Time resolution	$<$ 250 ps	$\sim$ 100 ps	$<$10 ns
PID:			
e/π	$\sim$0.01	...	...
π/p	....	$\sim$0.1	...
Background rate	$\sim$ 1 MHz/chan.	$\sim$ 1 MHz/chan.	$\sim$ 1 MHz/cm^2

Table 1: Proposed characteristics of the TCS detector setup. ϕ denotes angle in horizontal plane, and θ denotes angle in vertical plane. The background rates are estimates at the middle of detectors.

It is worth pointing out that the NPS, CPS, and the polarized target system are the same for the WACS experiment already approved to run. The NPS has been proposed to be used on electron beam experiments as well. We use a larger number of NPS detectors than WACS but our calibration will be similar in that these systems will be studies before and after the CPS installation with elastic processes.

The proposed design characteristics of the detectors are presented in Table 1.

4.2 High Intensity photon beam

The proposed experiment will utilize an untagged photon beam from a hermetically sealed Compact Photon Source (CPS) proposed by B. Wojtsekhowski *et al.* [46]. This novel design is capable of producing more than 10^{12} equivalent photons per second providing unprecedented access to the TCS process. This system is coupled to our dynamic nuclear polarized target with a rotating target cell to spread the heat-load and radiation damage in the target material while keeping the photon beam fixed improving our reconstruction performance. Compared to a traditional mix photon/$(e^+ + e^-)$ source or a tagged photon beam this concept presents several advantages, most significantly providing high intensity in a small beam spot on the target taking advantage of the narrow angular spread associated with high energy Bremsstrahlung. The resulting beam also significantly reduces the radiation damage to the polarized target material with respects to photon intensity.

This experiment will use the same CPS design and polarized target system as in the approved experiment E12-17-008 [74]. The main elements of the CPS are shown in Fig. 8. The CPS is optimized by maximizing photon intensity while collimating and reducing unwanted beam particle. After passing through the radiator, the electron beam is separated from the photon beam by means of deflection in the CPS magnetic field. The length, aperture and field strength of the magnet are

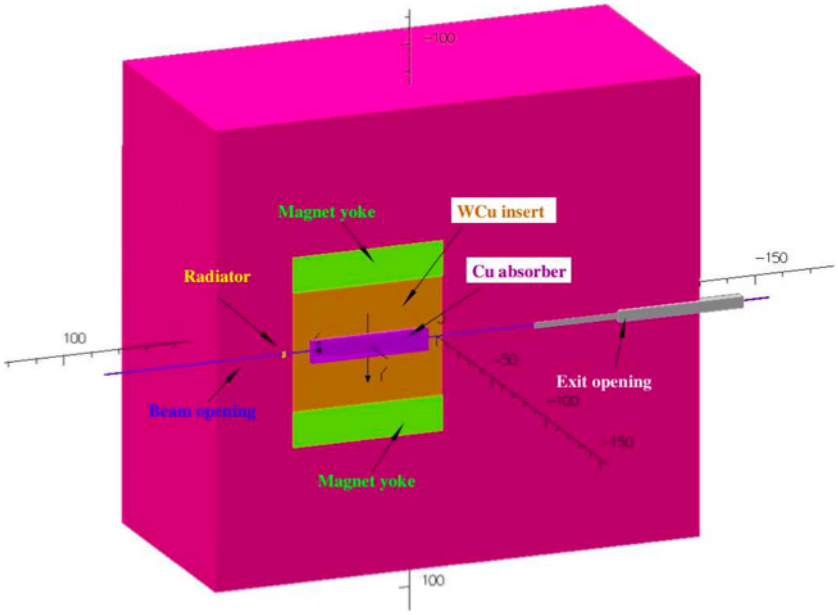

Figure 8: The CPS cut-out side view. Deflected electrons strike a copper absorber, surrounded by a W-Cu insert inside the magnet yoke. The outer rectangular region in this view is the tungsten-powder shield.

unique to this device and quite different from a lower intensity tagging technique used before in CLAS or now in Hall D. The CPS works as polarized photon source, collimator, and beam dump all in one.

The dumping of the electron beam starts in the photon beam channel, so even a small deflection of the electron trajectory by just 1-3 mm due to the presence of the magnetic field is already sufficient to induce a shower. At the same time, such a deflection needs to be accomplished at a relatively short distance after the beam passes through the radiator to keep the source compact. The spot size of photon beam at 2 m away from the radiator is calculated to be $\sim$1 mm. The projected photon flux is $1.5 \times 10^{12}\ s^{-1}$ for a primary electron beam current of 2.5 μA, for photon energies $>\ 0.5\ E_{beam}$ [74, 46]. The magnet designed for the CPS has permendur poles tapered in two dimensions, which allows for a strong magnetic field at the upstream end of the magnet (3.2 T), with the coils located 20 cm from the source of radiation.

4.3 Polarized Target

Hall C has a long and successful history with the use of solid polarized targets, starting in 1998 with the first run of E93-026[77] designed to measure the electric form factor of the neutron. This was followed by its second run in 2001 and immediately by the Resonance Spin Structure experiment, E01-006 [78] in 2002 and by the Spin Asymmetries Experiment on the Nucleon (SANE) [79] in 2009. The polarized target was extensively refurbished and modified for successful measurements

of g_2p and G_Ep in Hall A [75].

These targets exploit a technique called Dynamic Nuclear Polarization (DNP) in which polarization is transferred from unpaired electrons in a dilute concentration of paramagnetic centers (introduced via irradiation at 80K or by chemical doping). At 5 T and 1K the thermal equilibrium of both species (proton and electron) is determined solely by Boltzmann statistics and can be written as $P = \tanh \frac{\mu B}{kT}$. The TE polarization of the electron under these conditions is 99.8% while the proton is 0.51%, the difference due solely to the size of their respective magnetic moments. The dipole-dipole interaction between the nucleus and the electron spins leads to hyperfine splitting. By applying a RF field with a frequency very close to the electron paramagnetic resonance (EPR) frequency (about 140 GHz at 5.0 Tesla), the high electron polarization (due to the large electron magnetic moment) can be transferred to the proton. Either positive or negative polarization can be achieved, depending on whether the RF field is below or above the EPR frequency.

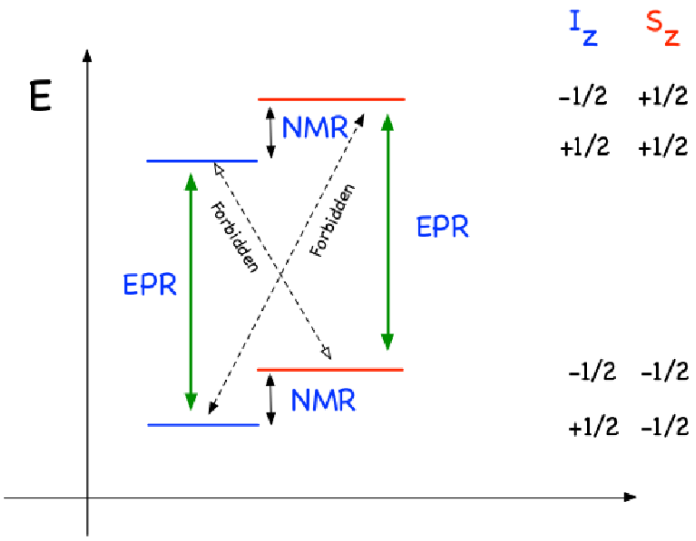

Figure 9: Transitions driven by GHz microwaves in the DNP process

Positive proton polarization results by driving the forbidden transition from the $|S_z, I_z\rangle = |-\frac{1}{2}, -\frac{1}{2}\rangle$ ground state to the $|+\frac{1}{2}, +\frac{1}{2}\rangle$ excited state. The later quickly relaxes to the $|-\frac{1}{2}, +\frac{1}{2}\rangle$ ground state via the allowed EPR transition. Driving the other forbidden transition, $|-\frac{1}{2}, +\frac{1}{2}\rangle \rightarrow |+\frac{1}{2}, -\frac{1}{2}\rangle$, results in negative proton polarization. It is illustrated in Figure 9.

The schematic view of the polarized target and the lower part of the target insert are shown in Fig. 10.

The target magnet is a pair of superconducting Helmholtz coils that when driven at 121 Amps produce a magnetic field of 5 Tesla. The coils have a 20 cm central bore, 100^o opening angle and 8 cm of coil split. The field is uniform to 10^{-4} over the 3 cm diameter right cylinder.

The polarized target assembly contain a 3–cm–long rotating target cells that can be moved remotely to be located in the uniform field region of the magnet or positioned for annealing. The

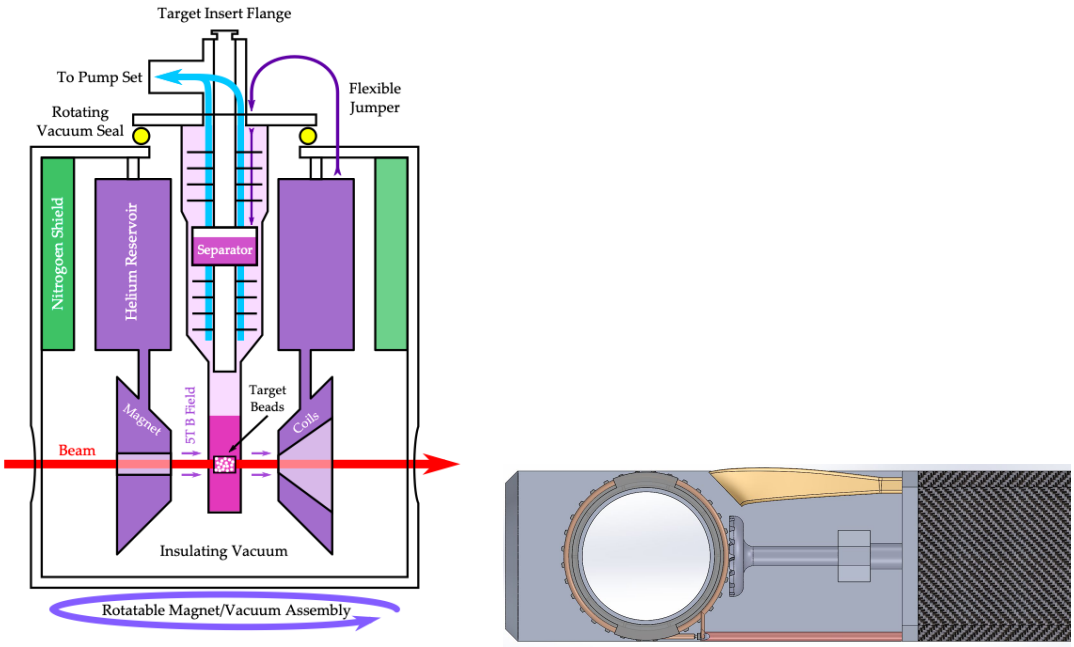

Figure 10: The UVA polarized target used in Hall C experiments. Left: Cross section view of the target, this magnet can be oriented longitudinal or transverse. Right: A drawing of the lower part of the UVA rotating cup target insert.

magnet coils have a 55 degrees conical shaped aperture along the axis and a 38 degree wedge shaped aperture along the vertically oriented mid-plane.

To provide transverse polarization of the target needed in this measurement, the target magnet will be rotated by 90° around vertical axis. Restricted by the magnet coils and scattering chamber window, the angular acceptance in this configuration will span $\pm 17^\circ$ horizontally and $\pm 21.7^\circ$ vertically [5].

The target magnetic field direction has been found to be coincident with the geometric axis of the coils and is known to 0.1° [75, 80]. The target is cooled by a ^{4}He evaporation refrigerator placed vertically in the center bore of the magnet (see Fig. 10). The target material is held in cups at the the end of the target insert which can carry up to 5 targets: a top and bottom NH_3, an empty target and 2 solid targets (C or Be).

The microwaves are generated by an Extended Interaction Oscillator tube (Manufactured by CPI, Canada) which has a maximum power of $\sim$20 W with approximately 1 W delivered to the target sample. $^{14}NH_3$ is chosen as the target material because of its high polarizability, large polarizable nucleon content and resistance to radiation damage.

The target polarization is measured via NMR using the Liverpool Q-meter in which the magnitude of polarization is linearly related with the voltage of the phase sensitive detector: $P = K \cdot S$, and K is a calibration constant. The calibration constant K is determined by measuring the size of

[5] A version of the target used in JLab Hall A g_p^2 experiment E08-027.

a sample's NMR signal under known thermal equilibrium conditions where the polarization can be calculated from the aforementioned Boltzmann statistics. A series of NMR signal area measurements are made and averaged to obtain the calibration constant. They are typically done with each load of target material and as many time as is possible during the run, especially after anneals.

The target material consists of 1-3 mm diameter granules of NH_3, immersed in a ^{4}He bath inside the target cavity. The packing fraction is the fraction of target cell volume filled by target material (NH_3), the rest of the cell being filled with liquid ^{4}He. The packing fraction is important for the simulation of the scattering cross sections and for the determination of the dilution factor.

Interaction of the beam with the target material produces an abundance of paramagnetic radicals which increase the rate of nuclear spin relaxation, but do not contribute to the DNP process. As a result, the polarization decays with the accumulation of beam charge until the time required to achieve a desired statistical precision becomes unacceptable.

In practice, for experiments using 100 nA electron beam this can occur in about 8 hours. Generally for experiments with photon beams, the radiation damage to the target are significantly less so the time running on a particular target load are longer. However, the photon intensity for running with the CPS has increased to record level on a polarized target leading to nearly the same depolarization usually seen with a 100 nA electron beam. Fortunately, the standard process of annealing recombines the paramagnetic centers and restores polarization for a time. To anneal, the target material is moved out of the beam and into the annealing oven in the fridge and heated to between 70-100 K for between 10 and 60 minutes, depending on the phase of the targets life cycle.

For a photon intensity of 1.5×10^{12} equivalent photons per second, it is necessary to use an evaporation refrigerator with $\sim$1 Watt cooling power in combination with a high polarization, high radiation resistant proton target material (NH_3). For electron beam experiments, typically 100 nA is the maximum current on the target. The heat load is about 0.33 W and combined with the DNP microwaves is about 0.5 W. This heat load must be distributed throughout the target so that the target material beads do not experience local depolarization. To do this, the standard fast raster is used to make a $2mm \times 2mm$ square pattern of electrons over the radiator. The resulting photon beam is then distributed over the target by mechanical rotation of the target cell.

Conventional target cells have diameters much larger than the desirable beam spot size, and one is forced to minimize rapid degradation of the target polarization by the beam at one location at the target. The traditional solution of minimizing such localized polarization degradation is fast movement of the beam spot, which prevents overheating of the material and ensures the depolarizing effects of the beam are uniformly spread over the target volume. A beam raster magnet, which moves the beam with a frequency of several Hz, was used in past experiments in Jefferson Lab. However, this does not work for very small collimation apertures, e.g. a few mm by a few mm collimation cone, limiting possible beam motion. The CPS solution for the beam-target raster is target rotation around the horizontal axis. Such a raster method effectively moves the motion complexity out of the high radiation area of the absorber.

Mechanical target rotation is discussed in [45] where rotation rates faster that 1 Hz under stan-

dard polarized target conditions have been demonstrated. The target rotation in combination with the standard vertical motion of the target actuator ($\sim$ 10 mm) results in an effective slow raster which spirals over the full area of the standard 2.5 cm diameter target. Uniform exposure of the target cell is achieved by a combined rotation of the target cup synchronized with an up/down movement of the target ladder. Depolarization and uniform radiation damage can easily be achieved by continuously moving the target at a rate determined by the radius of the circle made through rotation on the target surface, spending no more than a few hundred milliseconds on each set of target beads. Rotation of the target cup with external NMR have been proven viable during multiple studies at UVa. An example of a rotating target cell is shown in Fig. 10 (right). Each insert will contain a single rotating cup. The target is rotated with a shaft connecting to a rotary vacuum feed-through driven by an electric motor outside of the cryogenic environment and above the target insert. The NMR coil surrounds the target cell on the outside and does not touch the cell during rotation. The gold-plated microwave horn is optimally positioned to irradiate the cell while rotating. Additional work on novel rotating target systems are in the press [50].

4.4 Acceptance and reconstruction

The coincidence trigger between the final state leptons of the reaction helps reduce the background. We suppress the background from the two-pion photoproduction by setting a cut on the two leptons energy of 2.5 GeV. The exclusivity of the reaction is ensured by detecting all final-state particles, e^+e^-p and cutting on the missing-particle kinematics. We use an 11 GeV energy electron beam incident on 10% radiator to produce high intensity real photons (see Section 4.2). Highly collimated photons will interact with transversely polarized protons (solid ammonia NH_3) yielding luminosities up to $L = 10^{35}$ cm^{-2} sec^{-1}. Electromagnetic NPS-type calorimeters will be used for detection of leptons, determination of their energies, and for e/π separation. Recoil detectors will be used to detect protons. These detectors will be combined Hall C basic electronics and DAQ (see the sketch of experimental setup Fig. 7).

The generated lepton and proton tracks are traced through the magnetic field of the target, then scattering chamber window up to the detectors at 1.5 m distance from target. As target field is oriented sideways relative to the beam direction, the tracks are deflected up and down. The track bending happens close to the target, for the field being localized within $\sim$15 cm space at target. The fringe fields do not affect significantly the tracks. The high momentum electrons deflect by only $\sim 2^\circ$. While for protons, with momenta from 0.3 to 1.5 GeV/c the bending angle is $\sim 15^\circ - 30^\circ$, typically, and may reach 45°.

Positions and sizes of the lepton and proton detectors and trackers are chosen to match the outgoing track directions (see Sections 4.1, 4.7, 4.6). We display in Fig.11 the t-distribution of accepted events applying a tagging of the two leptons only (left panel, blue curve), and applying in addition a tagging of the proton (left panel, red curve). The ratio of the curves (right panel) illustrates the impact on the acceptance of the proton tagging.

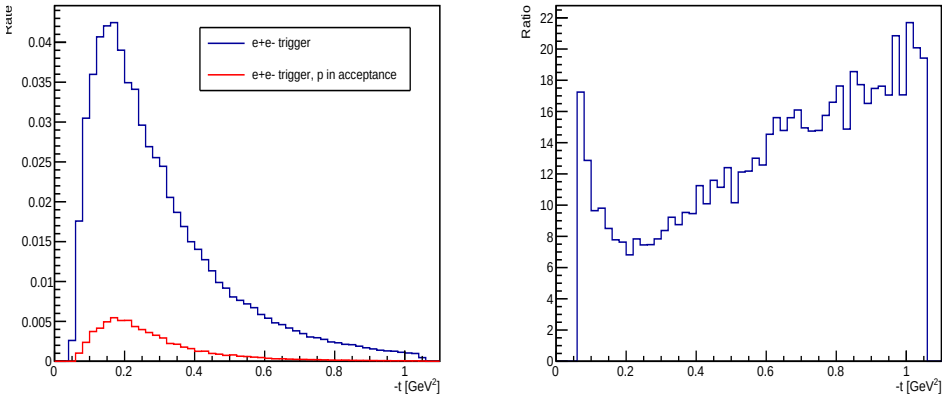

Figure 11: Left panel: the $-t$ distributions for events with the decay leptons within the detectors' acceptance (blue curve), and in addition the recoil proton in the acceptance (red curve). Right panel: the ratio of the two cases. The energy of bremsstrahlung photon beam is in the range from 5.5 GeV to 11 GeV. Kinematic cuts $4\ GeV^2/c^2 < Q'^2 < 9\ GeV^2/c^2$ are applied.

4.5 Tracking detectors

Reconstruction of the reaction vertex, hence obtaining kinematic parameters on event by event basis requires a descent tracking ability of the setup. Gas Electron Multiplier (GEM) detectors [86] are well suited to that purpose for their superior accuracy of coordinate measurement, and high efficiency. Resolutions of reconstruction of transverse coordinates of tracks of better than 100 μm is common among the GEM trackers.

The GEM trackers also are well suited for open geometry measurements, for their capability to withstand background rates as high as 10^6 Hz/mm^2, which is above the requirements of this experiment.

To reconstruct direction at the vertex, both coordinates and direction of a track at detectors should be measured. In principle a double layer arrangement of trackers would suffice to that purpose. However, additional layers are proven to be helpful in disentanglement of tracks in high background environment, in improving tracking efficiency. In our simulations we use 3 layers of trackers in a minimalistic approach.

GEM based trackers are thin and add very little material along the pass of particle. The cover area required for this project, of $\sim$50$\times$50 cm^2 is within the reach of GEM manufacturing technology.

GEM-s have been in use at JLab in a number of experiments. This project will benefit in particular from experience of construction and use of trackers for the SBS spectrometer [81].

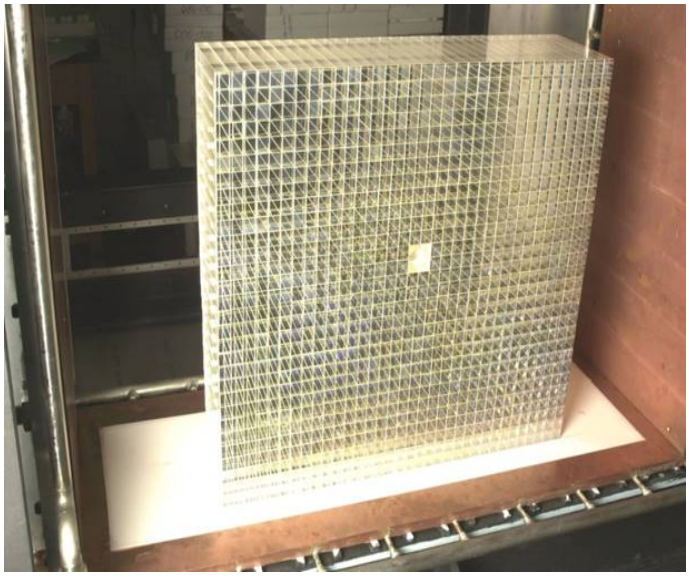

Figure 12: $2.05 \times 2.05 \times 18 cm^3$ $PbWO_4$ crystals used in the high resolution part of Hall B PrimEx experiment calorimeter (HYCAL) [82].

4.6 Lepton detectors

The determination of the kinematic variables Q'^2, ξ and t depends on the accuracy of reconstruction of the lepton energy and angle. Leptons (e^+ and e^-) in the experiment will be detected and identified by measuring their energies and coordinates (X and Y) in a pair of electro-magnetic calorimeters.

The calorimeters are a copy of the shower counter for the projected Neutral Particle Spectrometer. The basic concept for the NPS is a highly segmented electro-magnetic calorimeter preceded by a compact sweeping magnet. Experiments with NPS require detection of neutral particles with energies ranging between 0.5-7.6 GeV with good energy resolution ($\sim 2\%$), and good coordinate and angular resolution of 0.5-0.75 mrad, the latter being comparable to the resolutions of the focusing spectrometers in Hall C.

An assembly of lead tungstate crystals, similar to HYCAL calorimeter in the PrimEx and PrimEx-II experiments in Hall B [82] is recognized as a good match for the NPS calorimeter (see Fig 12). Work for construction of the NPS calorimeter is well underway. Tests have been curried out at CUA, JLab and IPN Orsay to characterize optical and radiation-resistive properties of $PbWO_4$ crystals from SICCAS and CRYTUR, a small prototype detector of 3×3 crystal assembly has been built and studied [83].

The new active divider design of the PMT bases provides a linear response up to high rates of $\sim$1 MHz. More information about the NPS and design studies can be found in reference [84].

The prototype detector has been tested under beam conditions in Hall D at JLab. It was calibrated with tagged photons. An energy resolution of 1.5% for incident electrons of 4.7 GeV energy

has been measured [83], which is comparable with the HYCAL performance (see Fig. 13). On the same test stand Hall D Compton Calorimeter, of similar construction but of bigger size was tested. The measured energy resolution is in line with other lead tungstate calorimeters, the timing resolution falls with energy as $0.32/\sqrt{E(GeV)}$ in the GeV energy range [101].

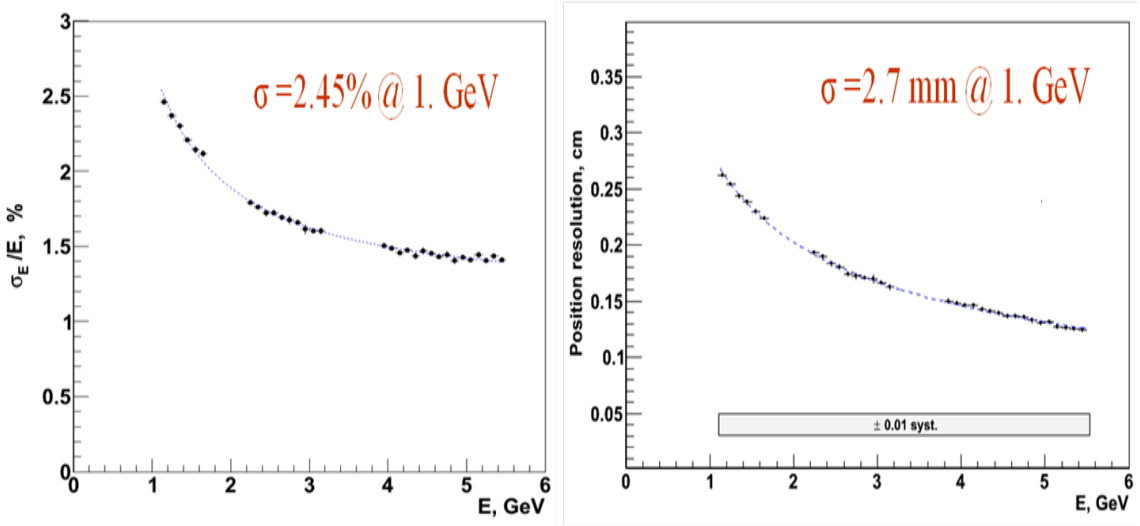

Figure 13: Energy and coordinate resolutions of $PbWO_4$ crystals based HYCAL calorimeter.

It should be noted that resolution of electromagnetic calorimeters critically depends on the calibration procedure. We intend to perform absolute calibration of calorimeters with electrons in elastic kinematics. The recoil protons can be detected with HMS/SHMS spectrometers in Hall C. The gain changes due to radiation and temperature variations in the crystals will be traced by a dedicated Gain Monitoring System.

The transverse size of the TCS lepton detectors is driven by required angular acceptance and distance to the target. Restricted by the target setup angular acceptance is $\pm 17^\circ$ in horizontal plane and $\pm 21.7^\circ$ in vertical plane (see Section 4.3). In addition, the beam pipe restricts scattering angles to greater than 6°. Taken into account vertical deflections of the particles to be detected in the sideways magnetic field of the target, we consider positioning the lepton detectors above and below the beam pipe, at 0° of azimuthal angle.

Reasonable sizes for the detectors are obtained by positioning them at a distance ~1.5 m from the target. This implies $92 \times 41.5\ cm^2$ of active area, for the angular acceptances $\pm 17^\circ$ horizontally and $\pm 15.7^\circ$ vertically. For $PbWO$ crystals of $2.05 \times 2.05\ cm^2$ cross section for construction, the number of modules would be ~1000 for each detector (taken into account addition of a layer around the perimeter of cross-sectional area to exclude shower leaks). This number was refined after simulated acceptance studies, according to which a 50×23 matrix arrangement would be optimal, with 1150 blocks per detector. A further refinement took place due to background simulations, according to which the central region of detectors covering $\pm 1.6^\circ$ horizontally must be excluded

from consideration, because of unacceptably high background rates (see Section 4.8 below).

Hence the final layout of the calorimeters consists of 4 quarters (top left, top right, bottom left, bottom right), 23 $\times$ 23 matrix of blocks each, mirroring each other horizontally and vertically. The horizontal gap between left and right quarters is 8.2 cm wide, the vertical gap is 15.8 cm wide. The number of required lead tungstate crystals totals to 2,116.

4.7 Detection of recoil protons

With the detection of the recoil proton direction vector, and the assumption of a 0° incident photon, the event-by-event kinematics are overcomplete. The CM energy squared s and the momentum transfer $-t$ and their resolutions will be obtained by a combined fit to the di-lepton four-momentum and the direction vector of the proton at the tracker.

Design requirements for the proton detectors are defined by kinematics, required accuracy, available space and cost, as well as by the expected background conditions. The recoil detectors will be located just before the lepton detectors and will cover a slightly larger angular area than allowed by the polarized target. Similar to the calorimeters' case (see Section 4.6), the horizontal band from -6° to 6° and vertical band $\pm$1.6° at the middle of the acceptance will be excluded, and the detector will be divided in 4 separate partitions.

The detected proton momenta will be within $0.3 - 1.2\ GeV/c$ range, with bulk of statistics between 0.4 and 0.8 GeV/c. Proton identification will explore dE/dx signal from the hodoscopes. Thickness of at least few cm will be needed for reliable separation of protons and lighter particles at momenta $\sim$1 GeV/c (Fig. 14). Hence each of the 4 proton detectors is a fly's-eye array of $2\times2\times5\ cm^3$ optically isolated scintillators, with light sensors optically coupled to the rear side.

We will have three layers of GEMs which will be configured similar to the previously proposed applications. These devices can deal with very high counting rate (over 400 kHz/cm^2 [85]) which is helpful for our first layer tracker, closest to the target. Our best timing information will come from the hodoscope and NPS, so high position resolution is critical to our reconstruction. These detectors give a spatial resolution on the order of 70 μm [86]. A similar design has been adopted for the tracking systems for this experiment. The GEM technology permits large area detectors with high counting rate capabilities.

The recoil detector package will leverage all three systems, the hodoscope, the GEMs and the NPS. A product of deposited energies in the hodoscope and calorimeter will allow for localization of the recoil proton. The total energy deposition of the selected events provides kinetic energy to acceptable accuracy. The derived absolute momentum and track direction from the GEM trackers will allow for backtracking through the target magnetic field and reconstruction of the recoil proton at vertex.

For the recoil protons of 90 MeV to 450 MeV low energies, the timing capabilities of the lead tungstate calorimeters and the scintillator hodoscopes allow for time of flight (TOF) measurement relative to the detected in the calorimeters relativistic e+ and e-. Combined with the energy mea-

surement, this will allow for separation of protons from background pions within the TOF domain.

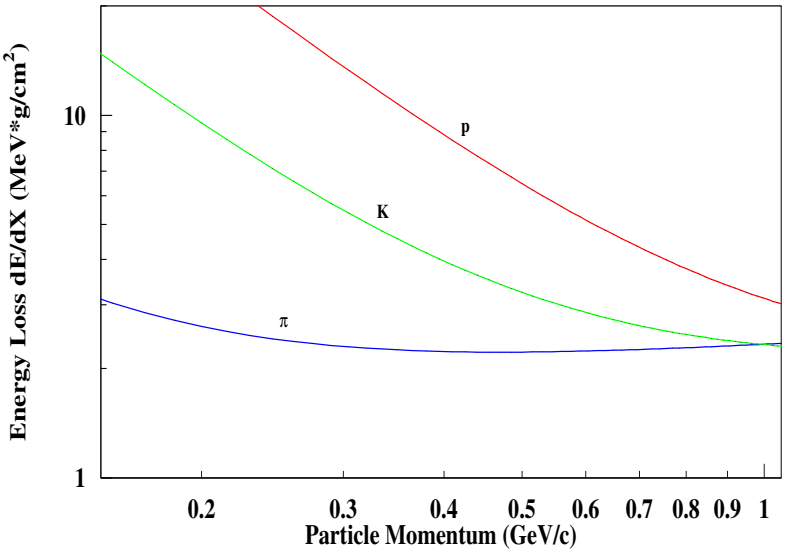

Figure 14: Proton PID by dE/dx in the Recoil Proton Detector. The graph shows ionization energy losses versus momentum for pions, kaons and protons.

To demonstrate possibility of detection of recoil protons, we simulated their tracking from target to detectors. Packets of protons of 400 MeV/c low momenta were generated at the center of target, each at a certain direction pointing to detectors. The protons were traced through magnetic field and materials on the pass. Particles traverse $\sim$ $0.7\,Tm$ field integral of transversely oriented target magnetic field before reaching detectors at $\sim$150 cm from target. For 400 MeV/c momenta protons, this causes 30° bending vertically. Each packet resulted in a scattered hit pattern in the trackers due to multiple scattering from the material, with a spot size of $\sim$15 mm and 95% of hits within circle of radius 4.5 cm (Fig. 15). These results show principal possibility of detection and reconstruction of the recoil proton even at our low momenta.

4.8 Background

For experiments with open geometry setups, background conditions are of special importance. This experiment will utilize a bremsstrahlung photon beam of intensity, potentially as high as 2×10^{13} photons per second on target of 3.8% radiation length. Simple PDG based estimates for e^+e^- γ-conversion production alone yields 3%/γ probability, i.e. rates in $\sim 10^{11} Hz$ range, even a small portion of which in the acceptance may cause difficulties.

A Geant4 based simulation code was developed to study background conditions, and detector acceptances as well. The code models the target assembly (scattering chamber with its windows

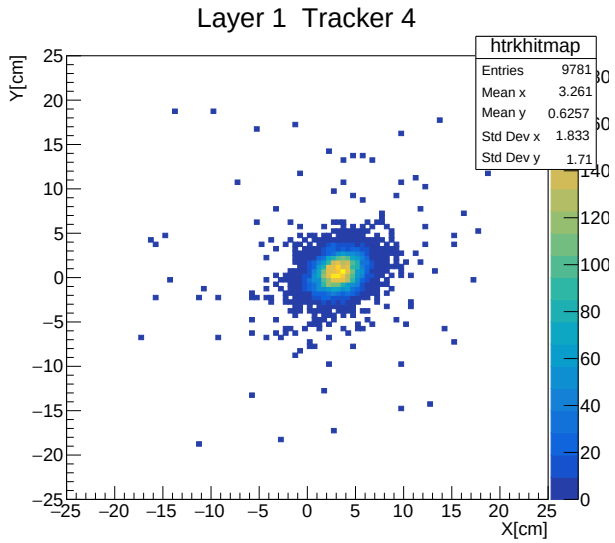

Figure 15: Geant4 simulation of tracking of 400 MeV/c protons originating at the center of target, in direction with 10° horizontal and 15° vertical deflections. Shown is hit pattern in the 1-st layer, bottom right tracker. See text for details.

and shieldings, target cell and target material, magnet coils, magnetic field) and detector package. The background events in the detectors were generated by passing bremsstrahlung photons through the target assembly. The photon energy was sampled from the bremsstrahlung spectrum with endpoint energy of 11 GeV.

It was found that among background tracks within the detector acceptances $\sim$90% are γ-s, $\sim$10% are electrons and $\sim$0.2% are positrons. The hadron content is small. Deposited in the calorimeters energies are mostly below 400 MeV. While vast majority of energetic electrons and positrons from γ-conversion in the target material fall into the gap in the middle of acceptance, some of them hit the calorimeters and deposit energies in GeV range.

The transverse magnetic field from the target deflects charged background toward detectors. Parts of detectors close to the middle of acceptance are affected with high background rates (Figure 16). The rates vary by an order of magnitude from edge to edge.

With an incident flux of 2×10^{13} photons per second (above 10 MeV), the background rates in the trackers will be at most 60 MHz/cm^2. This is not a problem, as GEM technology can withstand rates up to 100 MHz/cm^2 [86].

Background rates in the calorimeters can be significantly reduced by posing threshold on read signals (Fig. 17). Putting threshold of 200 p.e., which is equivalent to $\sim$50 MeV of deposited energy, will constrain the rates below acceptable limit (Fig. 18).

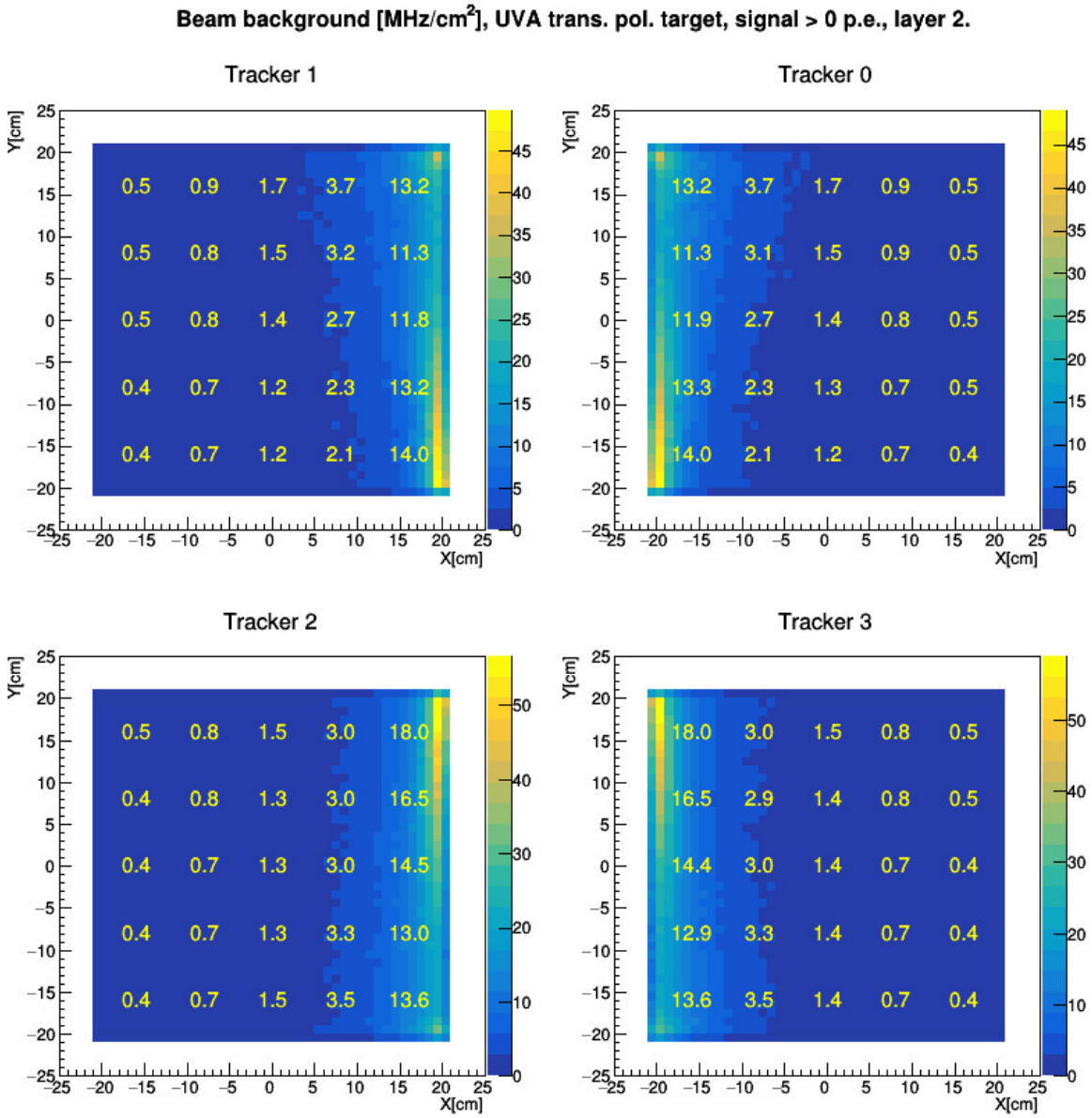

Figure 16: Background rates in the 2-nd layer GEM trackers, integrated over the CPS beam energy from 10 MeV to the end point 11 GeV, for the integrated beam intensity 2×10^{13} photon/s. Hits with non-zero energy depositions in the drift regions of GEM-s are counted. The numbers denote rates in MHz/cm^2 averaged over 5×5 cm^2 area.

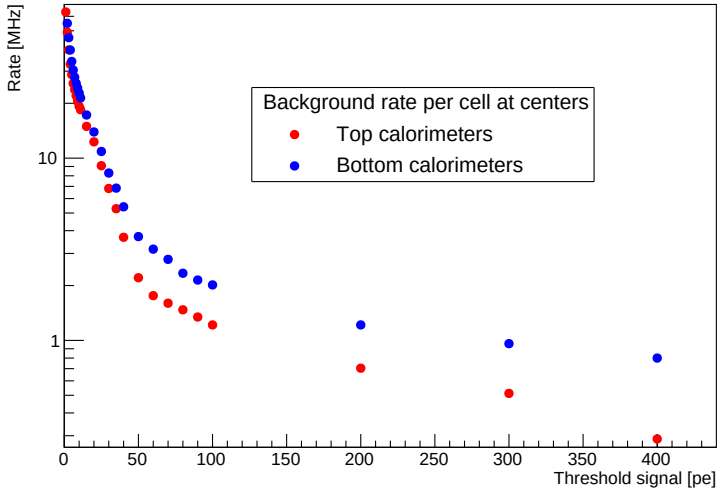

Figure 17: Background rates in the modules at the middle of top and bottom calorimeters versus low threshold signal. The rates are integrated over the CPS beam energy from 10 MeV to 11 GeV end point, the integrated beam intensity is 2×10^{13} photon/s. Note that 1 MeV energy deposition from electromagnetic projectiles yields $\sim$4 p.e. PMT signal on average.

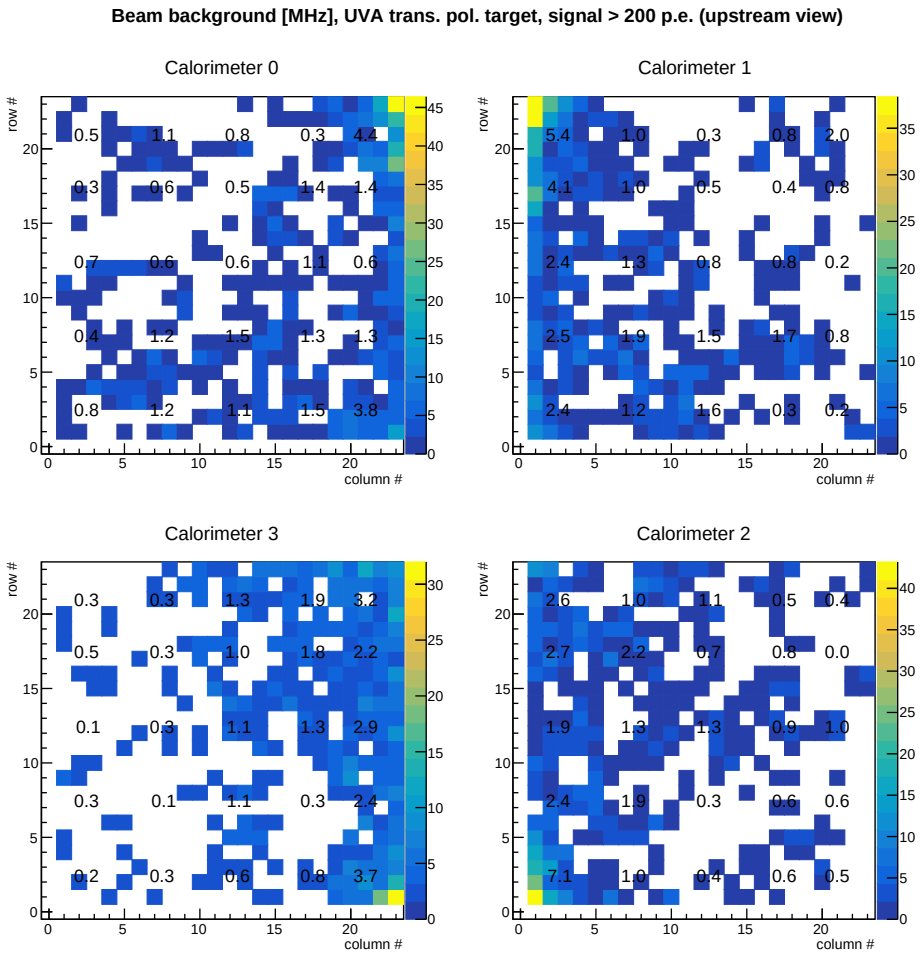

Figure 18: Background rates in the modules of calorimeters, integrated over the CPS beam energy from 10 MeV to maximum of 11 GeV, for the integrated beam intensity 2×10^{13} photon/s. Hits with signals greater than 200 p.e. are counted. The numbers denote rates per module in MHz averaged over 5×5 clusters of modules.

4.9 Trigger

For construction of a viable low level trigger, identification of the ranges of useful events is necessary. For loose cuts on the TCS kinematic variables of interest $9\ GeV^2 > Q^2 > 4\ GeV^2$, $.1 < -t < 1\ GeV^2$, $s > 4\ GeV^2$, the momenta of leptons from detected BH events are greater than $1\ GeV$, and the sum of lepton momenta is greater than $5\ GeV$ (Fig. 19).

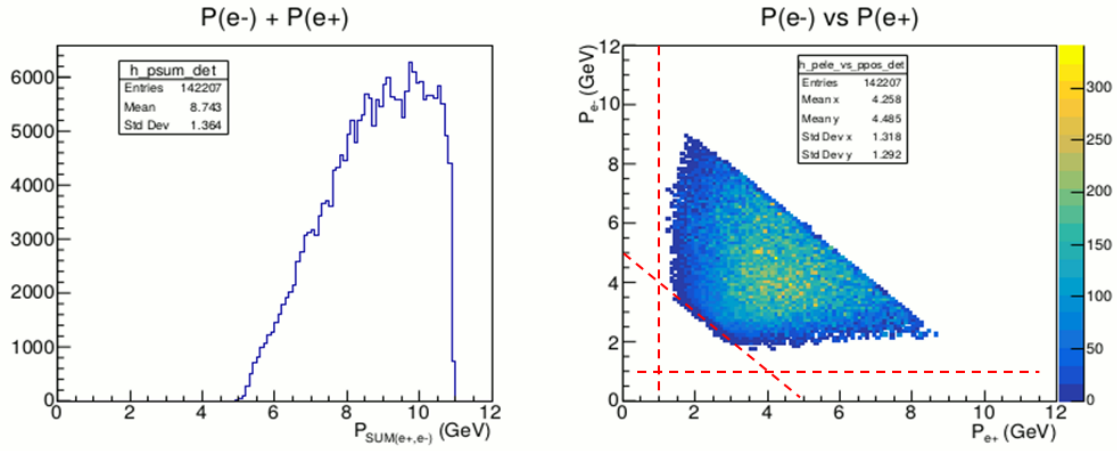

Figure 19: Lepton momenta of Bethe-Heitler events within acceptance of the TCS setup. Left: Sum of the momenta. Right: electron momentum versus positron momentum. The dashed lines indicate thresholds on the electron and positron momenta greater than 1 GeV, and sum of the two greater than 5 GeV.

A reliable hardware trigger can be constructed based on high amplitude signals from detection of the outgoing leptons in the calorimeters. The simulations indicate that in more than 95% cases the leptons in acceptance hit opposite quadrants of the detector setup. For an open geometry experiment with high level background particle fluxes, a guiding principle of trigger construction would be keeping the accidental coincidence background under control. We consider accidental coincidence rate in the range of tens of kHz within 50 ns coincidence time window to be acceptable for a DAQ electronics to operate.

Based on simulations, accidental background rate can be reduced to less than 120 kHz by establishing thresholds at 2.5 GeV on the maximum energies of the hit clusters in the calorimeters of opposite quadrants, and 6 GeV threshold on the sum of the energies in addition. The rate reduces further to an acceptable 60 kHz by excluding from trigger high background parts of the calorimeters which are close to the beam pipe by less than 8° in polar angle. Efficiency of such a trigger would be $\sim$72%.

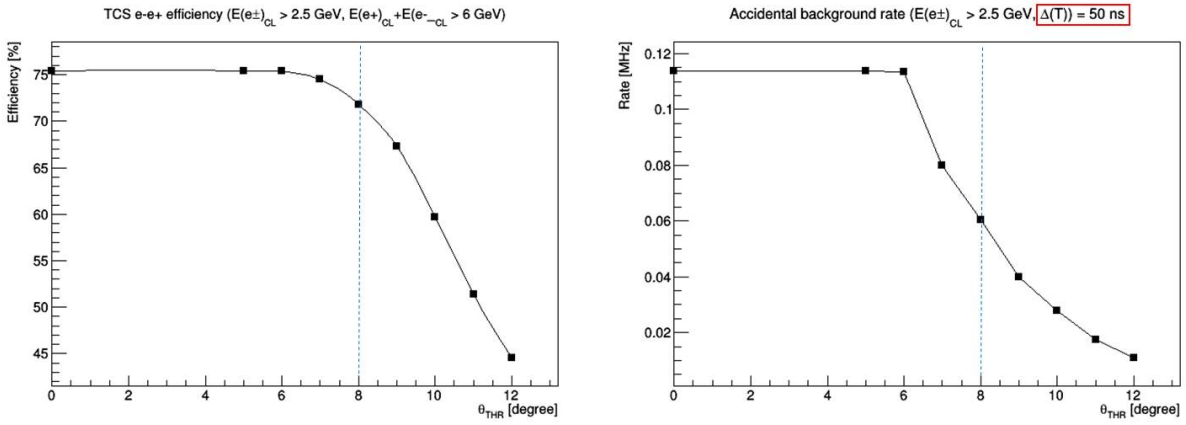

Figure 20: Performance of the proposed TCS trigger. Left: Efficiency versus threshold on polar angle θ to exclude high background rate regions. Right: accidental coincidence rate versus θ. See text for details.

5 Projections

5.1 TCS+BH simulations

We generated TCS+BH events from the DEEPGen event generator [87, 88], based on the calculations described section 3. It provides unpolarized and polarized cross sections with separated weights for "pure BH" and "total TCS+BH", to perform systematic studies on where the contribution of TCS is enhanced. For counting rate projections, we included only GPD H in TCS parametrization to limit model dependence (we will later show the impact on the size of asymmetries). At generator level we apply cuts to avoid regions of near-singularities in BH, that would otherwise create artificial spikes in generated events [89]. It corresponds to events with one of the lepton taking most of the energy and going very forward, these events are generally out of acceptance. We provide more details in Appendix C. We set the target polarization to be along x-axis, and the beam energy is following a Bremsstrahlung distribution.

The cuts applied on reconstructed events are explicited Table 2. We don't apply any cut on ϕ_S, and cuts in ϕ are correlated with the kinematics and with θ. A total of 7 kinematic bins in (ξ, t, Q'^{2}) is defined, as displayed Fig. 21. For each of these bins, we have 16 bins in ϕ and 16 bins in ϕ_S. All projections are integrated over θ. We base our observation in the rest of this section on the 2d and 3d -t bins, due to the limited proton tracking resolution at .1<-t<0.2 GeV^2 (consequence of the magnetic field). Counting rates for pure TCS+BH signal in each of the 7 kinematic bins are are presented Fig. 22. Distributions in ϕ at .1<-t<0.2 GeV^2 have a different shape than for larger values of -t, due to impact of the $\theta_{min,max}$ cut in these bins.

Variable and cut	**Comments**
Acceptance	
p(p) >0.1 GeV	for proton tracking accuracy
E(e^+ or e^-) > 0.7 GeV	trigger threshold
(E(e^+) + E(e^-)) > 5 GeV	trigger threshold
2 leptons + 1 lepton tagged	as determined by trigger and NPS cluster
± 4 cm vertical band at calorimeter level	avoid high background rates
Kinematics	
5.5 < E_γ < 11 GeV	most selected events have $E_\gamma > 7.5$ GeV
.1 < ξ < .35	statistically correlated with E_γ cut
4 < Q'^{2} < 9 GeV^2	above the region of meson resonances and below J/Ψ
0.1 < -t < 1 GeV^2	limited statistics above 1 GeV^2, proton tracking below .1 GeV^2
30° < θ < 150°	staying away from BH peaks
''$\theta_{min,max}$ versus ϕ"	staying way BH peaks: see Appendix C

Table 2: Cuts on reconstructed events

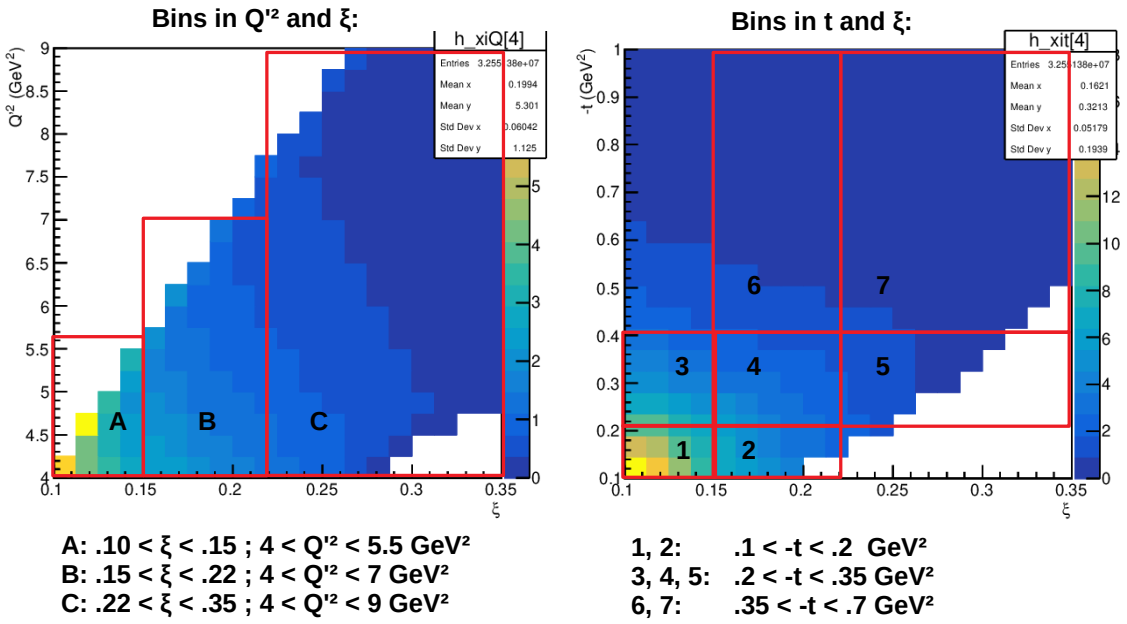

Figure 21: Phase space binning for the TCS+BH analysis in ξ and Q'^2 (left) and in ξ and -t (right). A total of 8 kinematic bins is used for the analysis.

5.2 Analysis and Signal Extraction

In previous versions of this proposal, we proposed 2 different methods for our analysis. The first one, privileged in 2018 was to use standard signal to background methods and exclusivity cuts. The second one, privileged in 2020 (see Appendix D) in addition to the standard cut method was to implement machine learning techniques. However, we realize that machine learning techniques are still in progress, not fully understood as of today, and present some unnecessary challenges for what is a simple analysis. We expect to be comparing various techniques in the future, once we have data, but decided in this document to present our projections in a more standard way and to show unbiased uncertainties and resolutions projections.

5.3 Kinematic Resolution and exclusivity

We smeared all the 4-vectors using a 12% energy resolution for the proton and a $\delta\theta_{lab} = 0.003849$ for its absolute angular resolution. We used the following parametrization to calculate the momentum resolution of the leptons, as in Ref. [82] (NPS resol):

$$\sigma = \sqrt{a^2 + \frac{b^2}{p} + \frac{c^2}{p^2}}, \tag{3}$$

with a=0.009, b=0.025, c=0.010 and p is the lepton momentum. Resolution in kinematic variables is shown Fig. 23. We also defined the exclusivity variables from the balance between initial and

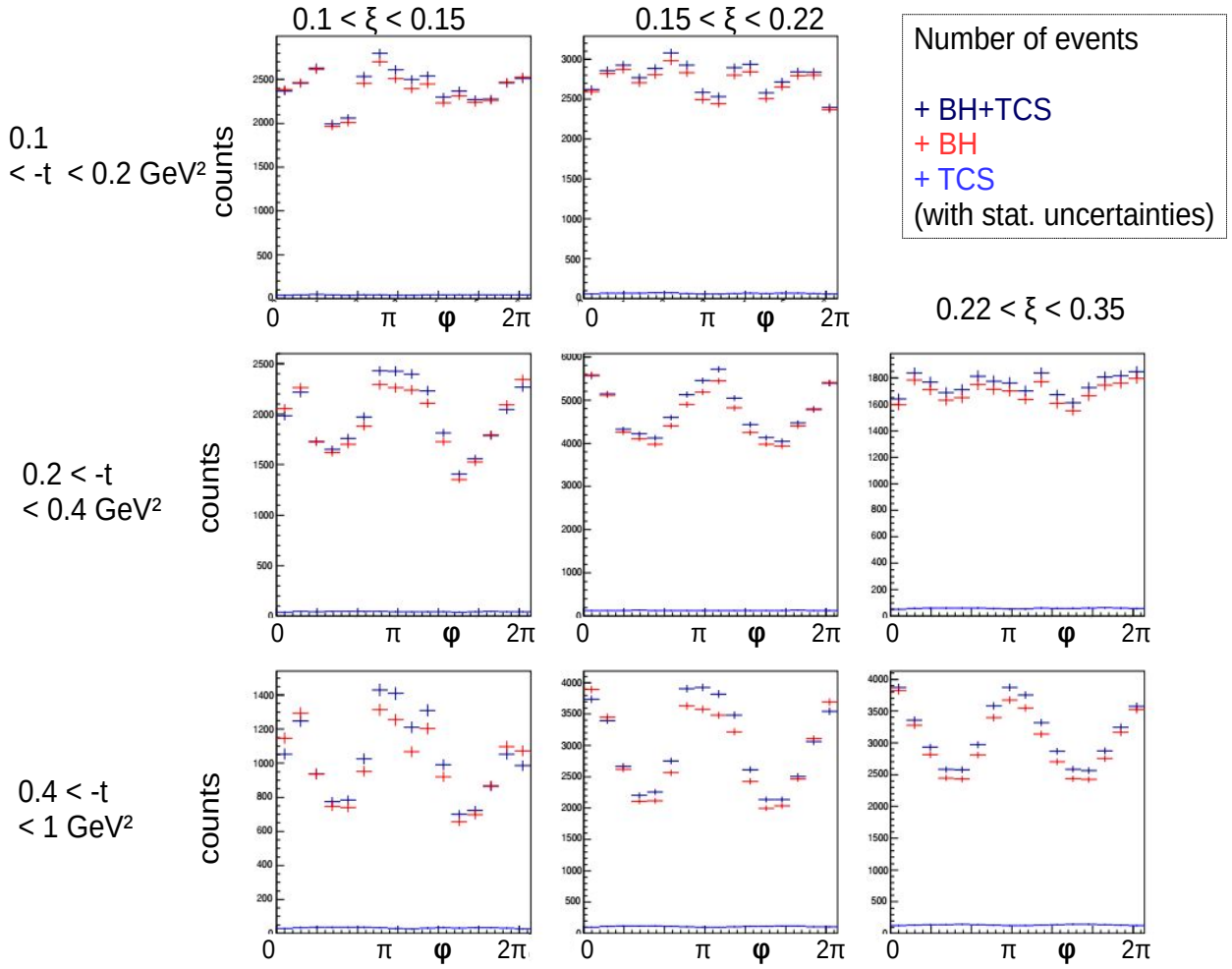

Figure 22: Counts after cuts and acceptance in each kinematic bin (different panels as indicated), for 16 bins in ϕ. Events are weighted by BH "only" rates (red), BH+TCS rates (dark blue) and TCS "only" rates (light blue, very low rates).

final states of TCS+BH events:

- Missing mass squared: $M^2_{miss} = (P + \gamma - e^+ - e^- - P')^2$
- Missing azimuthal angle: $\Delta\phi = \phi(e^+ + e^-) - \phi(P)$ (ϕ refers to arbitrary lab axis).
- Transverse missing momentum $\Delta p_T = p_T(e^+ + e^-) - p_T(P)$.

We will select events from these variables with kinematic dependent correlated cuts.

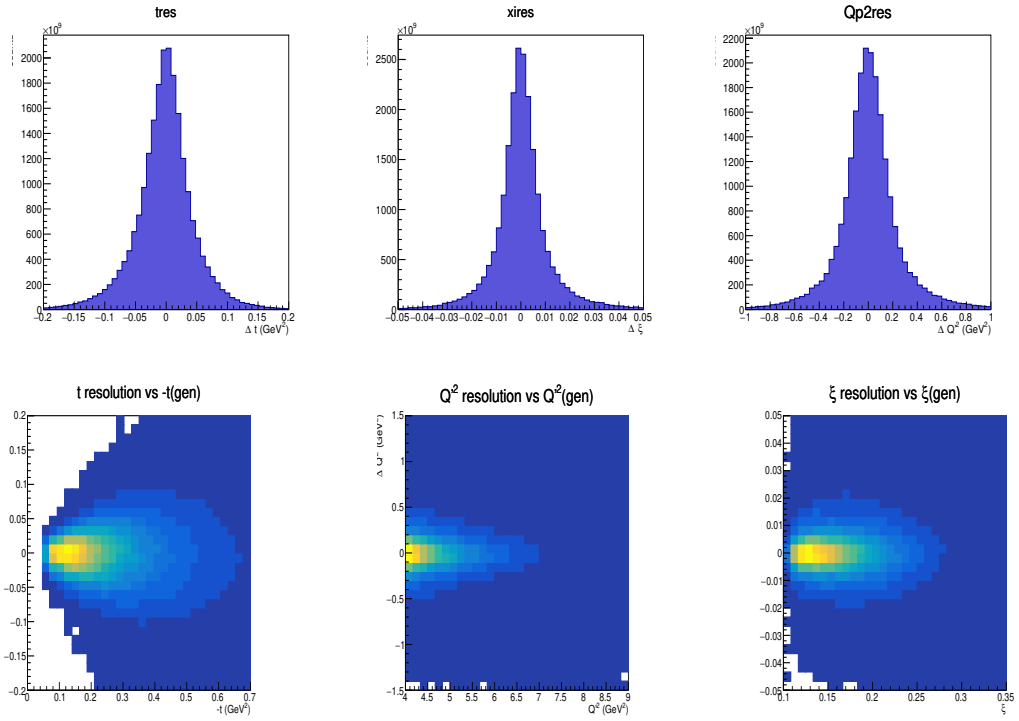

Figure 23: Resolution in kinematics: Top row: resolution in t (left), ξ (center), Q'^{2} (right). Bottom row: Evolution of the resolution (2-dim). Left: $\delta(-t)$ vs -t, center: $\delta(Q'^2) vs Q'^2$, right: $\delta(\xi) vs \xi$. Distributions are integrated over all other kinematic variables.

5.4 Physics background

Hadron background

The main source of physics background comes from the formation of $\pi^+\pi^-$ pairs. By staying above 4 GeV^2 for the photon virtuality, and below 9 GeV^2, we suppress the resonant production, including tails of mesons, as we are in a range without resonance, and have a resolution (as shown in previous subsection) sufficient to cut out meson peaks. The exclusivity request in addition to the kinematic we are running at is suppressing most of the semi-inclusive events. Therefore, most of our background comes from exclusive pion pair events, and other contributions can be neglected.

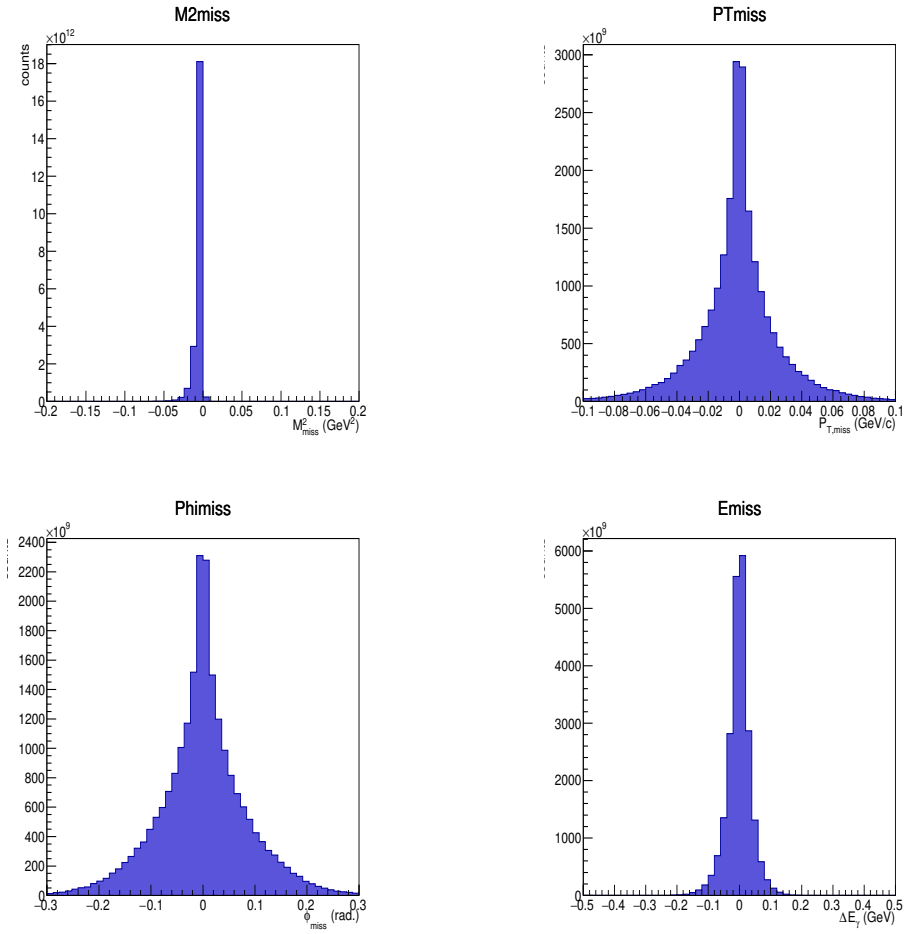

Figure 24: Exclusivity observables, integrated for all selected events.

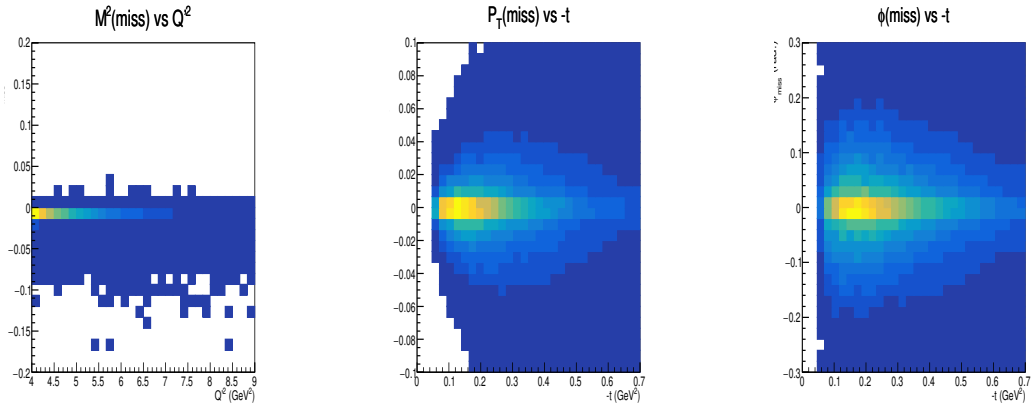

Figure 25: Evolution of exclusivity with kinematics. From the left to the right: missing mass squared versus Q'^{2}, missing azimuthal angle versus -t, missing transverse momentum versus -t.

Indeed, the mass of pions being small, most of the exclusive pairs remains after applying our exclusivity cuts (see [90, 91]).

The pion suppression in the electromagnetic calorimeters is on the order of 10^3 to 10^4, typically. Studies of the e^+e^- over $\pi^+\pi^-$ pairs ratio and pion discrimination for measurements of the e^+e^- continuum is has been performed by the GlueX collaboration for the studies of J/Ψ photoproduction near threshold [92] (and other studies not yet published). The rates strongly depend on the analysis cuts, and GlueX has a different spectrometer acceptance than us and a significantly lower acceptance. From extrapolating their results, we estimated a worse case (but unlikely) scenario of 30% contribution, a more optimistic case of 10% contribution, and a more realistic case (used in this proposal) of 20%. The resulting systematic uncertainty after all cuts are applied and this background is subtracted is 3%. We neglect the contribution to the asymmetry of such events, and consider them as an additional background dilution factor, which is taken into account in our systematics.

Lepton background

The lepton background for either inclusive or exclusive channels is quite small. As an example if we use the tail of the J/ψ and study the final state e^+e^-p we get an upper limit of $6X10^-4$ nbarn for our high Q^2 range and drops off fast for our central values. While it will not be possible to distinguish the softer part of the radiative tail and of the associated π° reaction tail, these two kind of emissions can be neglected in regard of our statistic uncertainties, and due to the fact they are suppressed by $\sim \alpha$ compared to non-radiative events.

Δ resonances and associated production

We found that Δ and associated production events are suppressed at our kinematics thanks to the detection of the recoil proton. We used a basic model with smearing of the proton momentum, which can be completed by further studies. However, this result is compatible with a similar studies we did using a recoil proton detector for COM- PASS, at a similar kinematic for the proton, which demonstrated negligible contribution (<1%) from such events. Such resonance suppression was achieved by applying exclusivity cuts to the recoil detector information, despite the resolutions on the proton momentum and energy were much broader in the COMPASS case than in our present experiment [93, 94]. Therefore, we neglect proton resonances and low energy associated production in our physics background for this experiment.

Other negligible sources of background

We assume the triple coincidence accidental rates being suppressed by exclusivity cuts. Other backgrounds include gamma conversion and π^0 events, which can be estimated from simulations,

but are considered here as negligible, due to their cross sections at our kinematics, and the very different signature of such events in the detectors.

Radiative events

Radiative corrections have not been included in our projections, however we generated such events for TCS+BH. Our results are compatible with theoretical predictions from [95], (10%), however we haven't performed systematic comparisons of our simulations versus model predictions. The formalism used in our radiative corrections is based on [96] and corrections have been implemented directly as sub-processes in our event generator (latest DEEPGen version).

5.5 Kinematic Dilution Factor (target)

The figure of merit for this type of polarized target experiment is proportional to the active target contribution squared times polarization squared. The active target contribution is made of the dilution factor and the packing fraction over the length of the target. The packing fraction can be measured using a method of cryogenic volume displacement measurement which compare an empty target cell to the full target cell used in the experiment. The target cell is filled with beads of solid NH_3 material with a typical packing factor of about 60% with the rest of the space filled with liquid helium.

The dilution factor is the ratio of the number of polarizable nucleons to the total number of nucleons in the target material and can be defined as,

$$f = \frac{N_H \sigma_H}{N_N \sigma_N + N_H \sigma_H + \Sigma N_A \sigma_A}, \tag{4}$$

where N_H is the number of hydrogen nuclei in the target and σ_H is the corresponding exclusive differential scattering cross section, N_N is the nitrogen number of scattered nuclei with cross section σ_N, and N_A is the numbers of other scattering nuclei of mass number A with cross section σ_A. The denominator of the dilution factor can be written in terms of the relative volume ratio of NH_3 to LHe in the target cell, the packing fraction p_f. For the case of a cylindrical target cell oriented along the magnetic field, the packing fraction is exactly equivalent to the percentage of the cell length filled with NH_3. The material density for NH_3 is 1.007 g/cm^3 and the target radiation length is about 5.7%. The uncertainty in these factors from irreducible background is typically 2-3% considering the ammonia density and packing fraction as well.

In terms of target nuclei accounting the dilution factor for NH_3 is 0.1775 when considering the 3 hydrogen to the one nitrogen per molecule, but there is a kinematic dependence to each cross section. There are also more materials in the experimental beam path than just the NH_3, which means the amounts and cross-sections of those materials must also be accounted for when calculating the kinematically sensitive dilution factor. Due to this, the dilution factor of the target

will actually be given by the equation

$$f = \frac{3d^4\sigma_H^{\gamma p \to pe^+e^-}\left(W_{\gamma p}, -t, \theta, Q^2\right)}{\sum_A N_A d^4\sigma_A^{\gamma p \to pe^+e^-}\left(W_{\gamma p}, -t, \theta, Q^2\right)}. \tag{5}$$

Here A is required for each nuclei in the beam path. Background that are not from TCS that are indistinguishable from the $\gamma p \to pe^+e^-$ process contribute the most. This would include processes like $\gamma p \to p\pi^+\pi^-$ which dominates our background. To estimate the kinematic dilution factor a modified version of Pythia was used with cross sections scale to our kinematic. The detection of relevant processes off the nitrogen are reduced in our acceptance however the cross section of nitrogen in the $\gamma p \to p\pi^+\pi^-$ higher reducing any advantage.

Q^2-bin	$< Q^2 >$	NH_3		NH_3+A		Full
		f	d_π	f	δf (%)	$\delta f(\%)$
4.0 -5.6	4.9	0.200	0.66	0.196	0.5%	2.3%
5.6 - 7.1	6.3	0.211	0.73	0.210	0.7%	2.5%
7.1 - 8.3	7.8	0.208	0.75	0.203	0.9%	2.6%
8.3 - 9.0	8.4	0.211	0.68	0.208	1.9%	2.8%

Table 3: Here will list the dilution factor estimates after our DNN analysis based on photoproduction cross sections of the dominate background with kinematic sensitivity for four kinematic bins for pure ammonia (NH_3) as well as for the contribution from all materials (NH_3+A), as well as the total with contribution from packing fraction and target density in (Full). Errors contain contributions from both statistical and systematic uncertainty estimates.

To estimate the contribution from other materials in the beam path such as the aluminum windows, the target cell material, the NMR coils, the liquid Helium, and the target ladder, estimates are used from the geometry we have constructed in Geant4. Rate contributions can be obtained by analyzing the percentage that make it into our acceptance and kinematic constraints. These materials generally have a higher cross section as well compared to hydrogen however there is very little interaction with these materials. Table 9 shows the resulting dilution factor from pure NH_3 as well as from the combination of all material in the beamline, shown in column (NH_3+A). We also show in column (Full) the combined error estimation from the dilution factor, the target packing fraction, and the NH_3 density, but this does not include the pion background contribution error.

Also included in Table 9 is the estimated ratio of TCS events to $\gamma p \to p\pi^+\pi^-$ in the column indicated by TCS/π. The pion background will be significant even with the NPS pion suppression. This background will likely have its own asymmetry which we will measure to be able to isolate the TCS asymmetry. This can be done by taking slices of our event distribution to isolate the pion background and calculating the target asymmetry $A_N^{\pi^+ + \pi^-}$. Then do the same for kinematic cut where both contribute and calculate the target asymmetry $A_N^{TCS+(\pi^+ + \pi^-)}$. From this we extract A_N^{TCS}. This is a common practice for these types of asymmetry measurements. For more details on dilution factor calculation and cuts, see Appendix D.

Beam dilution and polarization transfer

In case of an additional measurement of double spin asymmetries out of the naturally polarized photon beam, the uncertainties are dominated by the target dilution factor, as detailed above. Contribution to the dilution and systematics from beam polarization can be neglected in regards to the target, it is assumed to be at the percent level.

The JLab electron beam polarization is assumed to be larger than 85%. We calculated the secondary bremsstrahlung photon transfer factor to be from 85% (7.5 GeV photons) to 100% (11 GeV photons), as shown in Fig. 26. On average, we estimate a photon beam polarization transfer factor of ∼75%.

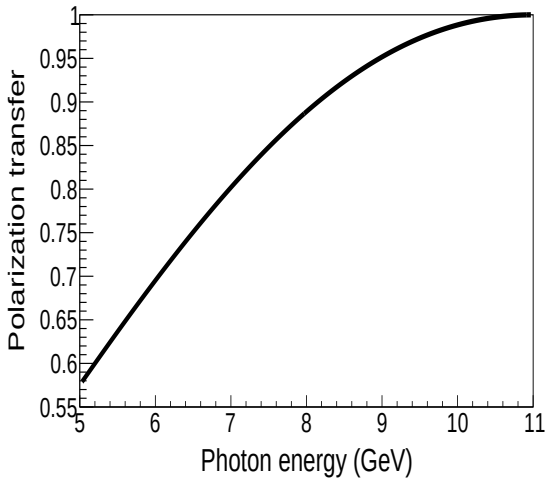

Figure 26: Circular polarization transfer for Bremsstrahlung photons initiated from a 100% polarized 11 GeV electron.

5.6 Systematic uncertainties

Many JLab experiments use the UVA/JLab target but this along with WCAS would be the first to use a rotating target raster. We estimate that with careful control of rotation with a NMR coil that does not brush against the rotating cell that a similar uncertainty can be achieved as past polarized target experiments. We also try to leave room for the unexpected so we estimate a systematic error contribution from the rotating polarized target at around (5%). We expect to be able to measure the packing fraction for each load of the target during the experiment.

Charge calibration and detector efficiencies are expected to be known better to 1%. Detector resolution and efficiency is also expect to contribute less than 1%. The signal extraction error will be minimized using a multivariate techniques leading to only a few counts of background slipping into the final result. The systematic error on resolving the Compton signal is dependent on the

Source	Systematic
Target Polarimetry	5.0%
Beam Polarimetry	1%
Packing fraction	3%
Trigger/Tracking efficiency	1.0%
Background subtraction	3.0%
Total	$\sim 6.7\%$

Table 4: Estimation of the systematic errors.

background produced at that kinematic point. A larger background with smaller signal naturally results in a larger error. By considering a larger than expected background we can estimate the expected systematic error from a plausible analysis. We expect less than 3% background which is a estimate directly based on the Monte Carlo. Estimated systematic uncertainties are summarized Table 4.

5.7 Results

In this section, we selected the 4^{th} bin for reference (.15<ξ<.22, .2<$-t$<.4 GeV^2, 4<Q'^{2}<7 GeV^2). Fig. 27 (top part) is a one dimensional projections of the transverse target spin asymmetry for 8 bins in ϕ_S, displayed as a function of ϕ. Uncertainties shown include statistics (largely dominant) and target polarization and dilution factors. We smeared each point with a Gaussian function. Figures of merit for these 1-dim projections are displayed Fig. 27 (bottom part). CFFs will be extracted by fitting simultaneously the orthogonal ϕ_S bins, i.e. top row versus second row, same columns (we plan to develop 2-dimensional fits in the future). Therefore in a ''naive" uncertainties estimate, we can combine part of the errors of correlated bins. For illustration, we included on each ϕ_S panel curves corresponding to fits by the dominant $A\ sin(\phi - \phi_S)$ moment of the asymmetries. The blue curve is the expected one, the red curve is a fit attempt to display an instance of the distribution. Projections for all kinematic bins are provided in Appendix E.1 (asymmetries) and E.2 (FOM). Combined relative uncertainties on moments for each kinematics are presented in Appendix E.3 (Fig 57).

As mentioned in section 5.1, our experimental projections are for TCS amplitudes calculated with only GPD H. We display Fig. 28 (top part) the asymmetries in bins of ϕ_S as a function of ϕ for different model scenarios, calculated for our reference kinematics. In this exercise, we use several values of J_u and J_d in the parametrization of GPD E. We use only one variant of VGG model (see [7] for the GPD E parametrization). We choose the same sets of values for J_u and J_d than [20]. The black curves (with label ''H only") are from the same model version than used for our experimental projections. Bottom part of Fig. 28 is a projection of the maximum of these asymmetries (its size at $\phi = \phi_S + 90°$), as a function of ϕ_S. We observe that the size of the asymmetries vary by up to 0.15 at $\phi_S = 90°$ between the two extreme cases presented (0.07 for the cyan curve and 0.23 for the pink curve), and up to 0.09 at $\phi_S = 0°$ (0.07 for the cyan curve and 0.16 for the pink curve). This

demonstration reflects a strong sensitivity of the asymmetries to the GPD E and the quark angular momenta. Note that we could obtain slightly larger differences with other models given that GPD E is poorly known.

5.8 Discussion

Our projected experimental uncertainties allow for the discrimination between models for our 7 kinematics. As demonstrated in section 3 (see Fig 34), we will be able to extract the CFF $\Im E$. Note that the uncertainties on the CFFs will strongly depend on the accuracy of complementary measurements of the unpolarized and beam polarized TCS+BH cross sections (and potential other measurements): in section 3, we set the errors by exploring both the upper and low limit in all observables. The correlation between the different CFFs and the number of independent observables available for TCS+BH also has a large impact the uncertainty on $\Im E$. As a consequence of the lack of experimental data for TCS, we cannot provide quantitative estimate on $\Im E$. We would like to emphasize that our experiment will allow this extraction. The uncertainties will strongly depend both on the availability of complementary measurements and on the fitting technique (our technique is more conservative than most other models), in addition to the uncertainties from our experiment. This sensitivity to GPD E is provided by the additional information from the proton transverse polarization [6].

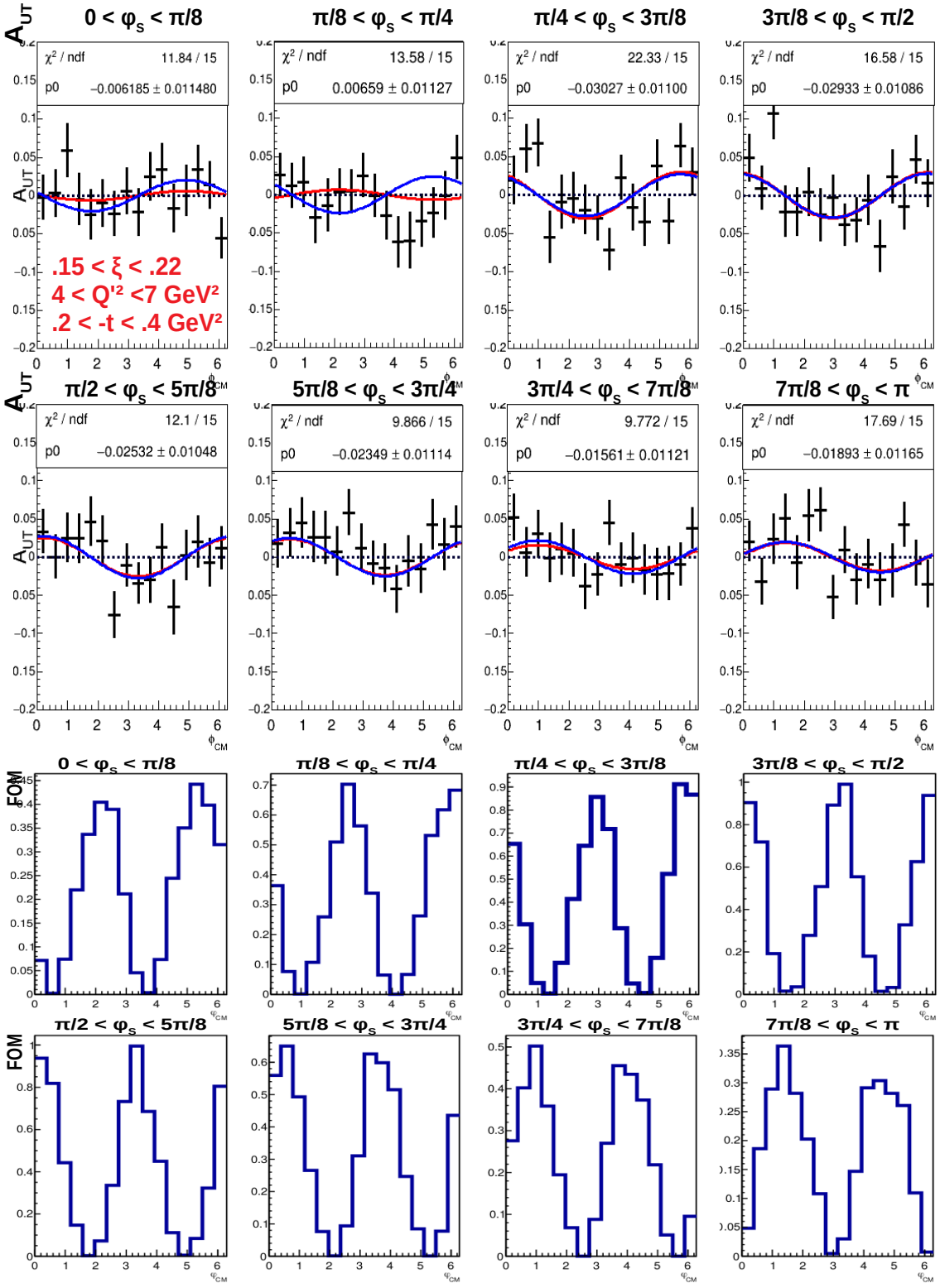

Figure 27: Top: Projection of the single transversely polarized target spin asymmetries in bins of ϕ_S (different panels), as a function of 16 bins in ϕ and for $0.15 < \xi < 0.22$ and $0.2 < -t < 0.35$ GeV^2. Statistic uncertainties are represented and correspond to an integrated photon luminosity of $5.85 * 10e5$ pb^{-1} for $5.5 < E_\gamma < 11$ GeV, and include various dilution factors. The blue curves are the fit of the generated distributions by $A * sin(\phi - \phi_S)$, the red curves are the fits of the randomly smeared distributions as displayed. Bottom: FOM for the above asymmetries.

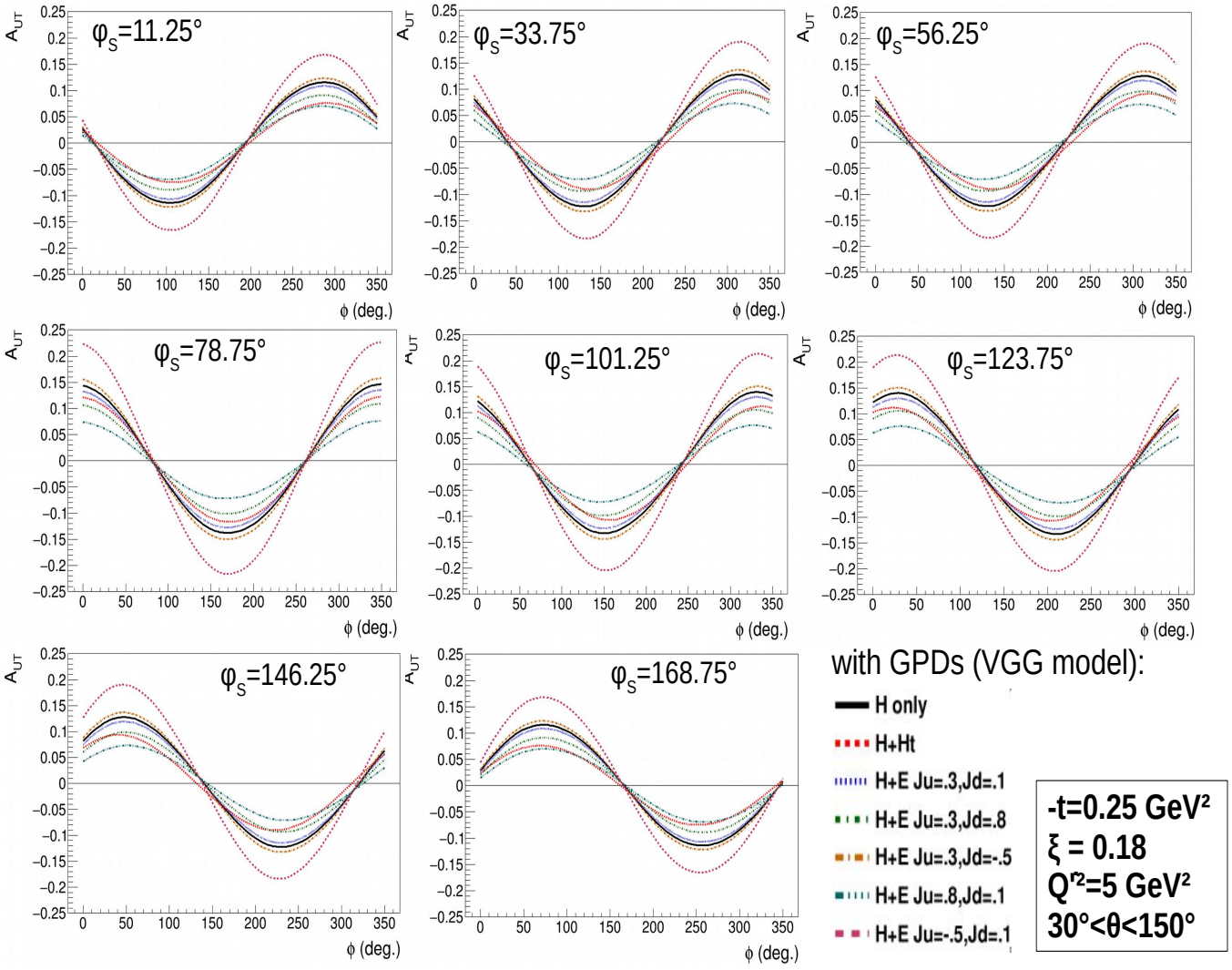

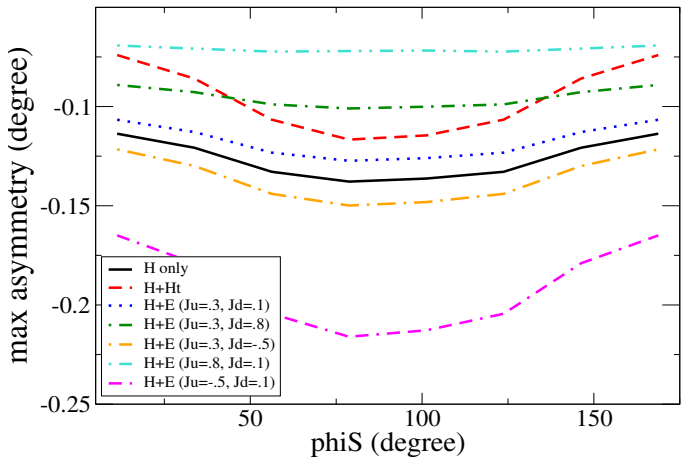

Figure 28: Top panel: transverse spin asymmetries calculated in the same bins in ϕ, ϕ_S (for our kinematic bin 4) as for experimental projections. The various colored curves correspond to different parametrization of TCS amplitude with GPDs H, $\tilde{H}$ and E, and with E parametrized with different values of J_u and J_d. Bottom panel: Projection of the maximum asymmetries as a function of ϕ_S corresponding to the different model scenarios of the top panel.

6 Beam time request

We request a total of 49.5 PAC days: 30 days are for the physics data taking (see next paragraph 6.1), 5 days are for the commissioning and checkout, and an equivalent of 14.5 PAC days (29 calendar days) are for target, polarimetry and detector overhead. We detail our needs in Table 5.

Operations	calendar days	PAC days
Installation in Hall C	5	2.5
Initial signal and electronic checkout	5	2.5
Gain matching of detector's channels with gain monitoring system	1	0.5
Decommissioning	3	1.5
Overhead (see paragraph 6.2)	15	7.5
sub-total (operations)	29	14.5
Data acquisition time	calendar days	PAC days
Commissioning with beam	10	5
Physics data taking	60	30
sub-total (beam time)	70	35
Total	99	**49.5**

Table 5: Details of our beam time request

6.1 Beam time for physics data taking and integrated luminosity

Our projections are based on 30 PAC days for the physics. We will use a longitudinally polarized electron beam with polarization >85% at an energy of 11 GeV and at an intensity of 2.5 μA. In the energy range $[5.5,\ 11]$ GeV, the secondary photon beam flux from CPS is 10^{35} photons/cm^2/s. For interaction off the 3 polarized protons of the UVa/JLab NH_3 polarized target, we obtain an integrated luminosity of 5.85*10^5 pb^{-1}.

6.2 Overhead

The incident beam causes radiation damage in the frozen ammonia, which leads to the creation of atomic hydrogen and other paramagnetic radicals in the target material. This provides an additional relaxation path for the nuclear spins, and the buildup of these free radicals leads to a gradual decay of the target polarization. The concentration of these unwanted radicals can be reduced significantly by annealing the target. The target material must be raise to of about 80-90K. Given the proposed beam intensity and single rotating target cell, we expect to require an anneal about once every 14 hours of beam time. The anneal time averages about 35 minutes but typically requires about 2.5 hours from beginning to beam ready. Because of the single target load, we expect that the material must be replaced once every 3 days of accumulated. A full shift is required to replace the insert and perform a target calibration to be ready to run again.

As of the calorimeter, our recent studies demonstrated that the integrated radiation load stays low enough in the most exposed blocks of the calorimeter for the duration of the experiment and no overhead is expected if we run in normal conditions.

Overhead	Number	Time Per (hr)	total (hr)
Polarization/depolarization	60	2.0	120
Target Anneals	15	4.0	60
Target T.E. Calibrations	10	4	28
Packing fraction/Dilution runs	6	2	12
Target Material Change	8	4	32
NPS Crystal Recovery	1	24	24
BCM/BPM Calibration	8	2	16
Moller Measurements	1	1	42
Total Overhead			346 (14.4 days)

Table 6: List of contributing factors to the overhead time

7 Conclusion

We are presenting this proposal as an update of our C2 conditionally approved proposal C12-18-005 after PAC 48. We worked on improving the experiment, took into account the suggestions we got and addressed the concerns brought up to us by previous PAC and TAC committee members.

Our goal is to measure transverse proton spin asymmetries for the TCS+BH reactions and their azimuthal dependence in bins of ϕ (lepton plane vs reaction plane) and ϕ_S (proton spin direction vs reaction plane), in different kinematic bins in ξ and t. The azimuthal study allows to disentangle the Compton contribution from the TCS+BH interference term, which dominates in these asymmetries. We presented a method for extracting Compton Form Factors and indirectly GPDs out of these data, which we put in perspective of other potential TCS+BH measurements and forthcoming DVCS+BH measurements at similar kinematics with a similar precision level. We demonstrated the feasibility to extract CFFs and GPDs, with unprecedented accuracy, in particular the poorly known but extremely important GPD E. The GPD extraction will be done in several ξ and t bins, therefore we are drastically reducing the theoretical uncertainties on the value of real parts of CFFs (dependent on resolutions mainly in ξ, but also in t), and in consequence the GPDs. It is minimizing the systematic effects related to higher twists (dependent on the t range), and allows to study these effects by comparing different bins in t.

This measurement will take place in Hall C, using a real photon source (Compact Photon Source, CPS), electromagnetic calorimeters (Neutral Particle Spectrometer, NPS), recoil proton detectors (Hodo/GEM-pack), and a transversely polarized proton target (NH_3 UVa/JLab target).

The main physics goals of this experiment are:

1. Extraction of the CFF $\Im E$, and provide constraints on the GPD E of the proton and on the quark angular momenta. It will contribute to the understanding of the nucleon's partonic spin structure.

2. Study of GPD universality and higher twist effects due to a unique comparison of results from a spacelike (DVCS) and timelike process (TCS). Our experiment is not sufficient in itself to provide these studies and compare to the large data sets already available for the DVCS+BH reaction to compare to. However, it is essential to bring enough precision in the measurement of the GPD H extracted solely out of TCS+BH, in complement to unpolarized and beam polarized precision measurements of TCS+BH in other experiment.

3. Complement experimental set of observables accessing GPDs due to two new independent transverse target spin asymmetries, not measured in any other experiments in any Halls at JLab, including DVCS+BH experiments.

We would like to emphasize again that our measurement will provide access to GPD E of the

proton specifically. Other groups have emphasized in the past that GPD E can be extracted out of DVCS+BH neutron measurements that have already been done in Hall B, but this statement is incorrect: indeed, in that case, the GPD of the neutron is extracted, and can't complement in itself the data set of observables sensitive to proton's GPDs, as we are intending to do.

We are taking advantage of the incredible expertise allotted to us from the NPS and CPS collaborations [47, 46]. The main hardware developments for the successful running of the proposed experiment are the additional electromagnetic calorimeters, NPS, a recoil proton detector based on GEM and a Hodoscope, as well as the CPS and the rotating target system.

The NPS collaboration will provide support for the necessary calorimeters. We will collaborate with experts at UVA on optimization of our GEM trackers. The CPS and polarized target system are both new and critical to the high intensity photon effort at Jefferson Lab. UVA, UNH and the JLab polarized target group will provide the necessary polarized target support. The VT group, in collaboration with ASNL, ODU, JLab will provide the hodoscopes for the tracking system. In total we need 49.5 PAC days, of which 30 are for the physics data taking (see section 6).

A Some details on TCS+BH formalism

At fixed beam energy, we express the unpolarized target cross section as

$$\frac{d^4\sigma}{dQ'^2 dt d\Omega}(\gamma p \to p' e^+ e^-) = \frac{1}{2\pi^4}\frac{1}{64}\frac{1}{(2m_N E_\gamma)^2} \mid T^{BH} + T^{TCS} \mid^2,$$

where the $\mid T^{BH}+T^{TCS} \mid^2$ term corresponds to the BH and TCS amplitudes, and m_N is the nucleon mass. The TCS amplitude reads

$$T^{TCS} = -\frac{e^3}{q'^2}\, \bar{u}(k)\, \gamma^\nu\, v(k')\, \epsilon^\mu(q)\, H^{TCS}_{\mu\nu}, \tag{6}$$

with, at the asymptotic limit,

$$\begin{aligned} & H^{TCS}_{\mu\nu} \qquad (7)\\ & = \frac{1}{2}\,(-g_{\mu\nu})_\perp \int_{-1}^{1} dx\, \left(\frac{1}{x-\xi-i\epsilon}+\frac{1}{x+\xi+i\epsilon}\right).\left(H(x,\xi,t)\bar{u}(p')\not{n}u(p) + E(x,\xi,t)\bar{u}(p')i\sigma^{\alpha\beta}n_\alpha\frac{\Delta_\beta}{2m}\,u(p)\right)\\ & -\frac{i}{2}(\epsilon_{\nu\mu})_\perp \int_{-1}^{1} dx\, \left(\frac{1}{x-\xi-i\epsilon}-\frac{1}{x+\xi+i\epsilon}\right).\left(\tilde{H}(x,\xi,t)\bar{u}(p')\not{n}\gamma_5\,u(p) + \tilde{E}(x,\xi,t)\bar{u}(p')\gamma_5\frac{\Delta.n}{2m}\,u(p)\right), \end{aligned}$$

where we used the metric:

$$\begin{aligned} (-g_{\mu\nu})_\perp &= -g_{\mu\nu} + \tilde{p}_\mu n_\nu + \tilde{p}_\nu n_\mu \ , \\ (\epsilon_{\nu\mu})_\perp &= \epsilon_{\nu\mu\alpha\beta}\, n^\alpha\, \tilde{p}^\beta. \end{aligned} \tag{8}$$

The GPDs entering Eq. 7 are proton GPDs, i.e. they read, in terms of quark flavors:

$$H_{TCS}(x,\xi,t) \;=\; \frac{4}{9}H^{u/p} \;+\; \frac{1}{9}H^{d/p} \;+\; \frac{1}{9}H^{s/p}. \tag{9}$$

We use the decomposition into GPDs and notations from Ji [4], and the GPD parametrizations from the VGG model [53, 54, 7, 55], which are summarized in Ref. [9] and based on the Radyushkin double- ansatz for the (x,ξ)-dependence [60, 61, 5] and on the Reggeized ansatz for the t-distribution [7, 55]. The BH amplitude can be expressed as

$$T^{BH} = -\frac{e^3}{\Delta^2}\,\bar{N}\,\Gamma^\nu\,N\,\epsilon^\mu(q)\,\bar{u}(k)\,\left(\gamma_\mu\frac{\not{k}-\not{q}}{(k-q)^2}\gamma_\nu + \gamma_\nu\frac{\not{q}-\not{k}'}{(q-k')^2}\gamma_\mu\right)\,v(k'), \tag{10}$$

where the 4-vectors q, k, k' respectively correspond to the photon, the electron and the positron, N is the nucleon spinor and Δ is the proton momentum transfer. The virtual photon-proton electro-

magnetic vertex matrix can be expressed as a function of Dirac (F_1) and Pauli (F_2) form factors

$$\Gamma^\nu = \gamma^\nu \, F_1(t) + \frac{i\sigma^{\nu\rho}\Delta_\rho}{2\, m_N} \, F_2(t), \tag{11}$$

We use the electric form factor parametrization from [62] and magnetic form factor parametrization from [63].

Analytic equations have been developed for the unpolarized and circularly beam polarized TCS+BH [12]. According to this work, the squared TCS amplitude, summed over the initial and final photon spin states is expressed as a function of CFFs, and is proportional to (using our notations) [12]

$$\begin{aligned} TCS^2 \propto (1-\xi^2)\left(|\mathcal{H}|^2 + |\tilde{\mathcal{H}}|^2\right) - 2\xi^2 \Re\left(\mathcal{H}\mathcal{E} + \tilde{\mathcal{H}}\tilde{\mathcal{E}}\right), \\ -(\xi^2 + \frac{t}{4m_N^2})|\mathcal{E}|^2 - \xi^2 \frac{t}{4m_N^2}|\tilde{\mathcal{E}}|^2. \end{aligned} \tag{12}$$

The dominant sin(ϕ) amplitude term (M^{--}) of the circularly beam polarized cross section decomposes into CFFs and FFs, and is proportionnal to [12]

$$M^{--} \propto F_1\mathcal{H} - \xi(F_1+F_2)\tilde{\mathcal{H}} - \frac{t}{4m_N^2}F_2\mathcal{E}. \tag{13}$$

B CFF fitting method

Set of observables	DVCS	TCS	DVCS+TCS	# independent obs. (DVCS/TCS/both)
1) σ, $\Delta\sigma_{LU}$	A, B, C	A, B, **C**	A, B, **C**	2/2/2
2) σ, $\Delta\sigma_{LU}$, $\Delta\sigma_{UL}$, $\Delta\sigma_{LL}$	B			4/4/4
3) σ, $\Delta\sigma_{LU}$, $\Delta\sigma_{UT}$ (x2)	B$^{(*)}$	**C**	B+C$^{(*)}$	4/4/4
4) σ, $\Delta\sigma_{LU}$, $\Delta\sigma_{UT}$ (x2) $\Delta\sigma_{UL}$, $\Delta\sigma_{LL}$				6/6/6
5) σ, $\Delta\sigma_{LU}$, $\Delta\sigma_{UT}$ (x2) $\Delta\sigma_{UL}$, $\Delta\sigma_{LL}$, $\Delta\sigma_{LT}$ (x2)				8/8/8
6) σ, $\Delta\sigma_{LU}$, $\Delta\sigma_{C}$		x	x	3 (DVCS)
6') σ, $\Delta\sigma_{\odot U}$, $\Delta\sigma_{LU}$	x		x	3 (TCS)
6'') 2) of DVCS + 3) of TCS	x	x	B+**C**	6 (DVCS+TCS)

Table 7: Set of observables generated for DVCS and TCS, and number of independent observables in the fits. The letters in columns 2, 3, 4 indicate the Halls where these observables can be measured. Bold C is our experiment.

All the distributions we generated and used for extracting the CFFs are shown on Fig. 29 (DVCS+BH) and 30 (TCS+BH). We combined these observable in various "sets" to reflect different scenarios where we would only have data for the beam spin asymmetry (BSA), or for both the BSA and unpolarized cross section, or for these 2 observables and the transverse target spin asymmetries, etc. The sets we used for interpretation in this document are presented Table 7.

Rather than directly fitting the CFF, we extract coefficients of the generated CFFs values from these observables. We limit the variation of all the coefficients during the minimization procedure to stay in a range of $[-5, +5]$ times the generated value. It allows for forcing the under-constrained fits to converge, otherwise some of the fits parameter may take infinite values. Impact on uncertainties is discussed in [69]. It may lead to ''double solutions" for some cases, however we can easily discriminate the ''wrong" solution by either reproducing the fits within a different range if generated values or by studying the correlation between the coefficients. The correct solution is always stable, while the incorrect one is not. Wrongly extracted parameters are indeed strongly correlated with the variation range limits (one CFFs takes the value of one limit and by correlation, one or more other extracted CFFs are incorrect).

As shown on Fig. 31, the result of the fit (mean value) has a dependence on the parameter starting value as randomly generated before performing the fit. The result fluctuates around the generated value, while $\pm 1\sigma$ (min and max uncertainties) limits are the same. If we smear the generated cross sections and repeat the fits multiple times, we obtain broader distributions of the results and limits. However, as shown Fig. 32, the limits remain very stable. Our conclusion on this effect

is that when interpreting experimental data, we should consider the result being the min and max limits of the CFFs rather than its extracted mean value (in the experiment, we cannot reproduce the multiple different possibilities of smearing the cross sections in a single experiment). In this work, our mean value, min and max uncertainties are the result of the fit by a gaussian function of the multiple randomly generated instances.

Results, Interpretation In the main document (section 3.2), we are discussing our interpretations on fitting several data sets for the DVCS+BH and TCS+BH reactions. Results on extracting CFFs from Table 7 are shown Fig. 33. We extracted the CFFs from DVCS+BH only, TCS+BH only, and combining the data sets. We reproduced the exercise for several kinematics and different scenarios for the uncertainties and data smearing.

Propagation of experimental uncertainties to CFF results Since our experimental uncertainties will be larger than the ones we set in the previous exercise (intending at showing sensitivities to CFFs), we reproduced the fits of '' case 3" (unpolarized, beam and transverse target polarized cross sections) for several scenarios, for TCS+BH and for DVCS+BH. In the first attempt, we smeared each 16 point of the distributions in ϕ assuming uncertainties of 3% on the unpolarized cross sections and 5% on polarized cross sections: $\delta\sigma^{unpol}/\sigma^{unpol}$=3%, $\delta\sigma^{pol}/\sigma^{pol}$=5% (notation: scenario A). Then, we produced the following data sets: B: 5%, 7%; C: 7%, 10%; D: 10%, 14%; E: 14%, 20%; F: 20%, 28%; G: 28%, 38%. As shown Fig. 34, we can extract the same CFFs for all scenarios ($\Im H$,$\Im \tilde{H}$,$\Im E$, $\Re H$), with growing uncertainties. As for previous studies, the uncertainties from DVCS and from TCS are of the same order of magnitude, and are generally smaller by 20% to 40% out of DVCS if we assume the same uncertainties on the observables. This observation should be taken cautiously: Q^2 (resp. Q'^2) are not the same for the two reaction, and we always used a significantly larger TCS Q'^2. Our conclusion is that CFFs and particularly $\Im E$ will be extracted even for cases of large experimental uncertainties. This result can be extrapolated to other kinematics.

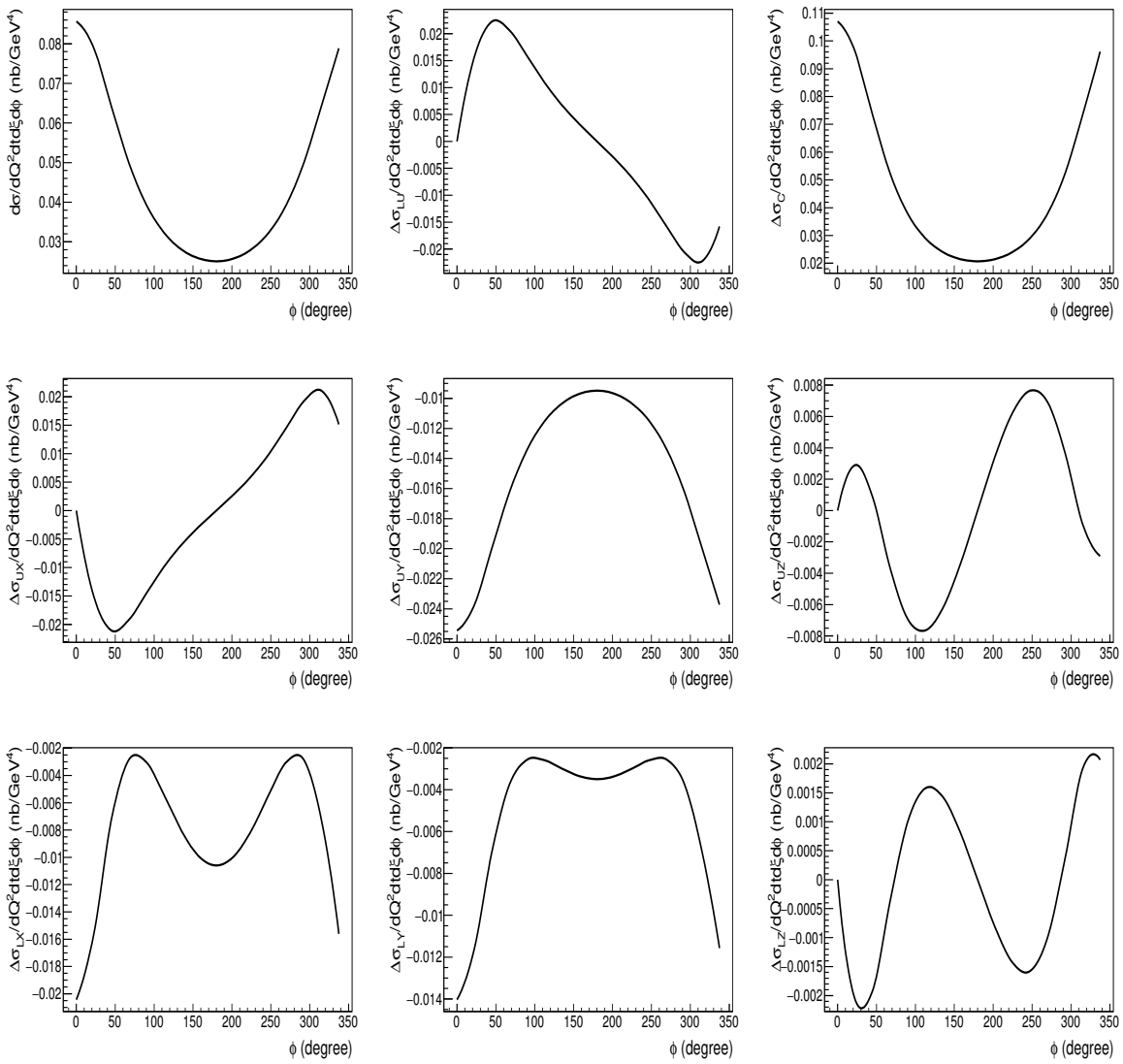

Figure 29: Generated distributions for DVCS+BH process. First row: unpolarized cross section, beam spin cross section difference, beam charge cross section difference. Second row: single target spin cross section differences (target spin along x, y, z). Third row: double spin cross section differences (target spin along x, y, z).

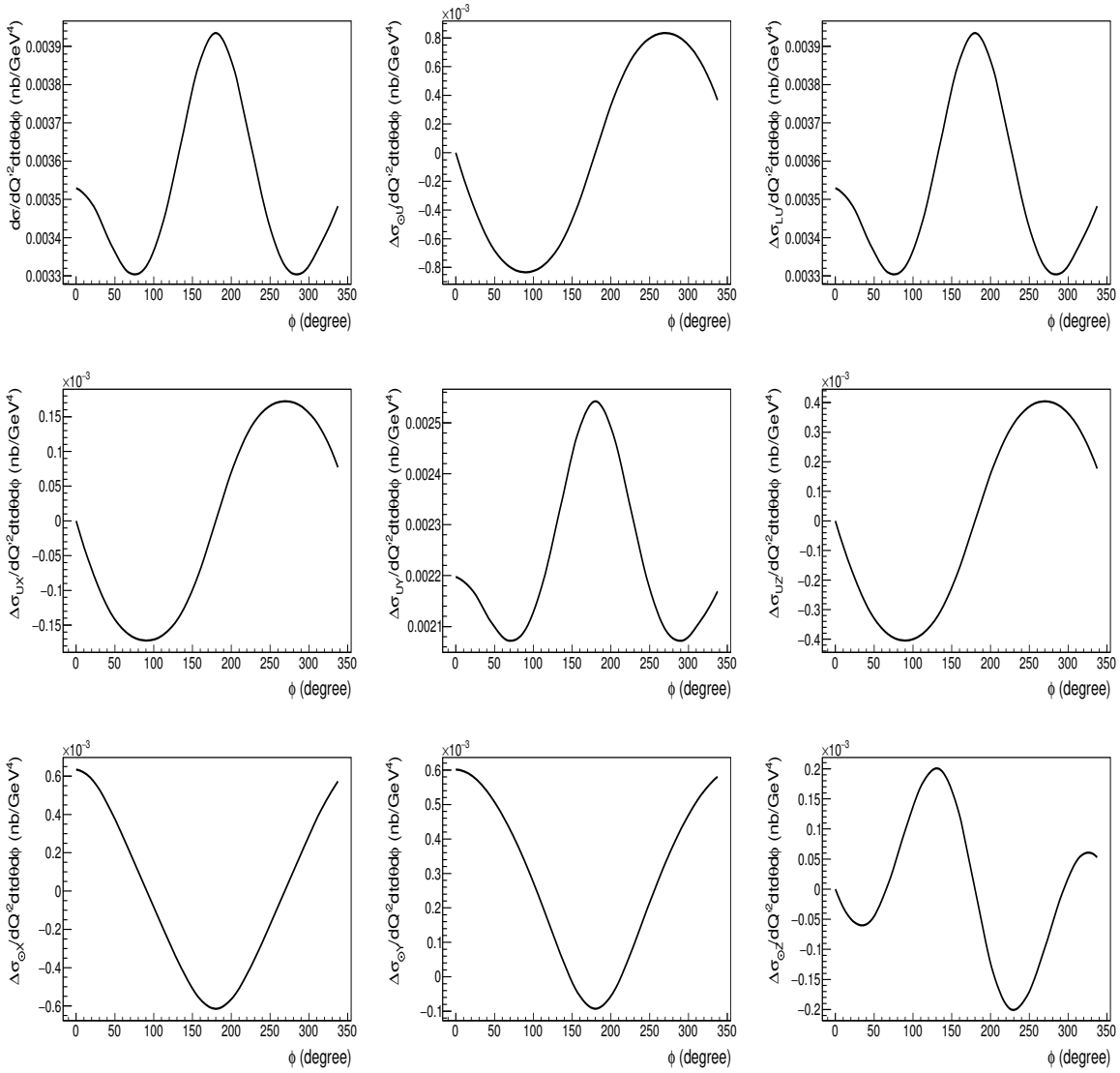

Figure 30: Generated distributions for TCS+BH process. First row: unpolarized cross section, circularly polarized beam spin cross section difference, longitudinaly polarized beam cross section difference. Second row: target polarized cross section differences (target spin along x, y, z). Third row: double beam and target polarized cross section difference (target spin along x, y, z).

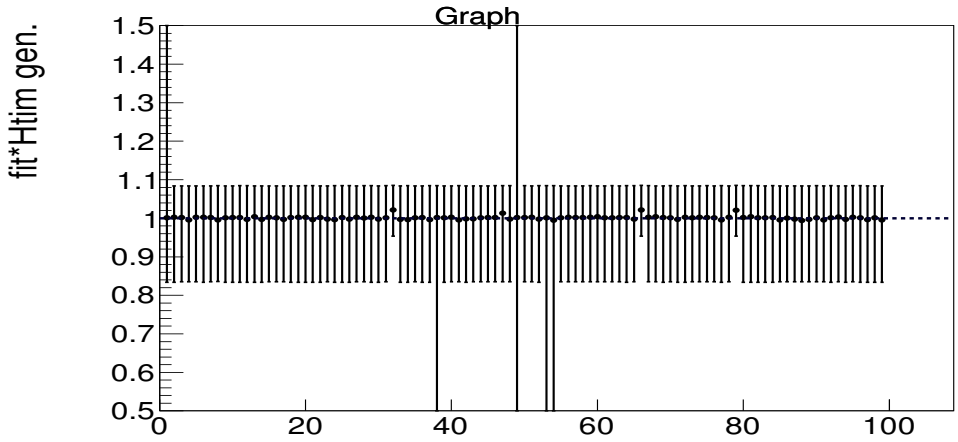

Figure 31: Result for $\Im\tilde{\mathcal{H}}$ of fitting 100 times the same distribution starting from a random value for all CFF coefficients in $[-5, +5]$. We fitted simultaneously DVCS+BH unpolarized cross section, beam spin and longitudinal target single and double polarized cross section differences. We assumed uncertainties of 5%/bin and 7%/bin for the unpolarized and polarized cross sections, respectively, for 16 bins in ϕ.

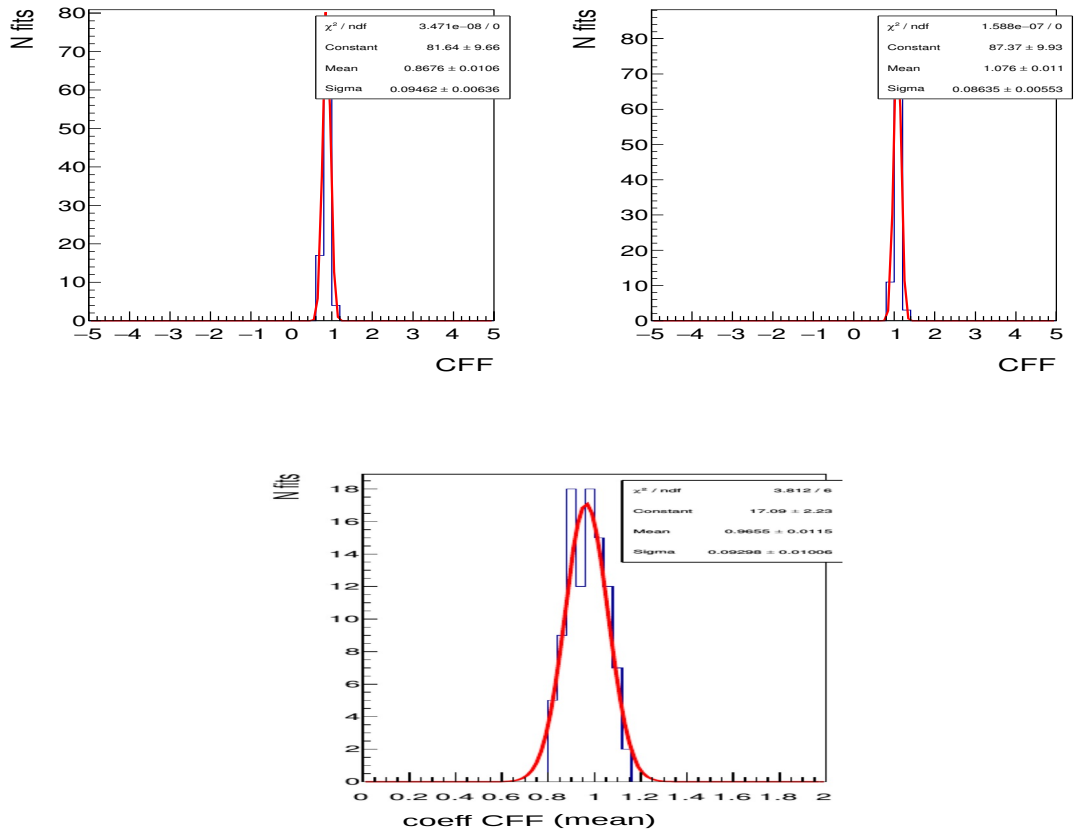

Figure 32: Top: Minimal (left) and maximal (right) limits of $\Im\tilde{\mathcal{H}}$ extracted from fitting 100 times smeared distributions of the same observables, and starting from a random value for all CFF coefficients in $[-5, +5]$. Bottom: fit result (central value) for the same distributions. Observables: DVCS+BH unpolarized cross section, beam spin and longitudinal target single and double polarized cross section differences. Uncertainties: 5%/bin for unpolarized and 7%/bin for polarized cross sections, with 16 bins in ϕ.

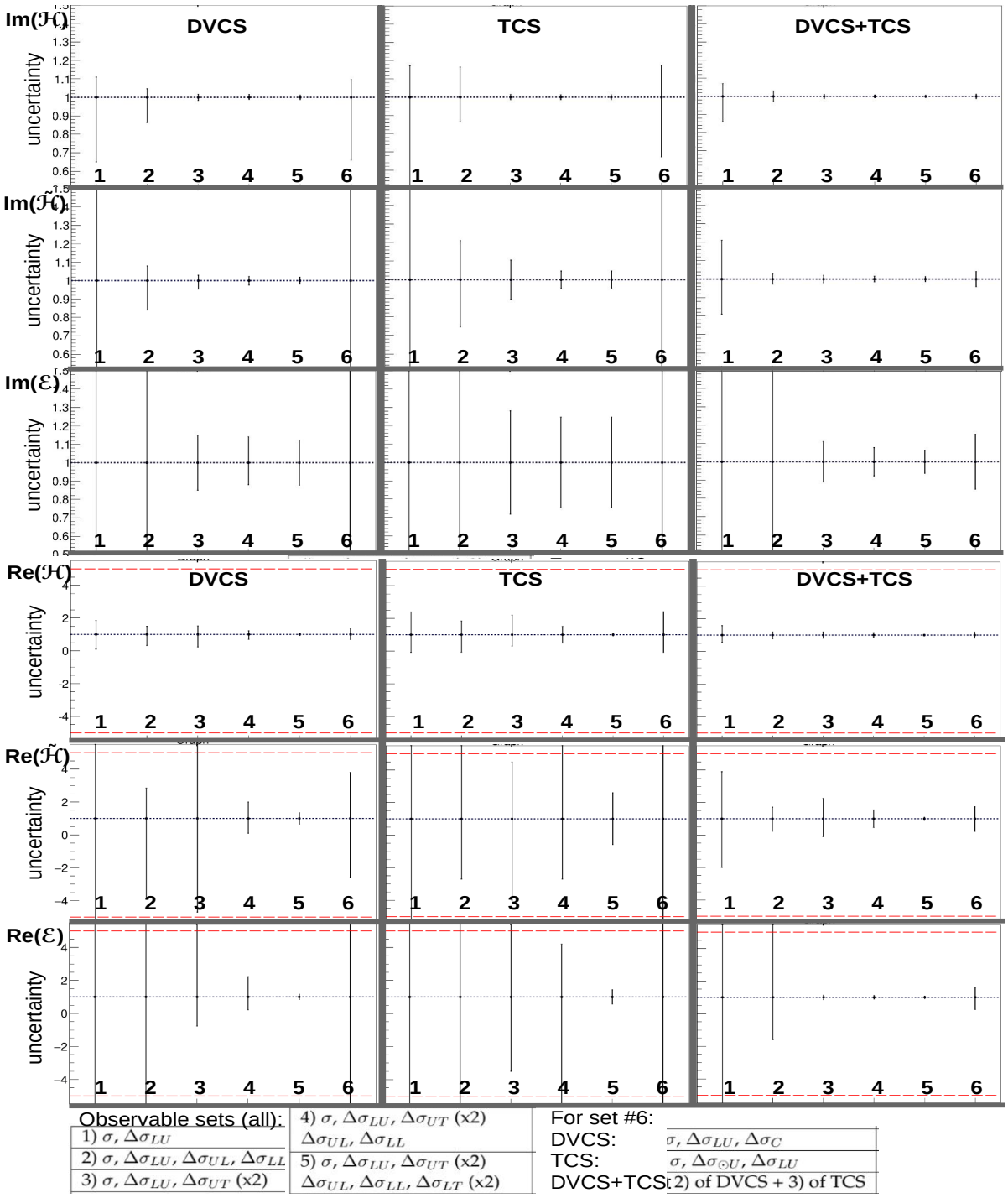

Figure 33: Uncertainties on extracted CFFs for the sets of observables Table 7 (Kinematic bin 1). Top: imaginary parts of H, $\tilde{H}$, E, Bottom: real parts of H, $\tilde{H}$, E.

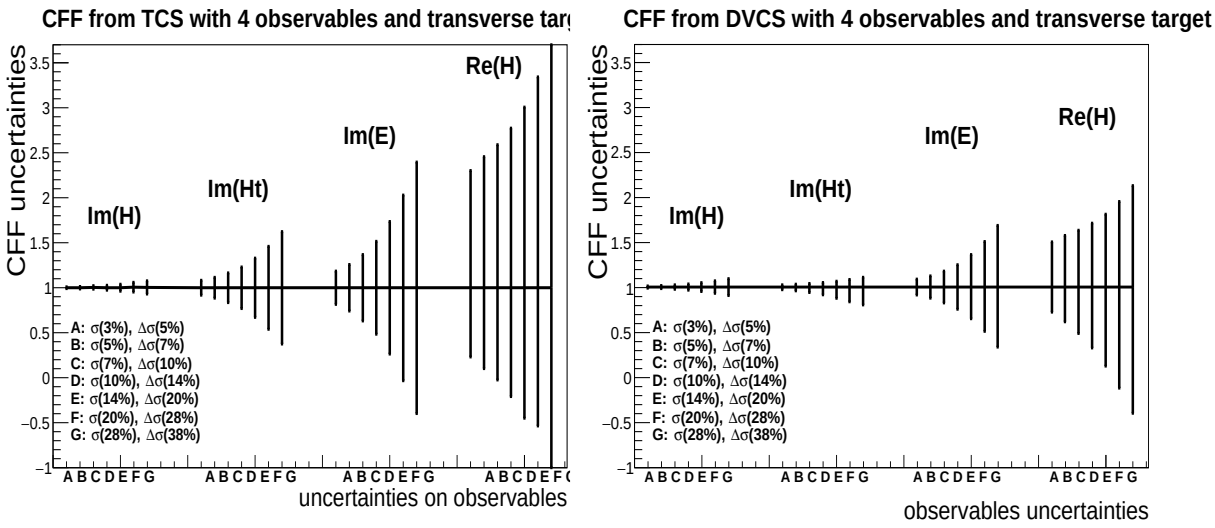

Figure 34: Uncertainties on extracted CFFs using pseudo-data for TCS (top panel) and DVCS (bottom panel), with increasing uncertainties on fitted observables. We used for the fits: σ^{unpol}, $\Delta\sigma_{LU}$, $\Delta\sigma_{Ux}$, $\Delta\sigma_{Uy}$.

C Angular correlations in BH and analysis methods

C.1 BH angular distributions

The angular dependence of the lepton pair production can be understood with the BH propagators of eq.10. In the lab frame or in the γN CM frame, if one of the leptons is emitted along the beam direction, one of the terms becomes very large. At these limits, one of the two BH diagrams is largely dominant compared to the other one. One of the leptons takes most of the energy of the virtual photon and is emitted at very low angle ($\sim 0°$), while the other one is emitted at large angle ($\sim 180°$) with a very low momentum. The cross section drastically increases next to these limits and sharp peaks are observed in angular distributions. Azimuthal distributions (ϕ) are also strongly affected by this effect: one lepton going in the beam direction forces all particles to be emitted in the same plane (see Fig. 3). The impact of this correlation between θ and ϕ is illustrated in Fig. 35, presenting distributions in ϕ, where θ has been integrated in asymmetric ranges over θ (one diagram dominates). At these kinematics, the BH peaks are at $\theta \sim 20°$ and $\theta \sim 160°$, explaining that the curve corresponding to $20° < \phi < 30°$ presents the largest cross section. In the perspective of experimental measurements, integrating calculations over a symmetric range around $\theta_{CM} = 90°$, away from BH peaks, presents the advantage of having the same contribution from the two diagrams in the integrated cross section while enhancing the statistic in each bin for displaying distributions in other variables in the data.

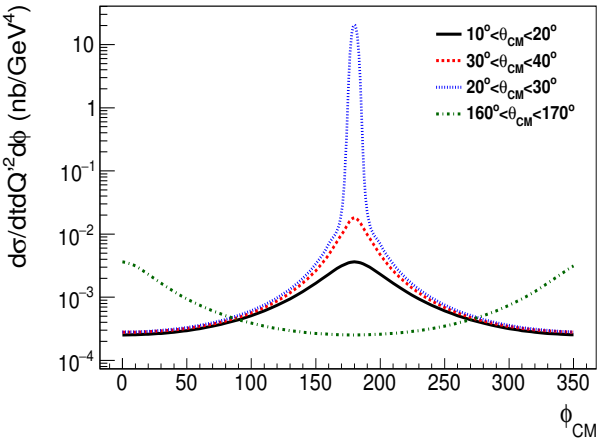

Figure 35: BH cross section as a function of ϕ at Q'^2 = 5 GeV^2, -t=0.3 GeV^2, E$_\gamma$=9.5 GeV, and integrated over θ_{CM} on various ranges (colored curves).

We expressed the cross sections as a function of the virtual photon CM frame electron angles ϕ and θ. The angle ϕ is conserved in the boost from γN C.M. frame to γ^* rest frame, while θ is not conserved. It is correlated to θ_{lab} for a given $\Theta_{\gamma\gamma^*}$ angle (the angle between incoming and outgoing photon). At $\Theta_{\gamma\gamma^*}$ larger than zero, the position of the peaks in the θ_{CM} distribution therefore de-

pends on the kinematics (E_γ, t, Q'^2). The correlation between $\Theta_{\gamma\gamma^*}$ and t at fixed E_γ and the $\Theta_{\gamma\gamma^*}$ dependence of the unpolarized cross section is displayed in Fig. 36. At small $\Theta_{\gamma\gamma^*}$ (t_{min} limit), the peaks are observed for $\theta \to 0^\circ$ and $\theta \to 180^\circ$.

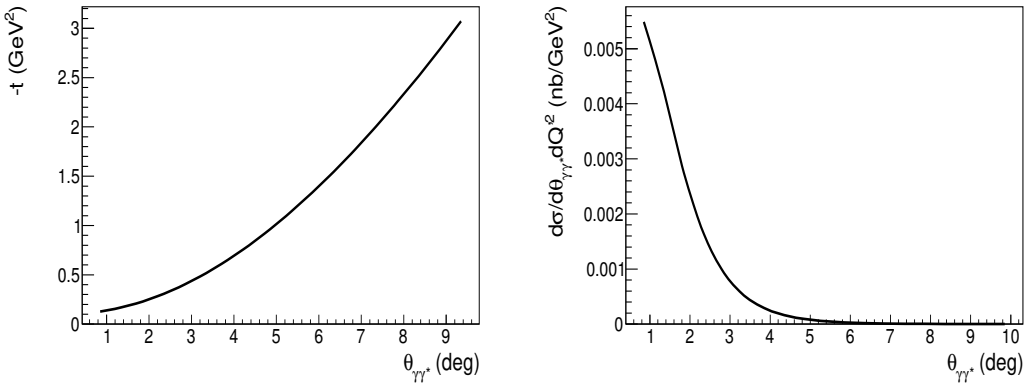

Figure 36: Distribution in -t versus $\theta_{\gamma\gamma^*}$ (left panel, at Q'^2=5 GeV^2) and BH cross section as a function of $\theta_{\gamma\gamma^*}$ (right panel, at -t=0.3 GeV^2 and Q'^2=5 GeV^2). Both curves are calculated at E_γ=9.5 GeV. for $0 < \phi_{CM} < 360^\circ$ and $45^\circ < \theta_{CM} < 135^\circ$.

C.2 Solutions for the analysis

With limited data statistics and resolution effects, measuring TCS+BH in the BH peak regions would induce very large systematic uncertainties due to the very fast variations of the cross sections. To reproduce experimental conditions (limited statistics, broad kinematic range) and obtain numerically the position of the BH peaks, we computed BH cross sections as a function of θ for several fixed values of E_γ, t and Q'^2. We integrated the cross sections over ϕ with a limited number of steps (numerical integration in Gaussian quadrature starting from the lower edge of the bin). We perfomed calculations and compared the results for two values of θ symmetric around $\theta = 90^\circ$, with 5° steps: by instance we compare the results for 85° and 95°, for 80° and 100°, etc.. The results are the same for the 2 symmetric values in θ until approching the peaks. We defined values of θ_{min} and θ_{max}, for which between these limits, the compared results have less than 5% differences. We reproduced the same exercise for different values of E_γ, t and Q'^2. Values of θ_{max} for $E_\gamma = 9.5$ GeV, as a function of $-t$ and Q'^2 are displayed on Fig. 37. We reproduced the same exercise by integrating cross sections over different ranges in ϕ_{CM} ($0\pm10^\circ$, $0 \pm 20^\circ$, $180^\circ \pm 30^\circ$, etc.). We conclude that the peaks can be avoided by 2-dimensional cuts in ϕ_{CM} and θ_{CM}, which we appy in our projections, such as:

- if (θ_{CM}<θ_{min} and $150^\circ < \phi_{CM} < 210^\circ$), the event has to be rejected,

- if (θ_{CM}>θ_{max} and $-30^\circ < \phi_{CM} < +30^\circ$, the event has to be rejected,
- otherwise the event can be kept and results can be fitted with reasonable systematic errors.

Further studies on angular correlations, impact on lepton kinematics and exclusivity can be found in [89].

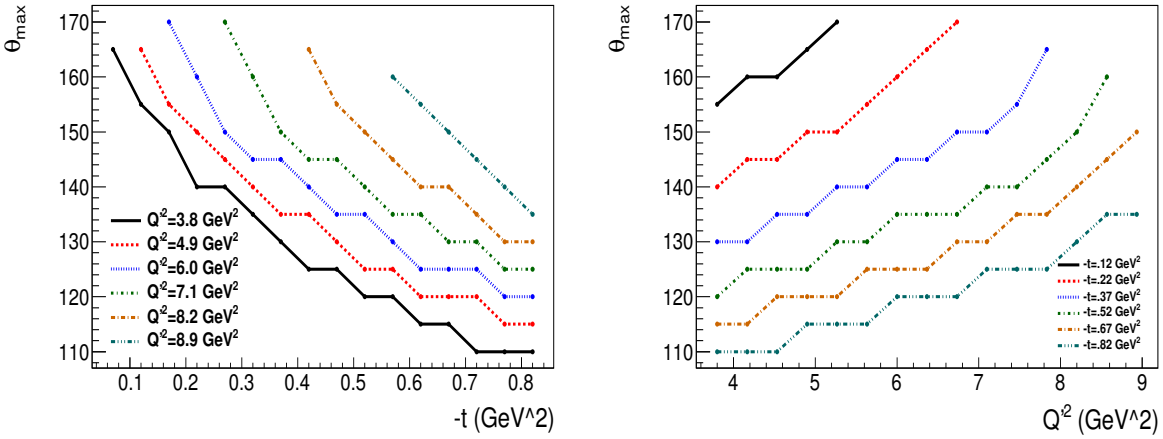

Figure 37: Values of θ_{max} for a fixed beam energy $E_\gamma = 9.5$ GeV, as a function of t for different values of Q'^2 (left panel) and as a function of Q'^2 for different values of $-t$ (right panel). See text for details.

D Analysis of Signal and Background

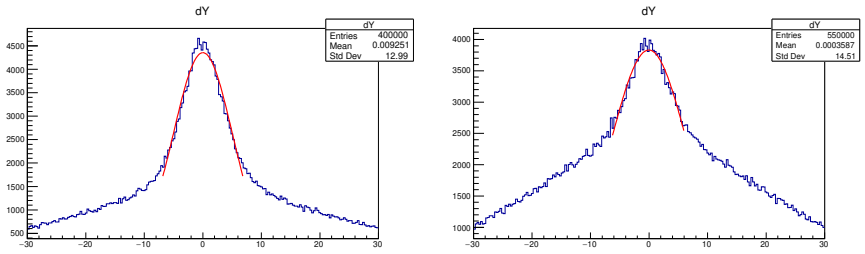

Figure 38: Distribution in δX which shows a combination of signal to background events 1:3 (left) as compared to a larger background contribution of signal to background events 1:10 (right). The fit shows a clear distinction between the signal and background events in this distribution. This demonstrates the practicality of resolving signal in the worst case scenario of ten times more background than signal.

Previous JLab experiments have shown that utilization of the two-body kinematic correlation (co-planarity) between the recoil proton and the NPS detected particles can help in improved extraction of the events of interest despite the competing background processes. In our case this is the $\gamma p \rightarrow p\pi^+\pi^-$ and $\gamma p \rightarrow p\pi^+\pi^- X$ events corresponding to the miss-identification of charged pions as the electrons from the TCS+BH decay. We first explore the list of all possible final states that could have a similar final state including different topologies that can be miss-identified in the NPS or Hodo/GEM-pack. There are many channels that contribute to the same final state but we select a Q^2 range that significantly reduces the cross section of the possible background for pe^+e^-. We also study the possible miss-identification of both the proton in the GEM-pack and the e^+ and e^- in the NPS. Our trigger, detector package and analysis process mitigates the majority of these processes. The ones with still measurable contributions are listed in Table 8. The cross section at middle Q^2 value 7 GeV^2 is indicated with the ratio of acceptance A_1 of TCS to the background in question. This is with our imposed analysis cuts but not with the additional constraints from machine learning which are listed as A_2. The estimated error to our asymmetry is also indicated under the $error$ column.

The π^+ and π^- are in multiple channels that can look very similar to our TCS (using the conservative NPS pion/e suppression ratio) so we still must carefully analyze the strength of these backgrounds that slip through.

The reconstructed energy of the recoiled particle is used which is measured with both the Hodo/GEM-pack. The NPS provide detection of the electrons/pions with energies range between 0.5-7.6 GeV with an energy resolution (1-2%), and coordinate resolution of (2-3 mm) with angular resolution of 0.5-0.75 mrad. For the GEMs the position resolution is better than on the tens of micron level. The GEMs high granularity can be configured with our FPGA trigger for high-level event selection. These combined high performance position resolution detectors help to provide the needed information to select our exclusive process.

To optimize our signal extraction we also use a δX and δY cut on the GEM position. δX

Channel	Xsec (nb)	A_1	A_2	(%) error
$pJ/\psi \to pe^+e^-$	1×10^{-4}	1	0.9	0.2%
$pX \to pe^+e^-$	1×10^{-5}	1	0.9	0.1%
$pX \to pe^+e^-\pi^0$	1×10^{-4}	0.7	0.4	0.1%
$p\psi' \to pe^+e^-$	1×10^{-6}	0.2	0.1	0.1%
$p\rho \to p\pi^+\pi^-$	1×10^{-2}	0.01	0.002	0.2%
$p\omega \to p\pi^+\pi^-$	1×10^{-5}	0.01	0.002	0.1%
$p\rho' \to p\pi^+\pi^-$	1×10^{-4}	0.01	0.002	0.1%
$pf_2 \to p\pi^+\pi^-$	1×10^{-5}	0.01	0.002	0.1%
$\gamma p \to p\pi^+\pi^-$	1×10^{-2}	0.01	0.002	0.1%
$pX \to \pi^+\pi^-$	1×10^{-5}	0.0.005	0.00	0.1%
$pX \to \pi^+\pi^-\pi^0$	1×10^{-5}	0.005	0.00	0.1%

Table 8: Here will list the dilution factor estimates based on photoproduction cross sections of the dominate background with kinematic sensitivity for four kinematic bins for pure ammonia (NH_3) as well as for the contribution from all materials (NH_3+A), as well as the total with contribution from packing fraction and target density in (Full). Errors contain contributions from both statistical and systematic uncertainty estimates.

(δY) are the different between the detected position in the GEM detector and the reconstructed position. The reconstructed position assumes a vertex from the q-vector and recoil proton as the central location in the target. There is then a co-planarity assumed between the q-vector and out going proton. The proton mass in also assumed as the target and the outgoing recoil particle. This gives us enough information to reconstruct the protons position on the first tracker layer face. All three tracker can be use to study this to improve selection but here we are using the first layer as an example.

In this same way we can study the distribution in the Mandelstam variables S, T, and U without photon beam detection. This also allows us to look at the photon beam distribution and select kinematic cuts on photon energy within our reconstructed resolution. This provides a way to study our results in photon energy bins. We can also study our data in Q^2 bins directly provided directly from the NPS.

In our case this is the $\gamma p \to p\pi^+\pi^-$ and $\gamma p \to p\pi^+\pi^- X$ events corresponding to the miss-identification of charged pions as the electrons from the TCS decay. Because of the similarity in the phase space of these processes with our TCS/BH signal contributions it is difficult make clean separate and can lead to a substantial contribution to the overall systematic uncertainty. One significant advantage of the deployment of a pure photon source is that many other channels to the background are naturally suppressed. However we are still susceptible to the photoproduction of pions with cross sections that are large relative to TCS/BH.

The NPS can suppress a significant fraction of the pion background using standard shower profile particle identification between electron and charged pions. This is estimated to be about 5×10^{-4} using basic cluster pattern discrimination combined with the particle momentum determination in order to achieve critical rejection factors. When optimized using multivariate classifi-

cation in the shower profile an additional suppression of pions is possible by more than a factor of 5. In our studies we use the conservative value listed above.

Our goal in signal extraction is to optimize our cut efficiently to reduce the amount of non-TCS background while preserving as much TCS/BH as possible. If after our standard kinematic constrains on angle, Q^2 range, and PID selection in both the NPS and GEMs we isolate our signal and the remaining contamination from the dominating background. For all kinematics that ratio of signal to background ranges from 3 to 10 as can be seen from the results of the Monte Carlo simulation in Figure 38. The final step would be to cut on δX and δY which leave a background dilution (d_π) of around 30% defines as,

$$d_\pi = \frac{N_{TCS}}{N_\pi + N_{TCS}}$$

. Both the polarized target dilution (f) and d_π we want as close to unity as possible. These factors adversely affect the statistical accuracy of our measurements. We list the resulting dilution factors in Table 9. We separate these two dilution factors because the target dilution factor is intrinsic to the target like the unwanted nitrogen and other materials in the beam-line. The background dilution is primarily due to limitations in PID and not intrinsic to the polarized target. The pions that interact with the target nitrogen or beam windows or other materials are counted in the target dilution.

Q^2-bin	$< Q^2 >$	NH_3		NH_3+A		Full
		f	d_π	f	δf (%)	$\delta f(\%)$
4.0 -5.6	4.9	0.198	0.33	0.197	0.5%	2.3%
5.6 - 7.1	6.3	0.210	0.35	0.210	0.7%	2.5%
7.1 - 8.3	7.8	0.205	0.32	0.203	0.9%	2.6%
8.3 - 9.0	8.4	0.209	0.34	0.207	1.9%	2.8%

Table 9: Here will list the dilution factor estimates based on photoproduction cross sections of the dominate background with kinematic sensitivity for four kinematic bins for pure ammonia (NH_3) as well as for the contribution from all materials (NH_3+A), as well as the total with contribution from packing fraction and target density in (Full). Errors contain contributions from both statistical and systematic uncertainty estimates.

The pion can also be produced from bound protons in nitrogen. Motion of the nucleons in nuclei, and FSI, reduce dramatically the dilution of TCS events. The nuclear pion process was investigated by using E99-114 data obtained from an aluminum target. We found that at conditions similar to those proposed here, pions produced from nuclei increase the dilution factor by less than 10

In order to optimize the final cut we use the distributions in Q^2, S, T, U, dX and dY to build a feature space for an artificial deep neural network classifier, see Fig. 39. Recent developments in machine learning have shown that these networks are capable of learning complex, non-linear relations when trained on a sufficiently large amount of training data. This is exceedingly so with $deep$ networks with several hidden layers and a large number of neurons in each layer. We employ

these techniques here only as a demonstration that the background evens in the most conservative estimates are manageable and that there are tools available to maximize our statistical significance with the requested beam time. Distribution in the feature space defined by our kinematic variables shown in Fig. 39 are used in our classification analysis. The red blue show the more narrow signal distributions which indicate the advantage of our right position resolution detector configuration. The red indicates the broader background, especially seen in the δX and δY distributions.

D.1 Deep Learning Method

The deep neural network implementation provides an optimized implementation of feed-forward multilayer perceptrons that can be efficiently trained for the classification of signa and background using deep neural networks. We use the stochastic batch gradient descend with a sigmoidal activation function, now quite common in artificial neural networks. In each training step the weights W_{ij}^k and bias terms θ_i^k of a given layer are updated using,

$$\begin{aligned} W_{i,j}^k &\to W_{i,j}^k - \alpha \frac{\partial J\left(\mathbf{x}_b, \mathbf{y}_b\right)}{\partial W_{i,j}^k} \\ \theta_i^k &\to \theta_i^k - \alpha \frac{\partial J\left(\mathbf{x}_b, \mathbf{y}_b\right)}{\partial \theta_i^k}. \end{aligned} \tag{14}$$

In this iteration $J\left(\mathbf{x}_b, \mathbf{y}_b\right)$ is the loss function corresponding to the randomly chosen input batch $\mathbf{x}_b$ and expected output $\mathbf{y}_b$. Loss can be impose by the weight terms W^{ij} at each layer. The training of the deep neural network is performed in one or multiple training phases. A training phase ends when the test error did not decrease for a user-specified number of epochs. We generate the background and signal channel imposing the appropriate resolutions from detector/reconstruction.

The training batch is randomly selected and without replacement from the set of training samples. The training of the deep neural network is performed over multiple training phases. A training phase ends when the test error did not decrease for 10 epochs assuming a natural descending trend.

A validation data set is used to determine the bounds of over-training. This is also a standard technique which requires sampling over the data set randomly to select non-biased Monte Carlo that can be compared to the evaluation set. The training set and a sub-training set are used to compute the gradient and update the weights while the validation set is used to compute the error and to check for convergence.

In order to study the quality of our input variable we look at the correlation matrix for our feature space (Fig. 40 (left)) which show that the only strong correlation is between S and U otherwise all these variable are contributing significantly to the classification. The classification response is shown (right) indicating that the background can significantly be reduced with a cut in the response. These resulting distributions of background and signal with an event by event response weight allows a cut based on the classification analysis of the deep neural net. Further analysis provides the optimal cut along the response.

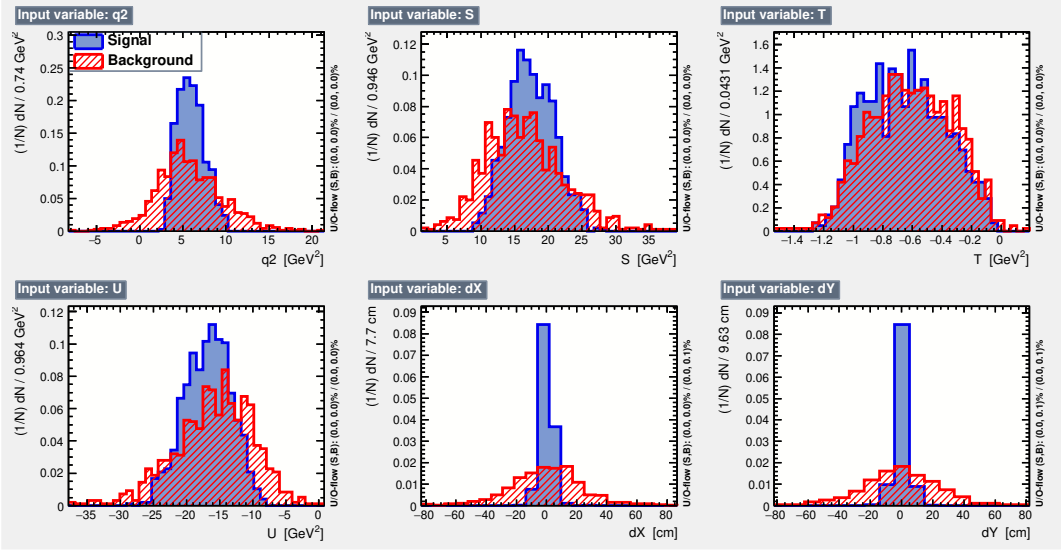

Figure 39: Distributions in Q^2, S, T, U, dX and dY used build a feature space for a artificial deep neural network classifier. The blue signal distributions generally shows more narrow distributions which indicate the advantage of the position resolution of our detector configuration. The red distributions indicates the broader background, especially seen in the δX and δY distributions. These distributions are shown before detector acceptance cuts for simplicity.

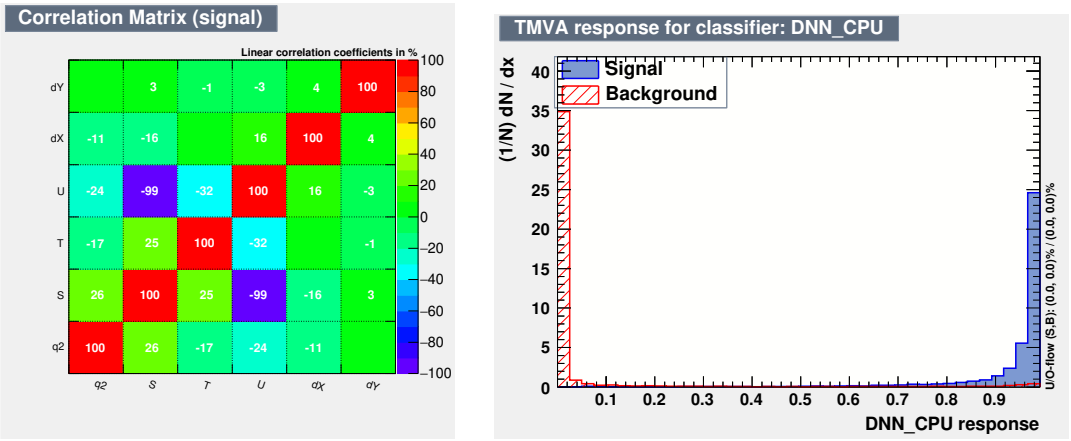

Figure 40: The correlation matrix for our feature space (left) which show that the only strong correlation is between S and U otherwise all these variable are contributing significantly to the classification. The classification response is shown (right) indicating that the background can significantly be reduced with a cut in the response.

The cut efficiencies and optimal cut value from the DNN classification analysis can be calculated with the resulting DNN response information. The signal and background efficiency as well as the signal purity and purity time efficiency are along with the statistical significance shown in green are all shown in Fig. 41. These efficiencies have a dependence on the amount of signal to background present. Here we are showing the example of equal amounts of signal to background. The results indicate that a cut 0.29 will maximize the statistical significance.

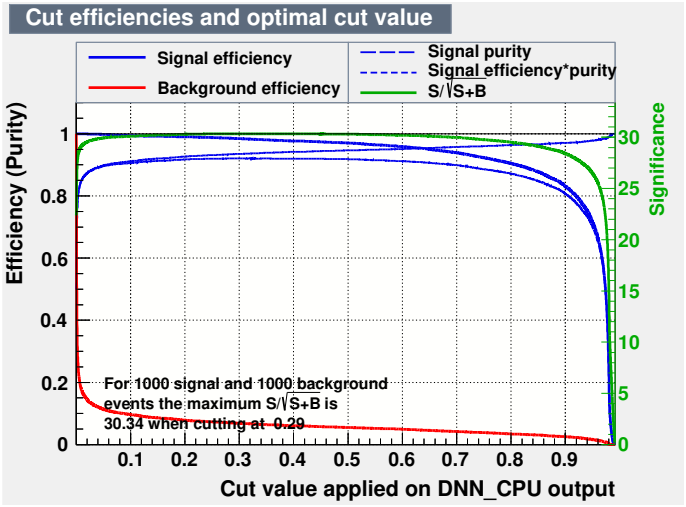

Figure 41: The cut efficiencies and optimal cut value from the DNN classification analysis. The signal and background efficiency as well as the signal purity and purity time efficiency are all shown with the statistical significance shown in green.

After we preform this analysis with cut optimization for the ratio of signal and background on the same set of bin we improve our experimental dilution factors as shown in Table 10. This same DNN optimized cut is used to produce the final acceptance ratio A_s listed in Table 8.

Q^2-bin	$< Q^2 >$	NH_3		NH_3+A		Full
		f	d_π	f	δf (%)	δf(%)
4.0 -5.6	4.9	0.200	0.66	0.196	0.5%	2.3%
5.6 - 7.1	6.3	0.211	0.73	0.210	0.7%	2.5%
7.1 - 8.3	7.8	0.208	0.75	0.203	0.9%	2.6%
8.3 - 9.0	8.4	0.211	0.68	0.208	1.9%	2.8%

Table 10: Here will list the dilution factor estimates after our DNN analysis based on photoproduction cross sections of the dominate background with kinematic sensitivity for four kinematic bins for pure ammonia (NH_3) as well as for the contribution from all materials (NH_3+A), as well as the total with contribution from packing fraction and target density in (Full). Errors contain contributions from both statistical and systematic uncertainty estimates.

After the cut DNN efficiency has been optimized the dilution factor is reevaluated again. Table 10 will list these new dilution factor estimates with kinematic sensitivity for four kinematic bins for pure ammonia (NH_3) as well as for the contribution from all materials (NH_3+A), as well as the total

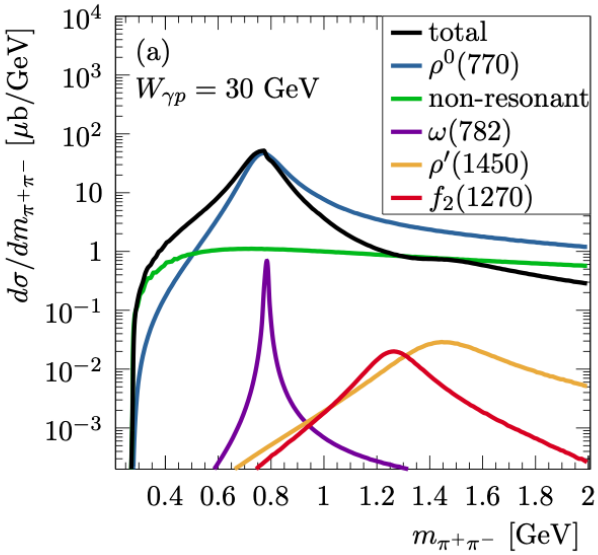

Figure 42: Differential cross sections $d\sigma/dm_{\pi^+\pi^-}(\gamma p \to \pi^+\pi^- p)$ as function of $m_{\pi^+\pi^-}$ for fixed $W_{\gamma p} = 30$ GeV and integrated over the range -1 GeV$^2 \leq t \leq 0$. The full model, non-resonant contributions and the contributions from the resonances $\rho(770)$, $\omega(782)$, $\rho(1450)$ and $f_2(1270)$ are shown.

with contribution from packing fraction and target density in (Full). Errors contain contributions from both statistical and systematic uncertainty estimates.

D.2 Background contributions

D.2.1 Pion background

Even after pion suppression from the NPS we still must contend with the charged pion background. To estimate the contribution to our background from $\gamma p \to \pi^+\pi^- p$ we produce at generator containing the necessary physics and kinematics overlapping with TCS. We encoded the cross sections and angular distributions from [97] for the numerical evaluation. In the model used in this work many of the parameters are well constrained for the kinematics up to $Q^2 < 4$ so an extrapolation is made for our kinematics of interest $Q^2 = 4 - 9$ GeV^2. The calculation is based on a model of high energy scattering with the exchanges of photon, pomeron, odderon and reggeons. The pomeron and the $C = +1$ reggeons are described as effective tensor exchanges, the odderon and the C = -1 reggeons as effective vector exchanges. Also used is a gauge-invariant version of the Drell-Soding mechanism which produces the skewing of the ρ-meson shape. Starting from the explicit formulae for the matrix element for dipion production an event generator was developed which comprises all contributions mentioned above and includes all interference terms. There is details information on the total and differential cross sections and a well as interference of $C = +1$ and $C = -1$ exchange contributions. In the model used many of the parameters are well constrained for the kinematics up to $Q^2 < 4$ so an extrapolation is made for our kinematics of interest $Q^2 = 4 - 9$ GeV^2 under the parameterization using $-t < 1$ GeV^2 and $W_{\gamma p} = 3.3 - 4.6$ GeV. In the extrapolation we do not make any attempt to fit the parameters to data but for region of large

uncertainty the more conservative cross section values provided by the experimental data of the ρ photoproduction are used [98]. This is likely an over estimate of the background for some of our kinematics. In general the magnitude and qualitative features of the full set of reactions are preserved in the generator. The dominating contributions are from the $\rho(770)$, $\omega(782)$, and non-resonance channel, and then lesser so by $\rho(1450)$ and $f_2(1270)$. We attempt to do a complete study of all $\gamma p \to \pi^+\pi^- p$ channels and overlapping $\gamma p \to \pi^+\pi^- X$, where X maybe a $K+$ or something else miss identified as a proton. There are near negligible contributions from excited state from K^* and excited state baryons that have necessary charged pions in their final state. There are also less than significant contributions from charm mesons decays.

Figure 42 shows the differential cross sections $d\sigma/dm_{\pi^+\pi^-}(\gamma p \to \pi^+\pi^- p)$ as a function of $m_{\pi^+\pi^-}$ for fixed $W_{\gamma p} = 30$ GeV and integrated over the range $-1 \leq t \leq 0$ GeV^2. The full model, non-resonant contributions and the contributions from the resonances $\rho(770)$, $\omega(782)$, $\rho(1450)$ and $f_2(1270)$ are shown. Note that most cross section go down slightly for our kinematic range of $W_{\gamma p} = 3.3 - 4.6$ GeV except for the ρ. However even the ρ tappers out for increasing Q^2 when TCS is more relevant. See discussion on dilution factor for the final background contributions after all kinematic constraints.

E Projections for all kinematic bins

E.1 Transverse target spin asymmetries in 8 ϕ_S bins for 7 kinematic bins

Fig. 43 to 49 present the transverse target spin asymmetries as a function of ϕ and ϕ_S for different kinematic bins. For all these figures, we took account the acceptance of the setup (section 4.4. We applied the analysis, acceptance and phase-space cuts as described in section **??**. For each figure sub-panel, the statistic uncertainties are represented and correspond to an integrated luminosity of $5.85 * 10e5$ pb^{-1} for photons such as $5.5 < E_\gamma < 11$ GeV. Our observations and interpretations are based on the results for $-t > 0.2$ GeV^2 only, as for lower -t we may be biased by the magnetic field effects and smaller acceptance. Each figure contain 8 panels, corresponding to respectively bins in $0 < \phi_S < \pi/8$, $\pi/8 < \phi_S < \pi/4$, $\pi/4 < \phi_S < 3\pi/8$, $3\pi/8 < \phi_S < \pi/2$, $5\pi/8 < \phi_S < 3\pi/4$,$3\pi/4 < \phi_S < 7\pi/8$, $7\pi/8 < \phi_S < \pi$.

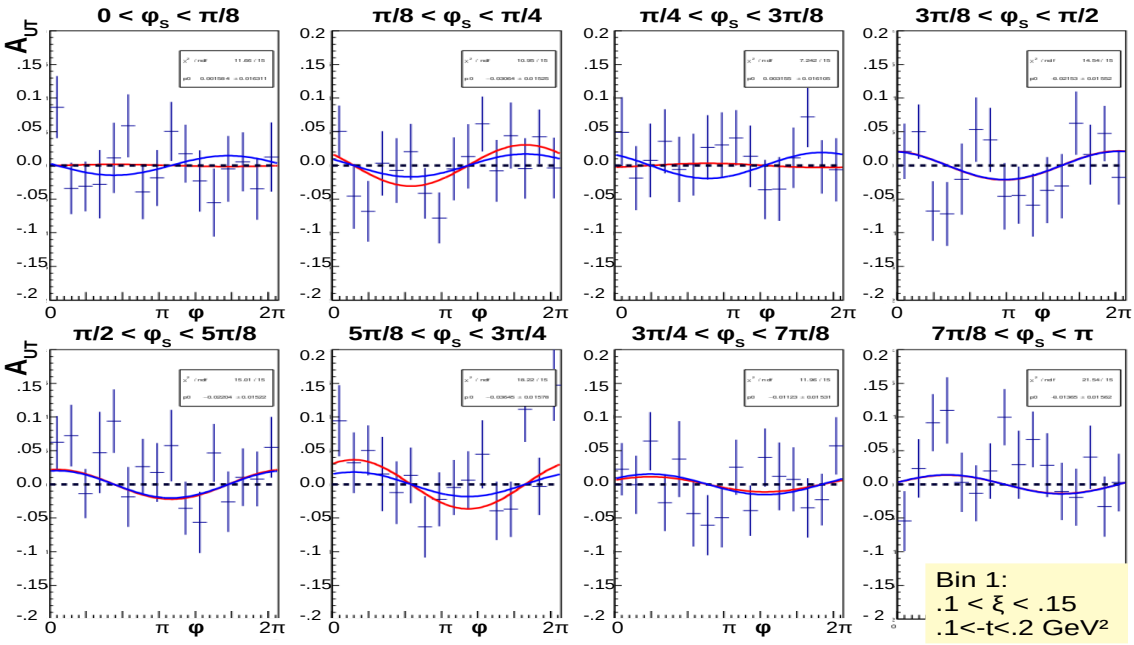

Figure 43: A_{UT} versus ϕ (16 bins) for 8 bins in ϕ_S (8 panels). Uncertainties account statistics and target polarization and dilution. Kinematic 1: $0.1 < \xi < 0.15$ and $0.1 < -t < 0.2$ GeV^2.

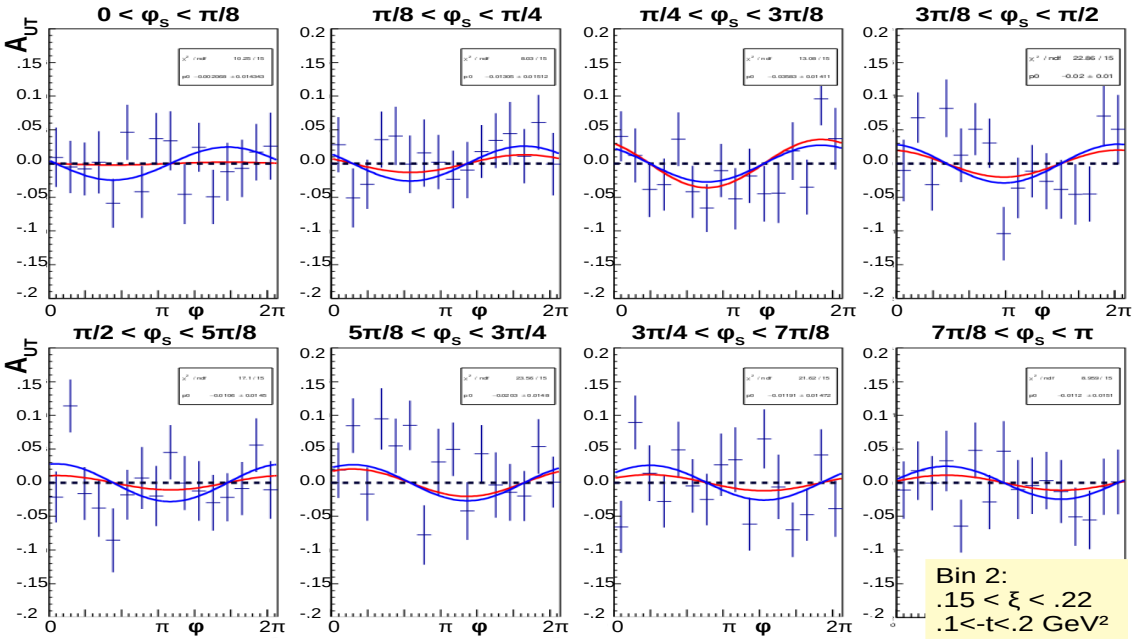

Figure 44: A_{UT} versus ϕ (16 bins) for 8 bins in ϕ_S (8 panels). Uncertainties account statistics and target polarization and dilution. Kinematic 2: $0.15 < \xi < 0.22$ and $0.1 < -t < 0.2$ GeV^2.

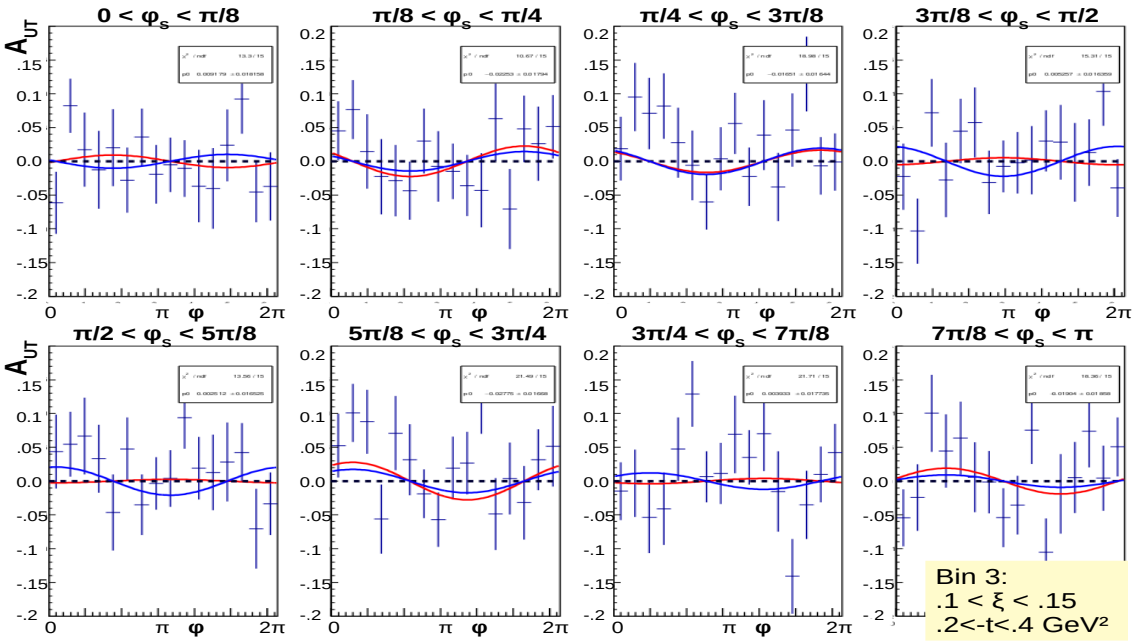

Figure 45: A_{UT} versus ϕ (16 bins) for 8 bins in ϕ_S (8 panels). Uncertainties account statistics and target polarization and dilution. Kinematic 3: $0.1 < \xi < 0.15$ and $0.2 < -t < 0.4$ GeV^2.

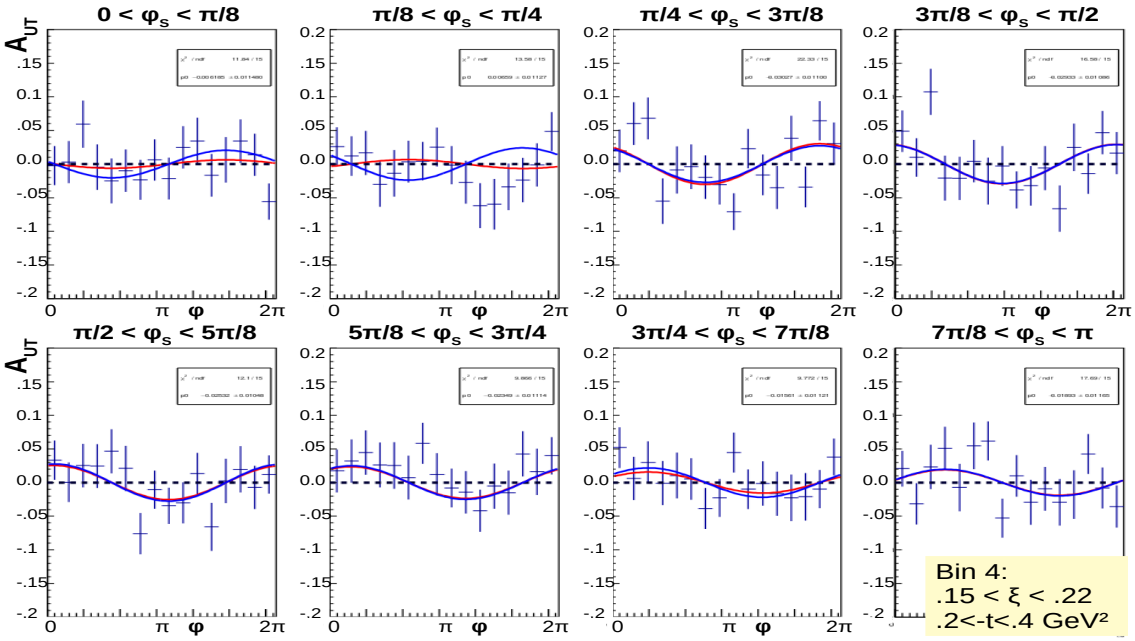

Figure 46: A_{UT} versus ϕ (16 bins) for 8 bins in ϕ_S (8 panels). Uncertainties account statistics and target polarization and dilution. Kinematic 4: $0.15 < \xi < 0.22$ and $0.2 < -t < 0.4\,\mathrm{GeV}^2$.

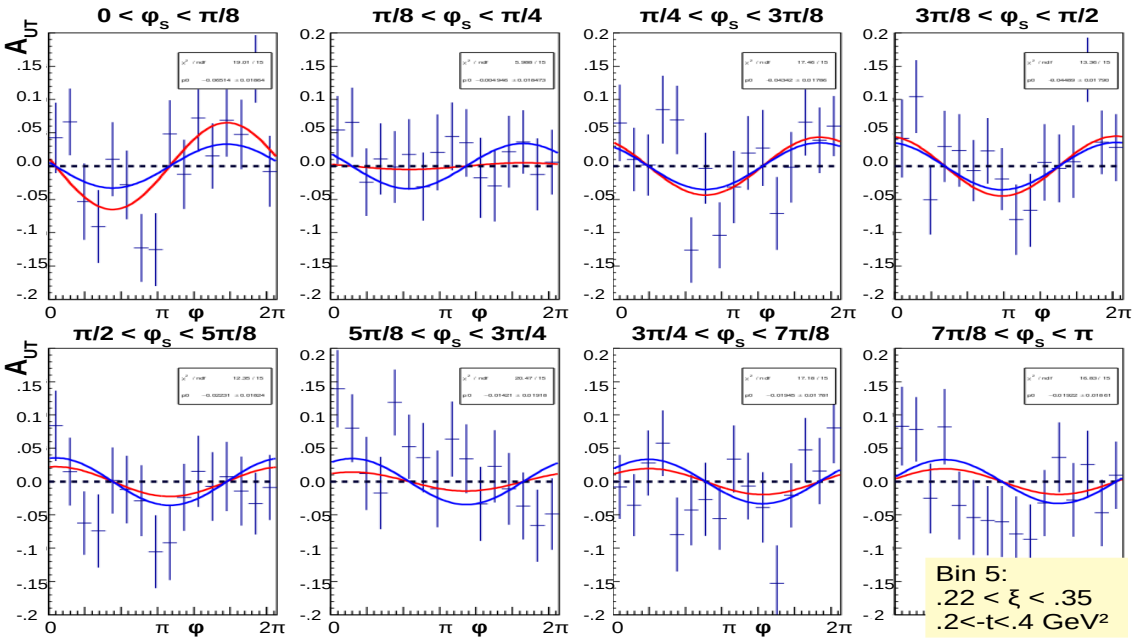

Figure 47: A_{UT} versus ϕ (16 bins) for 8 bins in ϕ_S (8 panels). Uncertainties account statistics and target polarization and dilution. Kinematic 5: $0.22 < \xi < 0.35$ and $0.2 < -t < 0.4\,\mathrm{GeV}^2$.

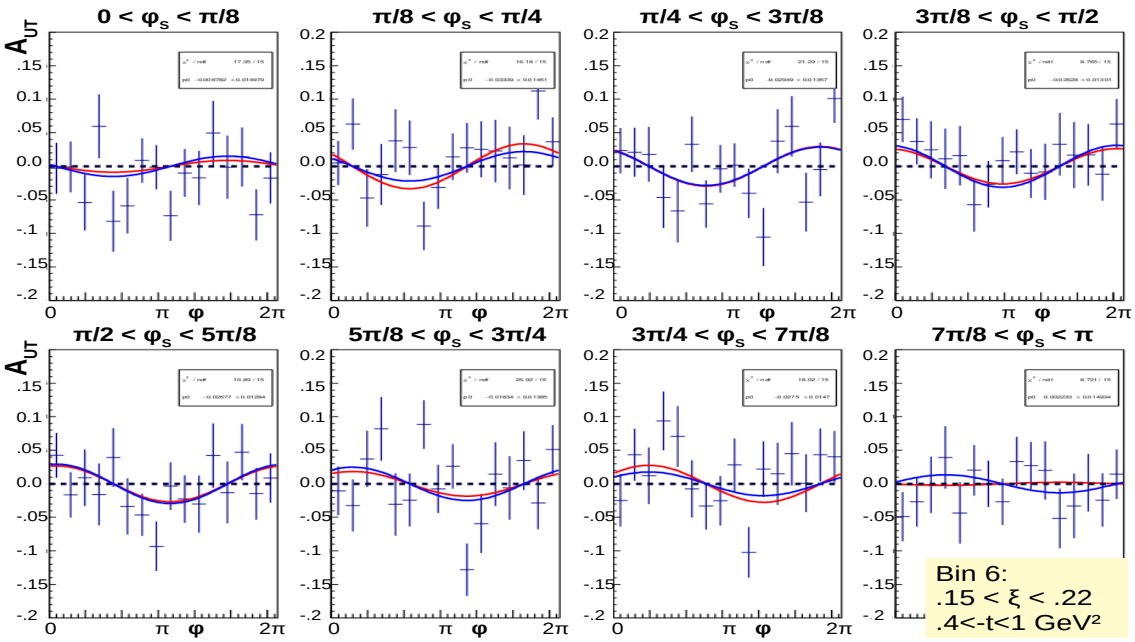

Figure 48: A_{UT} versus ϕ (16 bins) for 8 bins in ϕ_S (8 panels). Uncertainties account statistics and target polarization and dilution. Kinematic 6: $0.15 < \xi < 0.22$ and $0.4 < -t < 1$ GeV^2.

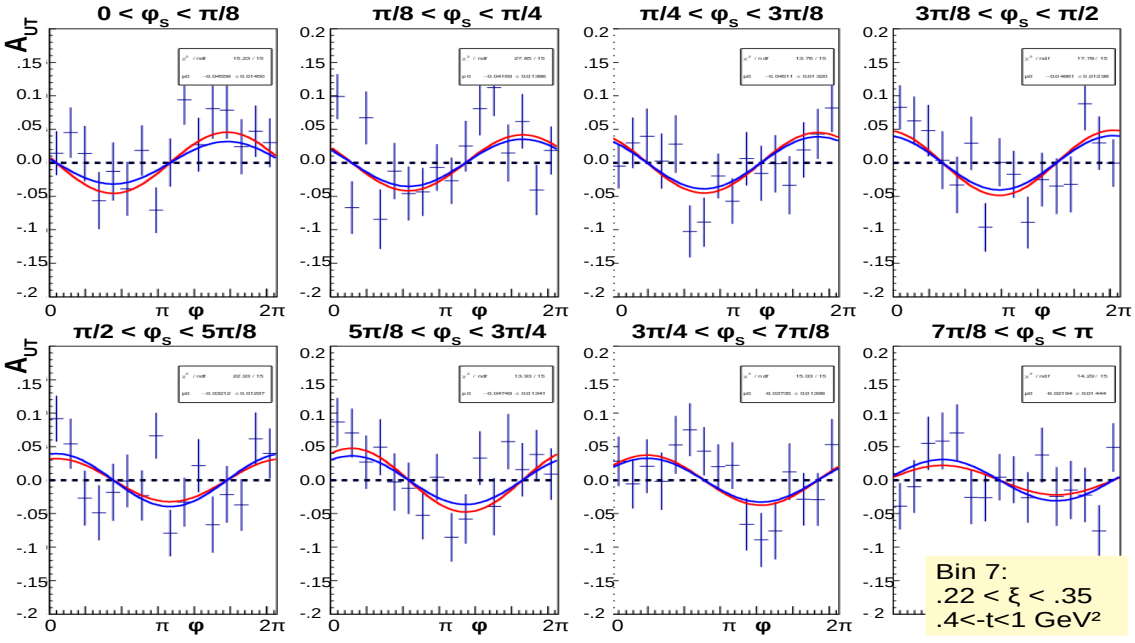

Figure 49: A_{UT} versus ϕ (16 bins) for 8 bins in ϕ_S (8 panels). Uncertainties account statistics and target polarization and dilution. Kinematic 7: $0.22 < \xi < 0.35$ and $0.4 < -t < 1$ GeV^2.

E.2 Figures of merit for the target spin asymmetry in 8 ϕ_S bins and for 8 kinematic bins

We defined the figures of merit for the asymmetries as

$$F.O.M. = N * A^2, \tag{15}$$

where N is the number of events including the acceptance and analysis cuts, and A^2 the size of the asymmetry. We neglect the background contribution and polarization transfer factor in this definition. FOM are displayed Figs. 50 to 56, corresponding to 7 kinematic bins (7 figures). Each figure contain 8 panels, corresponding to respectively bins in $0 < \phi_S < \pi/8$, $\pi/8 < \phi_S < \pi/4$, $\pi/4 < \phi_S < 3\pi/8$, $3\pi/8 < \phi_S < \pi/2$, $5\pi/8 < \phi_S < 3\pi/4$,$3\pi/4 < \phi_S < 7\pi/8$, $7\pi/8 < \phi_S < \pi$.

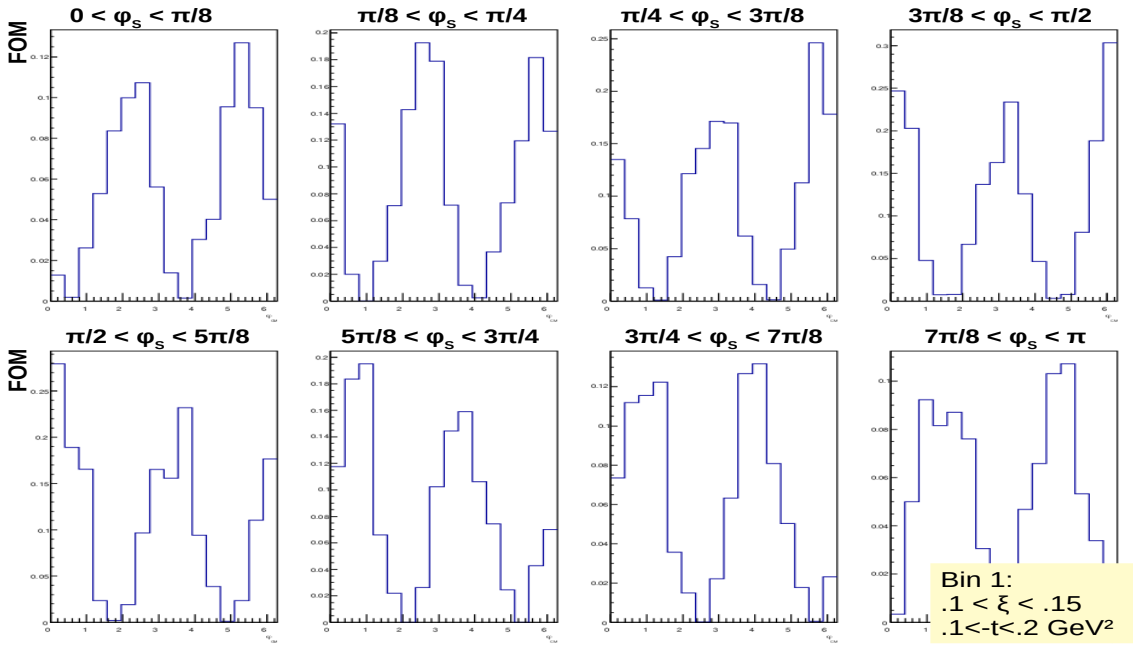

Figure 50: Figures of merit for the single transversely polarized target spin asymmetries in bins of ϕ_S (different panels), as a function of 16 bins in ϕ and for $0.1 < \xi < 0.15$ and $.1 < -t < 0.2$ GeV^2.

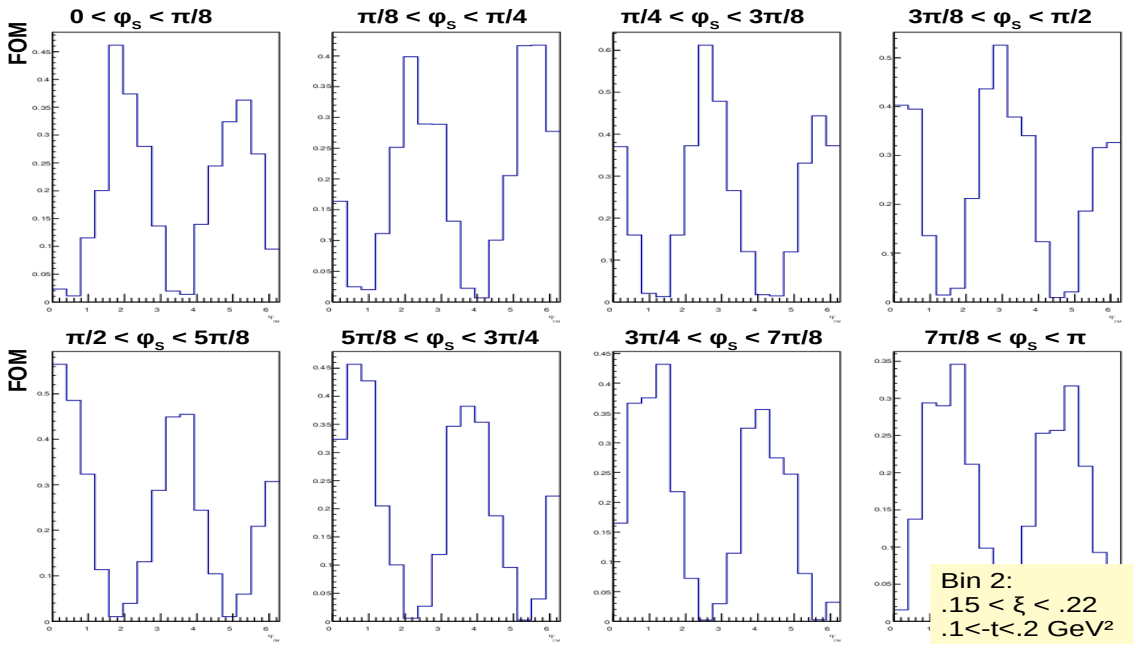

Figure 51: Figures of merit for the single transversely polarized target spin asymmetries in bins of ϕ_S (different panels), as a function of 16 bins in ϕ and for $0.15 < \xi < 0.22$ and $.1 < -t < 0.2$ GeV^2.

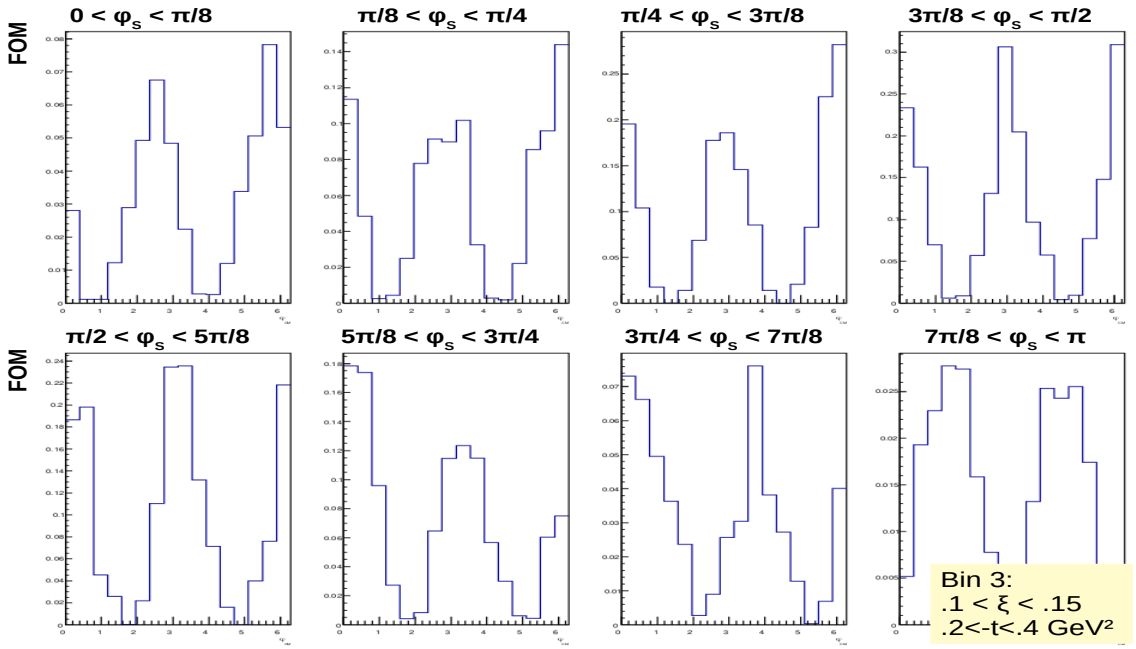

Figure 52: Figures of merit for the single transversely polarized target spin asymmetries in bins of ϕ_S (different panels), as a function of 16 bins in ϕ and for $0.1 < \xi < 0.15$ and $0.2 < -t < 0.4 GeV^2$.

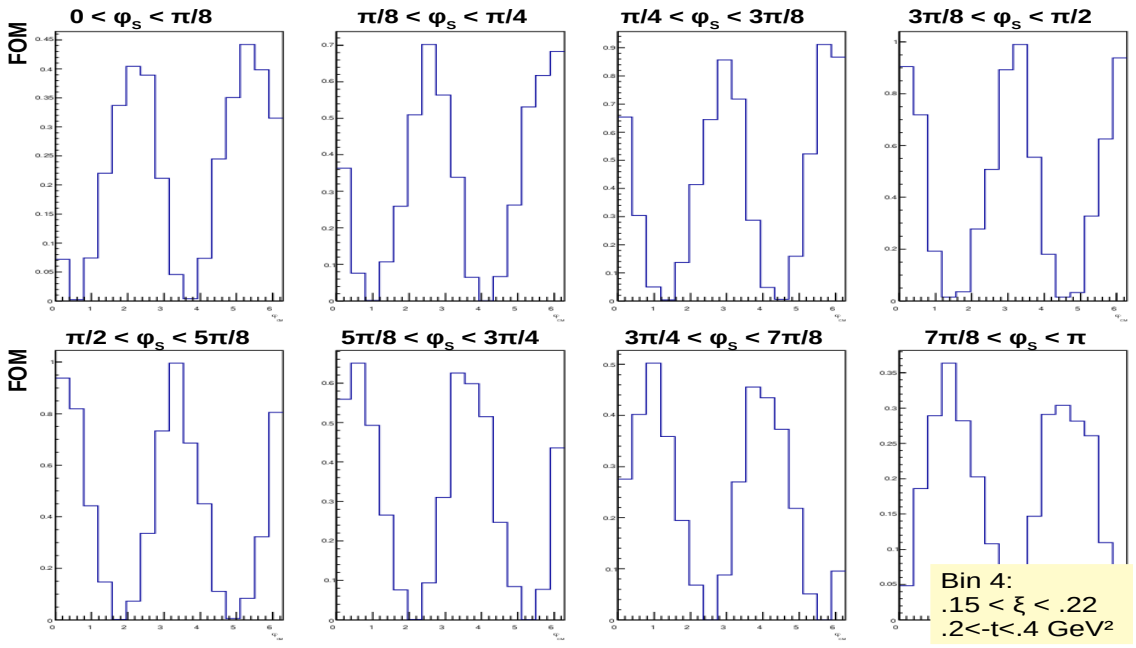

Figure 53: Figures of merit for the single transversely polarized target spin asymmetries in bins of ϕ_S (different panels), as a function of 16 bins in ϕ and for $0.15 < \xi < 0.22$ and $0.2 < -t < 0.4 GeV^2$.

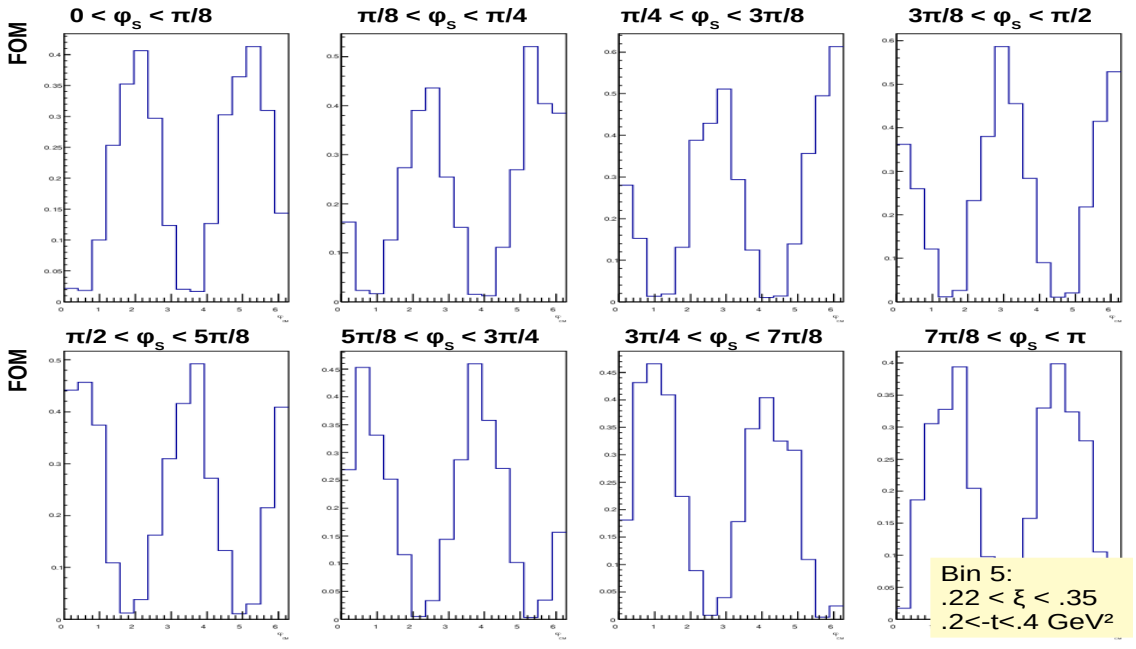

Figure 54: Figures of merit for the single transversely polarized target spin asymmetries in bins of ϕ_S (different panels), as a function of 16 bins in ϕ and for $0.22 < \xi < 0.3$ and $0.2 < -t < 0.4 GeV^2$.

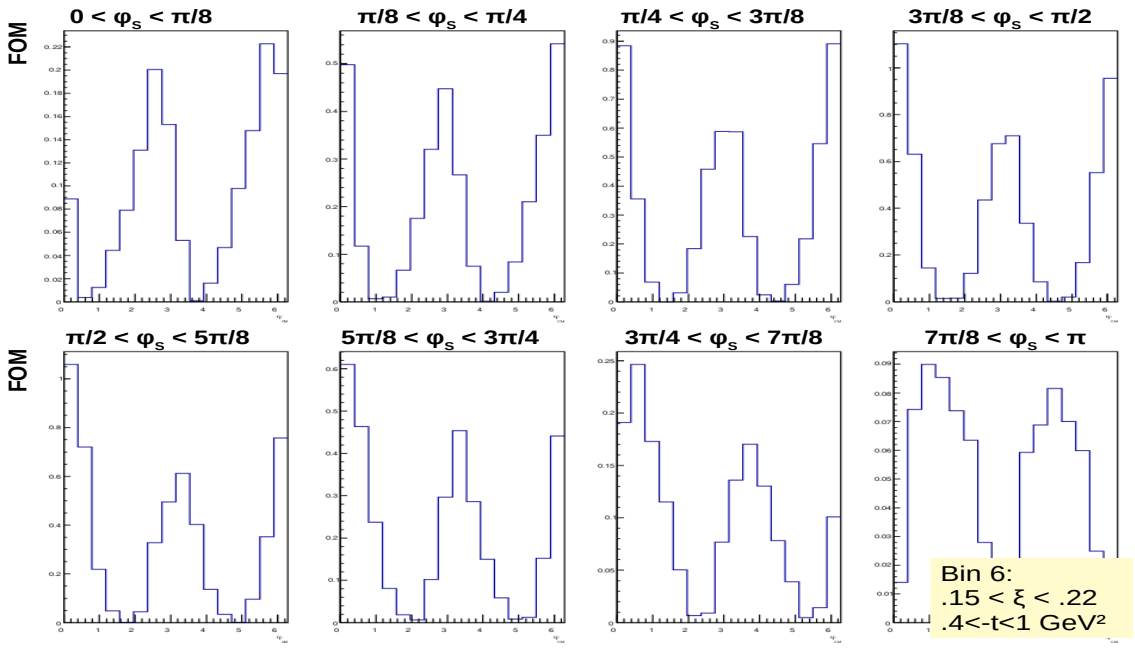

Figure 55: Figures of merit for the single transversely polarized target spin asymmetries in bins of ϕ_S (different panels), as a function of 16 bins in ϕ and for $0.15 < \xi < 0.22$ and $0.4 < -t < 1$ GeV^2.

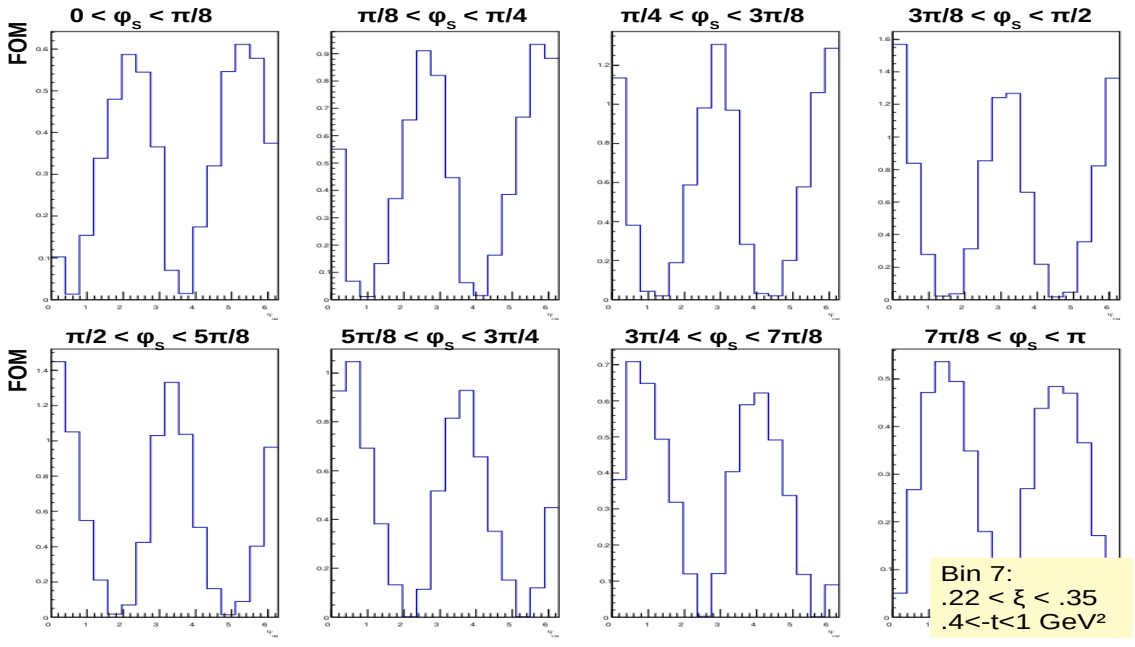

Figure 56: Figures of merit for the single transversely polarized target spin asymmetries in bins of ϕ_S (different panels), as a function of 16 bins in ϕ and for $0.22 < \xi < 0.3$ and $0.4 < -t < 1$ GeV^2.

E.3 Combined statistic uncertainties on $sin(\phi - \phi_S)$ moments

Even thought our goal is to extract the CFFs from direct fits rather than measuring moments, we can get an estimate of our expected uncertainties by looking at the projected uncertainties on the dominant $sin(\phi - \phi_S)$ moments. We can relate these projections to the uncertainties on CFFs as discussed in section 3.2. Since there are only two independent target spin asymmetries and we will fit simultaneously orthogonal bins, we can do a ''naive" error estimate by combining the non-orthogonal bins. We define $\delta A_{//}/A_{//}$ as the combination of relative errors for distributions with $\phi_S < 90°$, and similarly $\delta A_{\perp}/A_{\perp}$ with $\phi_S > 90°$. We display Fig 57 the relative uncertainties for each of our kinematic bins (x-axis), with 2 points for each bins, corresponding to $\delta A_{//}/A_{//}$ and $\delta A_{\perp}/A_{\perp}$, respectively.

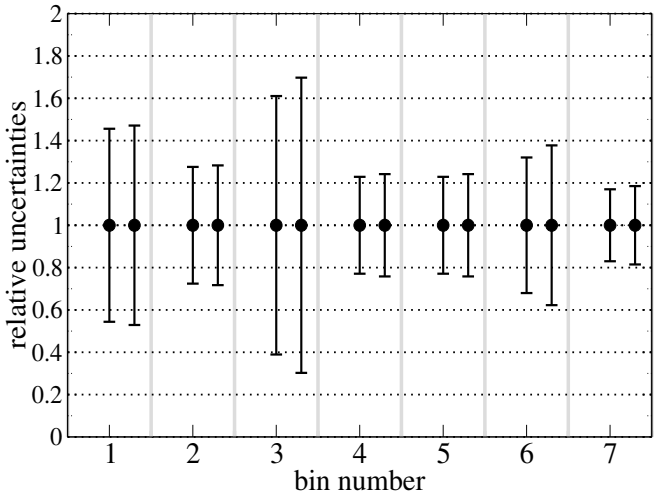

Figure 57: Relative uncertainties (y-axis) as defined in the text on the combined $sin(\phi - \phi_S)$ moments. For each kinematic bin (x-axis), 2 points are displayed, corresponding to $\delta A_{//}/A_{//}$ and $\delta A_{\perp}/A_{\perp}$, respectively.

References

[1] Z. Zhao, M. Boër, P. Nadel-Turonski, J. Zhang, JLab experiment E12-12-006A: Timelike Compton Scattering on the proton in e^+e^- with SoLID at 11 GeV, run group proposal to the PAC 43 (2015).

[2] P. Nadel-Turonski, M. Guidal, T. Horn, R. Paremuzyan, S. Stepanyan, JLab experiment E12-12-001: Timelike Compton Scattering and J/ψ photoproduction on the proton in e^+e^- pair production with CLAS12 at 11 GeV.

[3] L. Elouadrhiri, H. Avakian, V. Burkert, M. Guidal, M. Lowry, L. Pappalardo, and S. Procureur, JLab experiment E-12-12-010, conditionally approved.

[4] X. D. Ji, Phys. Rev. D **55** (1997) 7114

[5] D. Müller, D. Robaschik, B. Geyer, F.-M. Dittes and J. Hořejši, Fortsch. Phys. **42** (1994) 101

[6] A. V. Radyushkin, Phys. Rev. D **56** (1997) 5524

[7] Goeke K, Polyakov M V and Vanderhaeghen M 2001 *Prog. Part. Nucl. Phys.* **47** 401

[8] M. Diehl, Phys. Rept. **388** (2003) 41

[9] M. Guidal, H. Moutarde and M. Vanderhaeghen, Rept. Prog. Phys. **76** (2013) 066202

[10] K. Kumericki, S. Liuti and H. Moutarde, Eur. Phys. J. A **52**, no.6, 157 (2016) doi:10.1140/epja/i2016-16157-3 [arXiv:1602.02763 [hep-ph]].

[11] M. Boër, M. Guidal and M. Vanderhaeghen, Eur. Phys. J. A **51** (2015) no.8, 103.

[12] E. R. Berger, M. Diehl and B. Pire, Timelike Compton scattering: exclusive photoproduction of lepton pairs, The European Physical Journal C23 (2002) 675-689

[13] O. Grocholski, H. Moutarde, B. Pire, P. Sznajder and J. Wagner, Eur. Phys. J. C **80** (2020) no.2, 171

[14] X. D. Ji, Phys. Rev. Lett. **78**, 610 (1997)

[15] O. Grocholski, H. Moutarde, B. Pire, P. Sznajder, J. Wagner, SciPost conf. proceeding, arXiv:2106.11790 (2021)

[16] P. Chatagnon *et al.* [CLAS], Phys. Rev. Lett. **127**, no.26, 262501 (2021)

[17] Z-E. Meziani, K. Hafidi, X. Qian, N. Spaveris, JLab experiment E12-12-006, Near Threshold Electroproduction of J/Ψ at 11 GeV, proposal to the PAC 39 (2012).

[18] C. Munoz Camacho, R. Paremuzyan, T. Horn, JLab experiment E12-13-010.

[19] F. Sabatié, A. Biselli, V. Burkert, L. Elouadrhiri, M. Garçon, M. Holtrop, D. Ireland, K. Joo, W. Kim, JLab experiment E12-06-119.

[20] S. Niccolai, V. Kubarovsky, S. Pisano, and D. Sokhan, JLab experiment E12-11-003.

[21] S. Niccolai et al, Deeply virtual Compton scattering on the neutron with a longitudinally polarized deuteron target, run group proposal E12-06-109A (2016).

[22] S. Chekanov *et al.* [ZEUS Collaboration], Phys. Lett. B **573** (2003) 46 [hep-ex/0305028].

[23] S. Chekanov *et al.* [ZEUS Collaboration], JHEP **0905** (2009) 108.

[24] A. Aktas *et al.* [H1 Collaboration], Eur. Phys. J. C **44** (2005) 1 [hep-ex/0505061].

[25] F. D. Aaron *et al.* [H1 Collaboration], Phys. Lett. B **659** (2008) 796

[26] F. D. Aaron *et al.* [H1 Collaboration], Phys. Lett. B **681** (2009) 391.

[27] Airapetian A *et al.* [HERMES Collaboration] 2012 *JHEP* **1207**, 032

[28] Airapetian A *et al.* [HERMES Collaboration] 2012 561 *JHEP* **1210**, 042

[29] Airapetian A *et al.* [HERMES Collaboration] 2010 *JHEP* **1006**, 019

[30] Airapetian A *et al.* [HERMES Collaboration] 2008 *JHEP* **0806**, 066

[31] Airapetian A *et al.* [HERMES Collaboration] 2011 *Phys. Lett. B* **704**, 15

[32] Airapetian A *et al.* [HERMES Collaboration] 2007 *Phys. Rev. D* **75**, 011103

[33] Airapetian A *et al.* [HERMES Collaboration] 2009

[34] Airapetian A *et al.* [HERMES Collaboration] 2010 *Phys. Rev. C* **81**, 035202

[35] Airapetian A *et al.* [HERMES Collaboration] 2001 *Phys. Rev. Lett.* **87**, 182001

[36] R. Akhunzyanov *et al.* [COMPASS], Phys. Lett. B **793** (2019), 188-194

[37] Camacho C M *et al.* [Jefferson Lab Hall A and Hall A DVCS Collaborations] 2006 *Phys. Rev. Lett.* **97**, 262002

[38] M. Mazouz *et al.* [Jefferson Lab Hall A Collaboration], Phys. Rev. Lett. **99** (2007) 242501

[39] M. Defurne *et al.* [Jefferson Lab Hall A Collaboration], Phys. Rev. C **92** (2015) no.5

[40] M. Benali, et al. Nature Phys. **16** (2020) no.2, 191-198

[41] Girod F X *et al.* [CLAS Collaboration] 2008 *Phys. Rev. Lett.* **100**, 162002

[42] Chen S *et al.* [CLAS Collaboration] 2006 *Phys. Rev. Lett.* **97**, 072002.

[43] S. Stepanyan *et al.* [CLAS Collaboration], Phys. Rev. Lett. **87** (2001) 182002.

[44] H. S. Jo, New Phys. Sae Mulli **69** (2019) no.4, 376-379 doi:10.3938/NPSM.69.376

[45] Proceedings from High Intensity Photon Sources Workshop (CUA, 2/6–2/7 2017), https://arxiv.org/pdf/1704.00816.pdf

[46] D. Day, *et al.* NIM A 957 (2020) 163429, arXiv:1912.07355v1

[47] T. Horn et. al, Neutral Particle Spectrometer Facility in Hall C, proposal to PAC 40 (2013).

[48] UVa target group web page: *http://twist.phys.virginia.edu/documents.html*.

[49] JLab target group web page: *https://poltar.jlab.org/drupal*.

[50] D. Keller et al. NIM 2020, In press.

[51] D. Crabb and D. Day, *"The Virginia/Basel/SLAC polarized target: operation and performance during experiment E143 at SLAC"*. Nucl. Inst. Meth. **A**356, 9-19 (1995).

[52] H. Zhu, *"A Measurement of the Neutron Electric Form Factor in $\vec{D}(\vec{e}, e'n)p$ Quasi-elastic Scattering at $Q^2_= 0.5\ (GeV/c)^2$"*. Ph.D. Dissertation, University of Virginia, Charlottesville (2000).

[53] Vanderhaeghen M, Guichon P A M and Guidal M 1998 *Phys. Rev. Lett.* **80** 5064

[54] M. Vanderhaeghen, P. A. M. Guichon and M. Guidal, Phys. Rev. D **60** (1999) 094017 doi:10.1103/PhysRevD.60.094017

[55] Guidal M, Polyakov M V, Radyushkin A V and Vanderhaeghen M 2005 *Phys. Rev. D* **72** 054013

[56] A. V. Radyushkin, In *Shifman, M. (ed.): At the frontier of particle physics, vol. 2* 1037-1099

[57] S. Liuti, private communication.

[58] A.V. Belitsky, D. Mueller and A. Kirchner, Nucl. Phys. B629 (2002) 323.

[59] A. V. Belitsky and A. V. Radyushkin, Phys. Rept. **418** (2005) 1

[60] A. V. Radyushkin, Phys. Rev. D **59** (1999) 014030

[61] A. V. Radyushkin, Phys. Lett. B **449** (1999) 81

[62] P. A. M. Guichon and M. Vanderhaeghen, Phys. Rev. Lett. **91** (2003) 142303

[63] E. J. Brash, A. Kozlov, S. Li and G. M. Huber, Phys. Rev. C **65** (2002) 051001

[64] M. Aghasyan *et al.* [COMPASS Collaboration], Phys. Rev. Lett. **119** (2017) no.11, 112002

[65] D. W. Sivers, Phys. Rev. D **41** (1990) 83.

[66] M. Burkardt and D. S. Hwang, Phys. Rev. D **69** (2004) 074032 doi:10.1103/PhysRevD.69.074032

[67] H. Moutarde, B. Pire, F. Sabatie, L. Szymanowski and J. Wagner, Phys. Rev. D **87** (2013) no.5, 054029

[68] Guidal M 2008 *Eur. Phys. J. A* **37**, 319 [Erratum-ibid. A **40**, 119 (2009)]

[69] M. Boër and M. Guidal, J. Phys. G **42** (2015) no.3, 034023

[70] M. Boër, JLab hall C note 999, Extraction of Compton Form Factor from spacelike and timelike Deeply Virtual Compton Scattering (2019). `https://hallcweb.jlab.org/DocDB/0009/000999/001/Note_CFFcombinedfits.pdf`

[71] B. Semp, M. Boër, Hall C public note 1146 (2021) `https://hallcweb.jlab.org/DocDB/0011/001146/001/TCS_Semp_actual_final.pdf`

[72] B. Semp, CNP research day workshop presentation (2022)

[73] B. Semp (private communication), B. Semp and M. Boër (unpublished) (2022).

[74] Polarization Observables in Wide-Angle Compton Scattering at large s, t, and u. G. D. Hamilton, D. Day, D. Keller, G. Niculescu, B. Wojtsekhowski, J. Zhang, and the Neutral Particle Spectrometer Collaboration, Jefferson Lab experiment E12-17-008.

[75] J. Pierce, J. Maxwell and C. Keith, Nucl. Instrum. Meth. A **738** (2014) 54.

[76] Federico Carminati et al., Workshop on Deep Learning for Physical Sciences (DLPS 2017), NIPS 2017, Long Beach, CA, USA. Dawit Belayneh et al., arXiv:1912.06794.

[77] The Charge Form Factor of the Neutron, JLab experiment E93-026, D. Day spokesperson.

[78] Precision Measurement of the Nucleon Spin Structure Functions in the Region of the Nucleon Resonances, JLab experiment E01-006, O. Rondon Aramayo spokesperson.

[79] Spin Asymmetries on the Nucleon Experiment:SANE, JLab experiment E07-003, S. Choi, Z.E. Meziani, O. Rondon-Aramayo spokespersons.

[80] D. Keller, "The UVa approved and proposed experiments," arXiv:1704.00816.

[81] K.Gnanvo et al., Large size GEM for Super Bigbite Spectrometer (SBS) polarimeter for Hall A 12 GeV program at JLab. NIMA 782 (2015) 77-86.

[82] M. Kubantsev et al., Performance of the Primex Electromagnetic Calorimeter, arXiv:physics/0609201, 22 Sep. 2006; A. Gasparyan, Performance of PWO crystal Detector for a High Resolution Hybrit Electromagnetic Calorimeter at Jefferson Lab., Proceed. X Int. Conf. Calorimetry in Particle Physics, Perugia, Italy, 29 March-2 April 2004, pp. 109-115.

[83] T. Horn at al., *"Scintillating crystals for the Neutral Particle Spectrometer in Hall C at JLab"*. Nucl. Inst. Meth. **A**956, (2020) 163375.

[84] Measurement of Semi-Inclusive π^0 Production as Validation of Factorization, JLab Experiment E12-13-007, R. Ent, T. Horn, H. Mkrtchyan and V. Tadevosyan spokespersons. Proposal aproved in 2015 by JLab PAC40.

[85] Polarimeter for Hall A 12 GeV program at JLab. NIMA 782 (2015) 77-86.

[86] F.Sauli, NIMA 805 (2016) 2-24.

[87] M. Boër, JLab hall C note 1000, DEEPGen: an event generator framework for polarized Deep Exclusive Electro- and Photo- production processes (2019). `https://hallcweb.jlab.org/DocDB/0010/001000/001/DEEPGenframeworkNote.pdf`

[88] M. Boër, DEEPGen Event Generator, `https://hallaweb.jlab.org/wiki/index.php/DEEPGen_event_generator`

[89] M. Boër, GlueX note 3571, *Angular correlations in deep exclusive photo-production of lepton pairs and tools for data analysis* (2018), `https://halldweb.jlab.org/doc-public/DocDB/ShowDocument?docid=3571`.

[90] Camille Zindy, presentations to NPS/CPS meetings and APS workshop, 2021.

[91] C. Zindy, thesis report (2021) (in French, not public).

[92] A. Ali *et al.* [GlueX], Phys. Rev. Lett. **123** (2019) no.7, 072001

[93] M. Boër, PhD thesis (2014)

[94] M. Boër, E. Burtin, Measurement of the cross section for exclusive photoproduction of a single photon and of a neutral pion on hydrogen target, in the context of Generalized partons distributions studies at COMPASS II, COMPASS note 201312 (2013)

[95] Mark Vanderhaeghen, studies of radiative corrections in TCS+BH

[96] L. W. MO and Y. S. TSAI Rev. Mod. Phys. 41, 205 (1969).

[97] A. Bolz *et al.* Journal of High Energy Physics 151 (2015)

[98] J. Breitweg et al. [ZEUS Collaboration], Eur. Phys. J. C 2 (1998) 247 [hep-ex/9712020].

[99] P.A. Zyla et al. (Particle Data Group), Prog. Theor. Exp. Phys. 2020, 083C01 (2020) and 2021 update.

[100] A. Asaturyan et al., *"Electromagnetic calorimeters based on scintillating lead tungstate crystals for experiments at Jefferson Lab"*. Nucl. Inst. Meth. **A1013**, (2021) 165683.

[101] https://jleic-docdb.jlab.org/DocDB/0006/000622/001/halld_test_setups.pdf